

Structured light generation by refractive-diffractive micro optical array illuminators

Présentée le 21 mai 2021

Faculté des sciences et techniques de l'ingénieur
Laboratoire de nanophotonique et métrologie
Programme doctoral en photonique

pour l'obtention du grade de Docteur ès Sciences

par

Maryam YOUSEFI

Acceptée sur proposition du jury

Prof. R. Houdré, président du jury
Dr T. Scharf, directeur de thèse
Dr M. Rossi, rapporteur
Dr M. Shnieper , rapporteur
Prof. C. Moser , rapporteur

To my parents, who are the meaning of love for me...

Acknowledgements

I would like to thank my thesis director, Dr. Toralf Scharf for supervising this thesis.

I want to thank Dr. Markus Rossi for giving me the chance to obtain industrial experience during the one and a half years of my stay at AMS AG.

I would like to specially thank Prof. Olivier Martin, the head of the NAM group for all his support and cooperation, during the last year of my Ph.D. He was always open to hearing my problems and questions to help me.

I would like also to thank Prof. Hans Peter Herzig for very fruitful discussions. I was taking every opportunity to discuss with him for a deeper understating of the scientific problems.

I would like to thank Dr. Julien Dorsaz (CMI-EPFL) for useful discussions during the fabrication process using the Nanoscribe Photonic Professional GT at the Center of Micro Nano Technology (CMi) at EPFL.

I would like to thank my friends at the NAM group for the enjoyable and memorable times we had together.

Finally, a special thank goes to my parents, sister, and brother who supported me in every step of this journey toward obtaining the Ph.D. I thank them for being the most important part of my life and for being always with me, in happiness and difficulties.

Lausanne, January 17, 2021

M. Y.

Abstract

Structured light generation having broad applications in different optical fields, is the topic of this thesis. Our structured light generation strategy is based on applying periodic microoptical elements at the refraction-diffraction limit, under a focused diverging source instead of a plane wave. The high contrast pattern in the far-field is achieved for certain distances between the source and periodic structure, where the self-imaging condition is satisfied. This phenomenon is the basis of our strategy to obtain a high-contrast far-field distribution. Throughout this thesis, we analytically, numerically, and experimentally examine the self-imaging condition for our light generators. We engineer the structured light using two main strategies; modifying the periodic microoptical element surface profile and modulate the source by applying an optical element in its near-field.

For surface profile modulation, we apply a sinusoidal phase grating instead of conventional periodic optical elements such as microlenses under a Gaussian beam illumination to increase the number of points in the far-field distribution. We study the far-field distribution for thin and thick sinusoidal phase gratings by comparing vectorial and scalar simulation tools for paraxial and non-paraxial diffraction angles. By properly choosing the sinusoidal phase grating thickness, large numbers of peaks with a high field of view and uniform distribution in the far-field can be achieved. We use the Two-photon Polymerization (2PP) as a rapid technique to fabricate the sinusoidal phase grating and compare the measurement results with simulations. This part of the thesis demonstrates that by properly defining the refractive-diffractive microoptical element surface profile, we can achieve even more points in far-field compared to other optical elements such as lens arrays.

In the next part, we engineer the structured light in the far-field by modifying the source near-field. By bringing a dielectric microstructure in the source near-field, a source with new optical characteristics is produced. For a dielectric microparticle, for example, a hot spot i.e a photonic nanojet (PNJ) is generated in the shadow side surface of the structure that can redistribute the dots in the far-field. We first numerically investigate the PNJ optical characteristics by changing the microsphere diameter for diverging and converging sources of low and high wavefront curvatures and compare with plane wave illumination. The PNJ shows completely different behaviors under converging and diverging illuminations when changing the particle size. In some cases, no hot spot is generated in the microparticle near-field. In this way, we can generate different sources from low to high numerical apertures.

For the experimental evaluation, we employ a high-resolution interference microscopy (HRIM) setup which is based on a Mach-Zehnder interferometer to record both the amplitude and

Abstract

phase. Our setup has the flexibility to work with different illumination conditions from plane wave to the Gaussian beam and also to observe both near-field and far-field distributions. We study the far-field distribution for a microlens array under a focused diverging source that is modulated by applying a microparticle in its near-field. With the microparticle in the source near-field, a PNJ is generated and for this reason, the pattern field of view in the far-field is modified. We record both the phase and amplitude in different planes and compare them with simulation results. Finally, we numerically and experimentally study engineering the distribution in the far-field under multiple coherently illuminating PNJs. Depending on the PNJs arrangement in the near-field, different arbitrary distribution of points in the far-field is achieved.

In summary, in this thesis, we studied various strategies to manipulate structured light characteristics. The main characteristics include the contrast, field of view, and points distribution uniformity. Our purpose is to generate large numbers of points and increase the field of view.

KEYWORDS: Diffraction, refraction, Gaussian beam, sinusoidal phase grating, microlens array, high-resolution interference microscopy, photonic nanojet

Zusammenfassung

Erzeugung strukturierter Lichtmuster haben breite Anwendungen in verschiedenen Bereichen der Optik und Sensorik. Unsere Strategie zur Erzeugung von strukturiertem Licht basiert auf der Anwendung periodischer mikrooptischer Elemente an der Grenze zwischen Brechung (geometrischer Optik) und Beugung (physikalischer Optik) sowie durch Benutzung einer divergierenden Quelle anstatt einer ebenen Welle. Das kontrastreiche Lichtmuster im Fernfeld wird bei bestimmten Abständen zwischen der Quelle und der periodischen Struktur erreicht, bei welcher die Bedingung der Selbstabbildung erfüllt ist. Das Phänomen der Selbstabbildung ist die Grundlage unserer Strategie zur Erzeugung spezieller, kontrastreicher Fernfeldverteilungen. In dieser Arbeit untersuchen wir analytisch, numerisch und experimentell die Selbstabbildungsbedingung für miniaturisierte Lichtgeneratoren. Wir verwenden zwei Hauptstrategien: Modifizierung des Oberflächenprofils eines periodischen mikrooptischen Elements und Modulation der Quelle durch Anwendung eines optischen Elements im Nahfeld der Quelle.

Als Beispiel für die Modulation des Oberflächenprofils verwenden wir ein sinusförmiges Phasengitter als periodischer mikrooptischer Elemente unter einer Beleuchtung mit einem Gauß'schen Strahl. Wir zeigen das damit die Anzahl der Strukturen in der Fernfeldverteilung erhöht werden kann. Wir vergleichen die Fernfeldverteilung für dünne und dicke Sinusphasengitter, indem wir vektorielle und skalare Simulationswerkzeuge für paraxiale und nicht-paraxiale Beugungswinkel einsetzen. Durch die richtige Wahl der Dicke des Sinus-Phasengitters können im Fernfeld eine große Anzahl von Intensitätsmaxima bei gleichzeitigen hohen Sichtfeld und gleichmäßiger Verteilung erreicht werden. Zur Realisierung verwenden wir die Zwei-Photonen-Polymerisation (2PP) zur Herstellung verschiedener Sinus-Phasengitters und vergleichen die Messergebnisse mit Simulationen. Dieser Teil der Arbeit zeigt, dass wir durch die richtige Definition des Oberflächenprofils des refraktiv-beugenden mikrooptischen Elements noch mehr Punkte im Fernfeld erreichen können als mit den willkürlich verwendeten optischen Elementen wie z.B. Linsenarrays.

Im nächsten Teil der Arbeit erzeugen wir das strukturierte Licht im Fernfeld durch Modifizieren des Quellen-Nahfeldes. Durch Aufbringen einer dielektrischen Mikrostruktur im Quellennahfeld wird eine Quelle mit neuen optischen Eigenschaften erzeugt. Für ein dielektrisches Mikroteilchen wird zum Beispiel ein Intensitätsbündelung (Hot Spot) durch das Prinzip des photonischer Nanojet (PNJ), auf der schattenseitigen Oberfläche der Struktur erzeugt. Dieser Effekt ändert die Lichtverteilung im Fernfeld. Wir untersuchen zunächst numerisch die optischen Eigenschaften des PNJ bei Änderung des Durchmessers einer Mikrokugel für

divergierende und konvergierende Quellen mit niedrigen und hohen Wellenfrontkrümmungen. Der photonischer Nanojet PNJ zeigt bei konvergierender und divergierender Beleuchtung durch Änderung der Partikelgröße ein völlig unterschiedliches Verhalten; in einigen Fällen wird kein Hot Spot im Mikrokugel-Nahfeld erzeugt. Auf diese Weise können wir in einer Ebene verschiedene Quellen von niedriger bis hoher numerischer Apertur erzeugen, indem wir mehrere Mikrostrukturen in das Quellen-Nahfeld bringen.

Für die experimentelle Untersuchung verwenden wir einen neu entwickelten Interferenzaufbau mit hochauflösender Mikroskopie, der auf einem Mach-Zehnder-Interferometer basiert. Damit können wir sowohl die Amplitude als auch die Phase im Nahfeld- als auch die Fernfeldverteilung erfassen. Unser Aufbau hat die Flexibilität, mit verschiedenen Beleuchtungsbedingungen von der ebenen Welle bis zum Gaußschen Strahl zu arbeiten und ein präzises Ausrichten aller Komponenten vornehmen. Wir untersuchen die Fernfeldverteilung für ein Mikrolinsenarray unter einer fokussierten, divergierenden Quelle, die durch Aufbringen eines Mikropartikels in ihrem Nahfeld moduliert wird. Mit dem Mikropartikel an der Quelle im Nahfeld wird ein photonischer Nanojet PNJ erzeugt und aus diesem Grund wird das Lichtmuster im Fernfeld ausgeweitet. Wir messen sowohl die Phase als auch die Amplitude in verschiedenen Ebenen auf und vergleichen sie mit den Simulationsergebnissen. Schließlich untersuchen wir numerisch und experimentell die exakte Verteilung der Punkte im Fernfeld wenn mehrere kohärent leuchtenden photonischer Nanojet PNJ vor der Quelle platziert werden. Abhängig von der Anordnung der photonischer Nanojet PNJs im Nahfeld wird eine unterschiedliche willkürliche Verteilung der Punkte im Fernfeld erreicht.

Zusammenfassend lässt sich sagen, dass wir in dieser Arbeit verschiedene Strategien zur Manipulation der strukturierten Lichtcharakteristika untersucht haben. Als Kriterien haben wir den Kontrast, das Sichtfeld und die Gleichmäßigkeit der Punktverteilung herangezogen. Wir haben dabei erfolgreich neue Strategien zur Erzeugung kontrastreicherer Verteilung von Punkten mit vergrößerten Sichtfeld gefunden.

Schlüsselwörter: Beugung, Brechung, Gaußscher Strahl, Sinus-Phasengitter, Mikrolinsenarray, hochauflösende Interferenzmikroskopie, photonischer Nanojet

Contents

Acknowledgements	iii
Abstract (English/Deutsch)	v
1 Introduction	1
1.1 Structured light generation strategies	2
1.1.1 Talbot effect Theory	4
1.1.2 Lau effect Theory	4
1.2 Objective and thesis outline	5
2 Simulation tools	9
2.1 Vectorial Theory	10
2.2 Scalar approaches in free-space	11
2.2.1 Angular Spectrum of Plane waves	11
2.2.2 Huygens-Fresnel principle and Rayleigh-Sommerfeld diffraction formula	14
2.2.3 Fresnel approximation	15
2.2.4 Fraunhofer approximation	16
2.2.5 High numerical aperture far-field propagator	17
2.3 Scalar methods for optical element modeling	17
2.3.1 Thin element approximation (TEA)	17
2.3.2 Fourier transform Beam propagation method (FFT-BPM)	18
2.4 Discussions around the thesis problem	20
2.4.1 Analytical evaluation	21
3 Structured pattern generation for 1D sinusoidal phase grating	25
3.1 Configuration	25
3.2 Why the sinusoidal shape?	26
3.3 Diffractive/refractive element simulations	29
3.3.1 Variable source beam waist	29
3.3.2 Variable Phase profile thickness h	33
3.3.3 Transmission versus phase grating thickness using FDTD	37
3.4 Experimental Evaluation	38
3.4.1 Sample Fabrication using two photon absorption	38
3.4.2 Comparison of simulation and experiment	41

3.5	Far-field pattern contrast evaluation versus D	43
3.6	Surface profile optimization	44
3.7	Summary	48
4	Interferometry setup	51
4.1	Interferometer setup	52
4.2	Phase-shifting interferometry technique	52
4.3	High-resolution interference microscopy	53
4.3.1	High-resolution interferometry setup under plane wave	54
4.3.2	High-resolution interferometry setup under focused beam	55
4.3.3	Setup optical components and their functionality	56
4.4	Sources of error	64
4.4.1	Phase shift error	64
4.4.2	Detector nonlinearity	65
4.4.3	Source stability	65
4.4.4	Quantization error	65
4.4.5	Vibration error	65
4.4.6	Air currents and turbulence	66
4.4.7	Coherent noises	66
5	Near-field and far-field measurement for a focused source	69
5.1	Configuration	69
5.2	Simulation of near-field distribution and far-field intensity	70
5.3	HRIM setup	72
5.4	Experimental results	73
5.5	Summary	74
6	Analysis of Photonic Nanojet (PNJ) for different illumination conditions	77
6.1	PNJ as source near-field modulator for structured light generation	78
6.2	Configuration	79
6.3	Results and discussion	80
6.3.1	Comparison of the PNJ for the sphere diameter of 3.3λ and 25λ	82
6.3.2	FWHM and effective focal length f versus the sphere diameter d for diverging beam	83
6.3.3	FWHM and effective focal length f versus the sphere diameter d for converging beam	85
6.3.4	The analogy between converging source NA and sphere refractive index n	86
6.3.5	Comparison between 2D and 3D simulations	88
6.4	Summary	90
7	Structured light engineering using a photonic nanojet	95
7.1	Introduction	95
7.2	Configuration	95

7.3	Simulations	96
7.3.1	Gaussian Beam illumination	97
7.3.2	Modulated Gaussian beam by PNJ	98
7.4	Experiments	101
7.4.1	Gaussian beam illumination	102
7.4.2	Modulated Gaussian beam by PNJ	103
7.5	Comparison between simulations and experiments	105
7.6	Summary	106
8	Structured light engineering for photonic nanojets as multi-sources	109
8.1	Introduction	109
8.2	Simulations	109
8.3	Experiments	112
8.4	Summary	112
9	Summary and outlook	115
	Curriculum Vitae	119

1 Introduction

The physical world around us is three-dimensional (3D); traditional optical sensors and cameras can only record two-dimensional (2D) images and not the depth information [1]. In recent decades, great advances have been achieved in research and industrialization of 3D surface imaging technologies because of its comprehensive application in different fields. Three dimensional surface imaging and sensing is referred to the measurement of coordinate (x, y, z) of points on the surface of an object; the surface which is normally non-planar. Structured light generation is a principle technique for 3D surface imaging. As seen in Fig. 1.1, structured light is illuminated and a 2D image is acquired from the pattern distribution in the scene by making use of a camera. By analyzing the intensity distribution in the 2D image, the dept information is extracted. The structured light 3D surface imaging is based on the field distortion of the projected pattern in the scene.

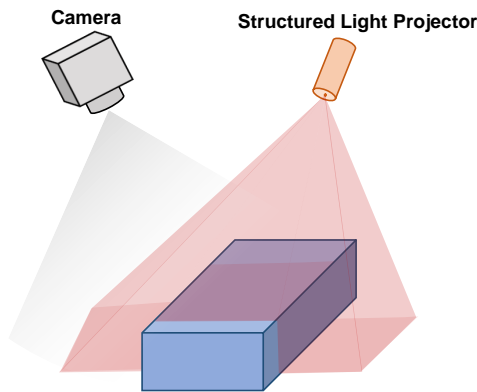


Figure 1.1: Structured light for 3D surface imaging.

This technique has various applications including imaging, microscopy, and sensing [1–3]. Figure 1.2 illustrates some practical daily life applications of structured light generation in smartphones, body position and dept recognition in Microsoft Kinect, Lidar systems, driver

monitoring, and health care such as 3D surface imaging for dental applications.

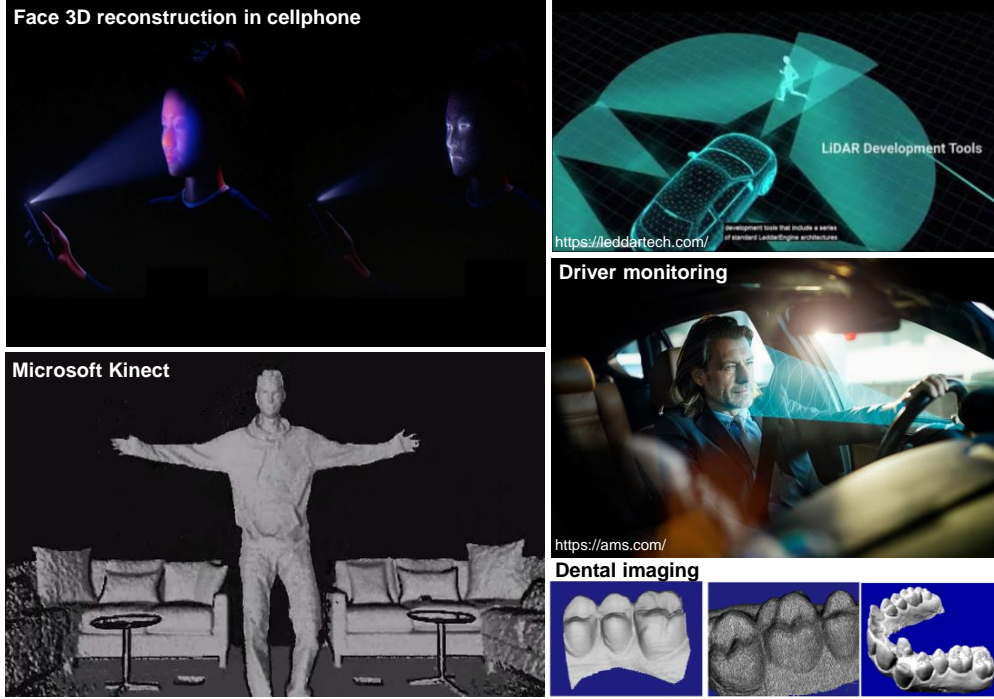


Figure 1.2: Example applications of 3D surface imaging in different fields, including smart-phones, entertainment, automotive, and health care such as dental imaging [1].

On the other hand, optics is the area of studying the electromagnetic fields and their behavior in interaction with matter. Many of the optical phenomena can be explained by classical optics [2]. In the geometrical or refractive optics, the fields are treated as a package of straight rays that refract and reflect at the interface between two mediums. Physical optics is a more comprehensive study in which the electromagnetic fields are considered as waves, showing diffraction, and interference effect. In this thesis, we will focus on structured light generation based on physical optics. Here we first review two main categories of structured light generation strategies and then we will introduce our approach by giving an introduction to its basic theory.

1.1 Structured light generation strategies

For some sensing applications such as face and body 3D reconstruction, generating large numbers of dots with a wide field of view and equal intensity peaks in the far-field is essential and also challenging to do. For this purpose, using micro-optical and diffractive optical elements with different aspect ratios from low to high is a practical method especially in terms of pattern field of view [4–7]. Figure 1.3 demonstrates the two concepts. Using binary

diffractive optical elements which are designed using optimization techniques produce a defined functionality for structured pattern generation [8–10]. Using binary diffractive optical elements, a uniform distribution of spots is designed in the far-field, as seen in Fig. 1.3(a). However, using this method is limited by some effects: First, the design is monochromatic. Second, there can be unwanted intensity in zero-order and outside the field of view due to fabrication errors [11]. Not all diffraction orders are addressed and it is quite challenging to design very high angle pattern distributions using this technique due to the very small feature size [12].

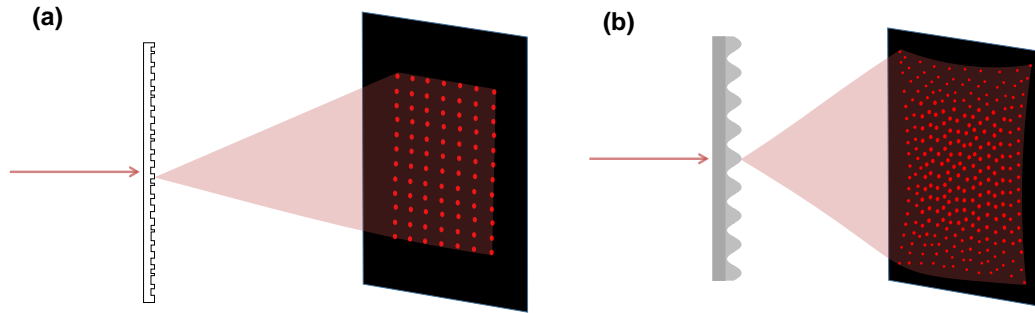


Figure 1.3: (a) Dot pattern generation for a binary diffractive optical element. A series of well-defined dot positions are designed and dots are optimized for intensity. (b) Dot pattern generation for a periodic refractive-diffractive optical element. Dots appear by diffraction and the intensity distribution is designed by the surface profile of the micro-optical components.

Using small period refractive optical elements that combine refraction and diffraction is another method for spot array generation in which the pattern distribution very much depends on the surface profile of the optical element [8, 13–15]. In this case, as sketched in Fig. 1.3(b), all diffraction orders can be used and the intensity distribution is managed by the form of the structure. There is no very small feature but the precision of the surface profile needs to be high. In this thesis, we will employ this strategy that is based on designing refractive-diffractive optical elements such as microlenses and phase gratings. We investigate micro-optical elements with a period of 50λ to 75λ which allows us to control both diffractive and refractive effects [8]. As we explained, physical optics is a more precise investigation than refractive optics in the refractive-diffractive regime. Many approximations still can be made in physical optics, the waves can be treated as scalar electric fields for instance. Fourier optics is a scalar approach in which the wavefronts are considered to be the superposition of plane waves and the field distribution can be expressed by a Fourier transform. To further introduce the topic, here we review two concepts based on the Fourier optics analysis.

1.1.1 Talbot effect Theory

The Talbot effect as a self-imaging concept was first observed by Henry Fox Talbot in 1835 [16]. For a diffraction grating under plane wave illumination, the image of the grating is repeated at regular distances from the grating plane which is a multiple of so-called Talbot distance, as seen in Fig. 1.4. Lord Rayleigh demonstrated that the Talbot distance is calculated by the following formula [17]:

$$z_T = \frac{2P^2}{\lambda} \quad (1.1)$$

Where P is the period of diffraction grating and λ is the source wavelength. Talbot carpet is observable in the grating near-field. Near-field here is referred to Fresnel region in the Fourier optics.

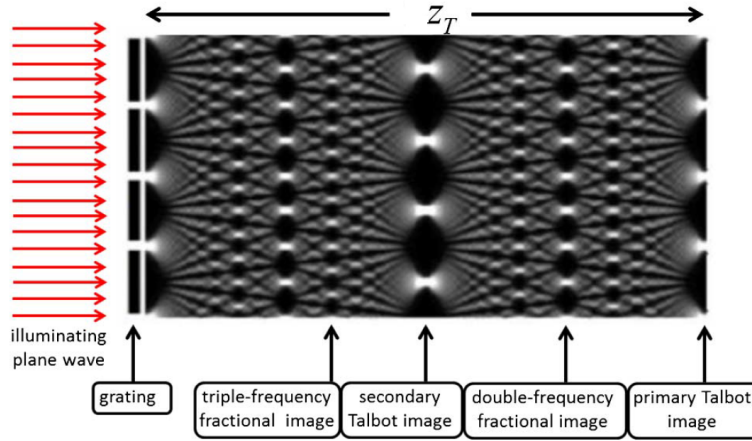


Figure 1.4: The optical Talbot effect for monochromatic light, shown as a Talbot carpet. The plane wave is illuminated from the left side on a grating, and the pattern is reproduced at certain distances from the grating [18].

1.1.2 Lau effect Theory

Considering the so-called Lau effect for a periodic grating under a point source illumination, the intensity distribution in the far-field varies according to the distance between the source and the grating. As seen in the configuration in Fig. 1.5, a point source illuminates a lens array at a certain distance. The image of the periodic structure is reproduced in the far-field at specific distances of z_T that is expressed by,

$$z_T = M \times \frac{P^2}{2\lambda} \times \frac{1}{N} \quad (1.2)$$

Where P is the optical element period, λ is the source wavelength, M and N are integer values.

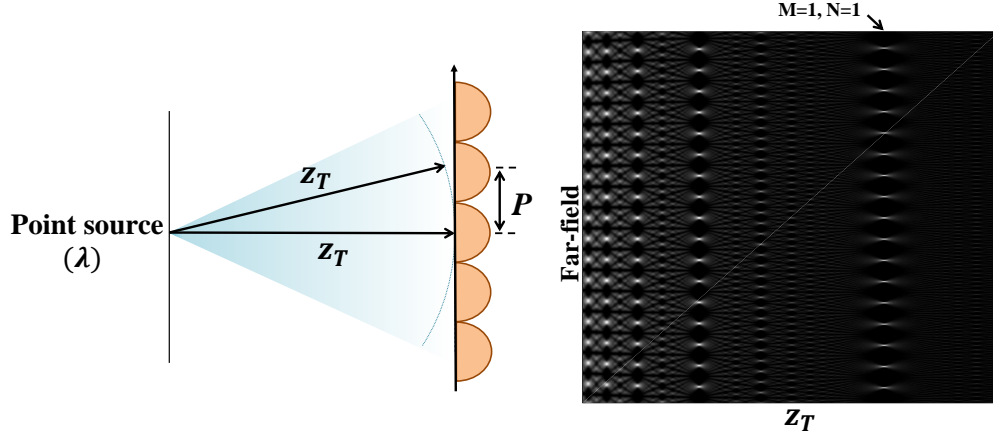


Figure 1.5: The optical Lau effect for a point source monochromatic light. The point source illuminates the periodic optical element at the certain distances of z_T from MLA and the pattern is reproduced in the far-field.

1.2 Objective and thesis outline

Light pattern generation is a practical strategy in different industrial fields. In this thesis, our focus is on pattern generation for sensing and imaging system in smartphones. The state of art 3D light projectors for mobile application has greatly advanced in recent years. A highly compact point generator ($3.5mm \times 3.5mm \times 3.5mm$) with a large field of view of $71^\circ \times 51^\circ$ (considering the Full width at half maximum definition) and $6k$ number of points have been introduced as standard in the industry [19]. The number of points can even be further increased up to $10k$. In another well-known point generator technology which is already been used in iPhone, the number of points can reach $30k$ [20]. Considering the great advances in the design of light generators, our purpose is to introduce strategies to obtain a high FOV and increase the number of points in the pattern. On the other side, the module should be kept very compact and slim; a criterion that is important in industrial applications. For a better understanding, we separately study the FOV and number of points as the figure of merit. Initially, we investigate strategies to increase the number of points. Then, we will draw our attention to enlarging the FOV. Finally, we introduce a scenario in which we can increase both the number of points and FOV, simultaneously. Overall, we are mostly focused on increasing the number of points in the pattern as it is a more difficult task to perform.

As we introduced our strategy, we apply a refractive-diffractive optical element for structured light generation. More specifically, as it is seen in Fig. 1.6, the configuration which will be studied in this thesis is a periodic microoptical element under a point source illumination; the pattern distribution will be recorded in the far-field. As we explained earlier, the period of the structure is between 50λ to 75λ . The periodic optical element can be a phase grating (here, we investigate a sinusoidal phase grating) or a microlens array with a square or hexagonal lattice. The distance between the point source and the optical element is required to be the

Lau distance z_T to observe a high contrast image in the far-field.

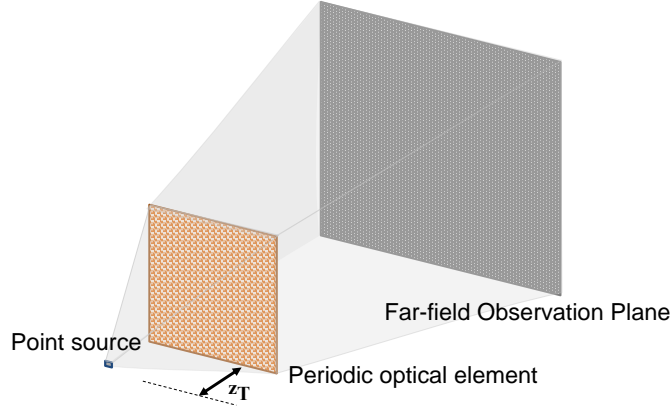


Figure 1.6: Our structured light generation strategy.

The pattern distribution in the far-field is engineered by many parameters including the source optical characteristics, periodic optical element geometry, the distance between the source and optical element, etc. Our figure of merit is the pattern field of view (FOV) and the pattern uniformity distribution. We aim to generate a high contrast pattern with a high FOV and uniform distribution.

In chapter 2, we will review the scalar and vectorial tools for simulating our problem. Then, we will analytically study the interdependence of parameters and introduce our strategies for improving the figure of merit.

In chapter 3, we will demonstrate a 1D dot pattern generator for a sinusoidal phase grating and compare different simulation tools for low and high structures. We will then compare the simulations with experiments.

In chapter 4, a high-resolution optical microscopy system is presented and designed for recording the phase and intensity in different planes.

In chapter 5, we numerically and experimentally record the near-field and far-field for a micro-lens array under the green Gaussian beam illumination.

In chapter 6, the photonic nanojet (PNJ) phenomenon is introduced and theoretically investigated under different sources from low to high diverging and converging curvatures. This chapter is a theoretical introduction to applying the PNJ as a tool for the source near-field modulation.

In chapter 7, a pattern generator for a micro-lens array under the Gaussian beam which is modified using the photonic nanojet (PNJ) phenomenon, is studied theoretically, and experimentally by making use of the high-resolution microscopy setup.

In chapter 8, a pattern generator for a micro-lens array by applying a coherent array of sources instead of one single source will be realized, theoretically, and experimentally.

References

- [1] J. Geng. “Structured-light 3d surface imaging: a tutorial”. *Advances in Optics and Photonics*, 3(2):128–160, 2011.
- [2] S. Zhang. “High-speed 3d shape measurement with structured light methods: a review”. *Optics and Lasers in Engineering*, 106:119–131, 2018.
- [3] “Optics”. en, Sept. 2020. URL: <https://en.wikipedia.org/w/index.php?title=Optics&oldid=976430149> (visited on 09/22/2020). Page Version ID: 976430149.
- [4] N. I. Petrov and G. N. Petrova. “Diffraction of partially-coherent light beams by microlens arrays”. *Optics express*, 25(19):22545–22564, 2017.
- [5] W. Eckstein, E.-B. Kley, and A. Tünnermann. “Comparison of different simulation methods for effective medium computer generated holograms”. *Optics express*, 21(10):12424–12433, 2013.
- [6] U. Levy, C.-H. Tsai, H.-C. Kim, and Y. Fainman. “Design, fabrication and characterization of subwavelength computer-generated holograms for spot array generation”. *Optics express*, 12(22):5345–5355, 2004.
- [7] R. Vanderhouten, A. Hermerschmidt, and R. Fiebelkorn. “Design and quality metrics of point patterns for coded structured light illuminations with diffractive optical elements in optical 3d sensors”. In *Proc. SPIE*, volume 10335, 2017.
- [8] B. C. Kress. “Field guide to digital micro-optics”. In SPIE, 2014.
- [9] V. Arrizón, M. Testorf, S. Sinzinger, and J. Jahns. “Iterative optimization of phase-only diffractive optical elements based on a lenslet array”. *JOSA A*, 17(12):2157–2164, 2000.
- [10] J.-N. Gillet and Y. Sheng. “Iterative simulated quenching for designing irregular-spot-array generators”. *Applied optics*, 39(20):3456–3465, 2000.
- [11] V. Kettunen, K. Jefimovs, J. Simonen, O. Ripoll, M. Kuittinen, and H. P. Herzig. “Diffractive elements designed to suppress unwanted zeroth order due to surface depth error”. *Journal of Modern Optics*, 51(14):2111–2123, 2004.
- [12] B. C. Kress and P. Meyrueis. *Applied Digital Optics: from micro-optics to nanophotonics*. John Wiley & Sons, 2009.
- [13] A. Büttner and U. D. Zeitner. “Calculation of the average lenslet shape and aberrations of microlens arrays from their far-field intensity distribution”. *Applied optics*, 41(32):6841–6848, 2002.
- [14] Z.-N. Tian, W.-G. Yao, J.-J. Xu, Y.-H. Yu, Q.-D. Chen, and H.-B. Sun. “Focal varying microlens array”. *Optics letters*, 40(18):4222–4225, 2015.
- [15] A. Naqavi, H. P. Herzig, and M. Rossi. “High-contrast self-imaging with ordered optical elements”. *JOSA B*, 33(11):2374–2382, 2016.
- [16] “Talbot effect”. en, Sept. 2020. URL: https://en.wikipedia.org/w/index.php?title=Talbot_effect&oldid=977078514 (visited on 09/25/2020). Page Version ID: 977078514.

- [17] L. Rayleigh. “Xxv. on copying diffraction-gratings, and on some phenomena connected therewith”. *The London, Edinburgh, and Dublin Philosophical Magazine and Journal of Science*, 11(67):196–205, 1881.
- [18] J. Wen, Y. Zhang, and M. Xiao. “The talbot effect: recent advances in classical optics, nonlinear optics, and quantum optics”. *Advances in optics and photonics*, 5(1):83–130, 2013.
- [19] “Sensor Solutions | ams”. URL: <https://ams.com/ams-start> (visited on 01/10/2021).
- [20] “How to "see" the crazy dot map the iPhone X uses to scan your face”, Nov. 2017. URL: <https://www.imore.com/how-see-iphone-xs-dot-map> (visited on 01/10/2021). Section: article.

2 Simulation tools

In this chapter, we discuss different field propagators and diffraction models for simulating our configuration. Also, the validity and computational constraints of vectorial and scalar propagators will be investigated. According to classical optics, electromagnetic waves are presented by Maxwell's equations. The homogeneous Maxwell equation (Without charge and current source, in isotropic non-dispersive medium) is described by:

$$\vec{\nabla} \times \vec{E} = -\mu \frac{\partial \vec{H}}{\partial t} \quad (2.1)$$

$$\vec{\nabla} \times \vec{H} = \epsilon \frac{\partial \vec{E}}{\partial t} \quad (2.2)$$

$$\vec{\nabla} \cdot (\epsilon \vec{E}) = 0, \quad D = \epsilon E \quad (2.3)$$

$$\vec{\nabla} \cdot (\mu \vec{H}) = 0, \quad B = \mu H \quad (2.4)$$

Where, E and H are electric and magnetic field vectors, respectively as a function of position and time. The \times and \cdot are the vectorial cross-product and vectorial dot product, respectively. Also, $\vec{\nabla} = \frac{\partial}{\partial x} \vec{x} + \frac{\partial}{\partial y} \vec{y} + \frac{\partial}{\partial z} \vec{z}$, where \vec{x} , \vec{y} and \vec{z} are unit vectors along x , y , and z , respectively. Also, μ and ϵ are the permeability and permittivity of the medium in which the field is propagated. Solving Maxwell's equations often needs numerical effort and different numerical approaches such as finite difference time domain (FDTD), Rigorous Coupled Wave Analysis (RCWA), finite element approach (FEM), etc. have been realized to calculate the electromagnetic fields. Since we implement the FDTD technique for the rigorous simulation part, here we briefly introduce the numerical procedure for calculating the electromagnetic fields. More details of FDTD and RCWA can be found in [1, 2]. In the rigorous simulation part, we use the Lumerical FDTD [3] and the VirtualLab fusion RCWA [4] packages. The RCWA has been used for comparison with

FDTD, although we present the final simulation results using the FDTD in the thesis content.

2.1 Vectorial Theory

The FDTD technique was first proposed by Kane S. Yee in 1966 [5]. In this method, the curl operators in time-varying Maxwell's Eq.2.1 and Eq.2.2, are rewritten as the following partial derivatives:

$$-\frac{\partial B_x}{\partial t} = \frac{\partial E_z}{\partial y} - \frac{\partial E_y}{\partial z}, \quad \frac{\partial D_x}{\partial t} = \frac{\partial H_z}{\partial y} - \frac{\partial H_y}{\partial z} \quad (2.5)$$

$$-\frac{\partial B_y}{\partial t} = \frac{\partial E_x}{\partial z} - \frac{\partial E_z}{\partial x}, \quad \frac{\partial D_y}{\partial t} = \frac{\partial H_x}{\partial z} - \frac{\partial H_z}{\partial x} \quad (2.6)$$

$$\frac{\partial B_z}{\partial t} = \frac{\partial E_y}{\partial x} - \frac{\partial E_x}{\partial y}, \quad \frac{\partial D_z}{\partial t} = \frac{\partial H_y}{\partial x} - \frac{\partial H_x}{\partial y} \quad (2.7)$$

Then, the equations are solved by applying the central difference approximation to the partial derivatives. Using this approximation, both the temporal and spatial derivatives of arbitrary function f (represents electric or magnetic field) are defined by

$$\frac{\partial f(r)}{\partial r} \Big|_{r=r_0} \approx \frac{f(r_0 + \Delta r) - f(r_0 - \Delta r)}{2\Delta r} \quad (2.8)$$

where Δr is the symbol of temporal or spatial sampling. Solving Maxwell's equations by applying the FDTD method is summarized as follows: The electric field vectors are calculated in a volume in an instant in time. Then, all the magnetic field components are obtained in the same volume but in the next instant of time. The procedure is repeated until a desired steady-state electromagnetic field is realized. The smaller the spatial sampling step, the higher the accuracy. However, for computational stability, the spatial step of Δx , Δy , and Δz and temporal step of Δt are required to fulfill the following unequal:

$$\sqrt{\Delta x^2 + \Delta y^2 + \Delta z^2} > c \cdot \Delta t \quad (2.9)$$

Where c is the speed of light in the medium. This stability unequal demonstrates that the temporal step should be smaller than the time needed for the electromagnetic beam to propagate to the neighboring spatial position.

To implement the FDTD method, we first introduce a computational domain, the physical volume in which the simulation will be performed. According to our desired configuration, an appropriate boundary condition is implemented along the x , y , and z axis. As an example, the perfectly matched layer (PML) is an absorbing boundary condition, assuming the fields to

propagate in space without any reflection from the boundaries. In our work, we consider PML boundary conditions for calculating the diffraction or scattering from dielectric geometries. As we discussed, RCWA is another vectorial method for calculating electromagnetic fields although this technique is only suitable for infinitely periodic structures. By implementing the FDTD, we can simulate various configurations from periodic to non-periodic structures and also different source configurations for example the focused Gaussian beam instead of plane wave illumination. Employing a rigorous vectorial approach gives the highest accurate simulation results although still needs a lot of computational effort and in some cases, it is impossible to numerically calculate the fields. Instead, we introduce scalar propagators that are less computationally extensive and can be implemented in the optical element region as well as for the field propagation in air, depending on our configuration.

2.2 Scalar approaches in free-space

Considering the vector identity $\text{curl of } \nabla \times (\nabla \times E) = \nabla(\nabla \cdot E) - \nabla^2 E$ and applying the $\nabla \times$ operator to Eq. 2.1, the Maxwell's equations are simplified to the following wave equation[6]:

$$\nabla^2 u - \frac{n^2}{c_0^2} \frac{\partial^2 u}{\partial t^2} = 0, \quad (2.10)$$

Where n is the refractive index of the medium in which the fields are propagated and c_0 is the speed of light in air. Considering a monochromatic electromagnetic beam, all the electric and magnetic fields oscillate with the same frequency of ν and corresponding angular frequency of $\omega = 2\pi\nu$. In such a situation, the scalar field u can be represented by:

$$u = \text{Re}\{U \cdot \exp(j\omega t)\} \quad (2.11)$$

Where U is the complex scalar electric or magnetic field. Substituting the scalar field u in the wave Eq. 2.10, we obtain the following time-independent scalar so-called Helmholtz equation

$$\nabla^2 U + k^2 U = 0, \quad k = nk_0 = \omega \sqrt{\epsilon \mu} \quad (2.12)$$

Where k is the wavenumber and $\lambda = c_0/n\nu$. The Helmholtz equation is the basis of many scalar propagators in free space. Here, we introduce several useful scalar propagators that can be applied for the propagation of the field in free space.

2.2.1 Angular Spectrum of Plane waves

As seen in Fig. 2.1, consider a complex field across the $z = 0$ plane, that is represented by $U(x_1, y_1, 0)$. Our purpose is to calculate the complex field $U(x_2, y_2, z)$ across the second plane that is parallel with the first plane. Considering the angular spectrum of plane waves (ASP) method, the electric field in the $z = 0$ plane is decomposed into a spectrum of plane waves, propagating in different directions away from that plane. The angular spectrum of fields in

the observation plane can be represented by a Fourier transform,

$$A\left(\frac{\alpha}{\lambda}, \frac{\beta}{\lambda}; z\right) = \iint_{-\infty}^{+\infty} U(x_2, y_2, z) \exp\left[-j2\pi\left(\frac{\alpha}{\lambda}x + \frac{\beta}{\lambda}y\right)\right] dx dy \quad (2.13)$$

Taking an inverse Fourier transform of $A\left(\frac{\alpha}{\lambda}, \frac{\beta}{\lambda}; z\right)$, the field distribution $U(x_2, y_2, z)$ is obtained as follows

$$U(x_2, y_2, z) = \iint_{-\infty}^{+\infty} A\left(\frac{\alpha}{\lambda}, \frac{\beta}{\lambda}; z\right) \exp\left[j2\pi\left(\frac{\alpha}{\lambda}x + \frac{\beta}{\lambda}y\right)\right] d\alpha/\lambda d\beta/\lambda \quad (2.14)$$

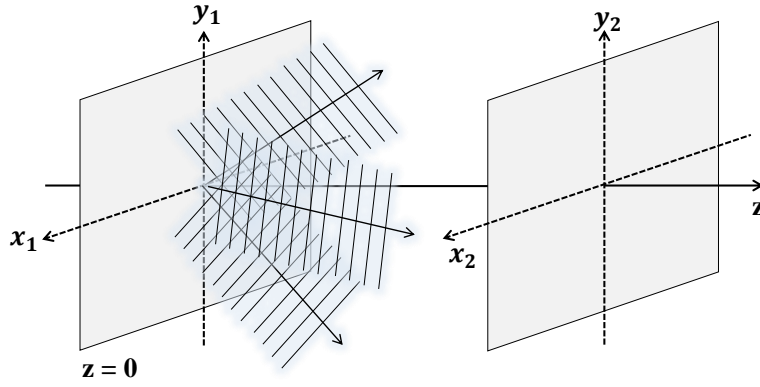


Figure 2.1: The angular spectrum of plane waves (ASP) method. The fields in the plane of $z = 0$ are decomposed into plane waves, and propagated to the observation plane.

On the other side, the complex field U satisfies the Helmholtz equation,

$$\nabla^2 U + k^2 U = 0, \quad (2.15)$$

By substituting Eq. 2.14 in Helmholtz formula, and solving a second-order differential equation, the following elementary solution is realized,

$$A\left(\frac{\alpha}{\lambda}, \frac{\beta}{\lambda}; z\right) = A\left(\frac{\alpha}{\lambda}, \frac{\beta}{\lambda}; 0\right) \exp\left[j\frac{2\pi}{\lambda} z \sqrt{1 - \alpha^2 - \beta^2}\right] \quad (2.16)$$

Where $A\left(\frac{\alpha}{\lambda}, \frac{\beta}{\lambda}; 0\right)$ is the Fourier transform of the complex field in the source plane. In the other words, $A\left(\frac{\alpha}{\lambda}, \frac{\beta}{\lambda}; 0\right)$ demonstrates the field in the source plane as the spectrum of plane waves propagating in different directions. The exponential term in Eq. 2.16 is interpreted as the phase delay that each of the plane waves encompasses by traveling between the source and the observation plane, by considering the following criterion for α and β

$$\alpha^2 + \beta^2 < 1 \quad (2.17)$$

It means that the square root in Eq. 2.16 is required to be real, resulting in an exponential term

that expresses a traveling plane wave. However, if (α, β) satisfy

$$\alpha^2 + \beta^2 > 1 \quad (2.18)$$

The square root in the exponential term is imaginary; meaning that for such a pair of (α, β) , the beams are evanescent and are rapidly attenuated. Finally, the fields in the observation plane are written as

$$U(x_2, y_2, z) = \iint_{-\infty}^{+\infty} A\left(\frac{\alpha}{\lambda}, \frac{\beta}{\lambda}; 0\right) \exp\left[j\frac{2\pi}{\lambda}z\sqrt{1-\alpha^2-\beta^2} \times \text{circ}(\sqrt{\alpha^2+\beta^2})\right] \exp\left[j2\pi\left(\frac{\alpha}{\lambda}x + \frac{\beta}{\lambda}y\right)\right] d\alpha/\lambda d\beta/\lambda \quad (2.19)$$

This equation can be simplified to the following inverse Fourier transform that will be employed in simulations,

$$U(x_2, y_2, z) = IFT\left\{A(f_x, f_y; 0) \exp\left[j\frac{2\pi}{\lambda}z\sqrt{1-\alpha^2-\beta^2} \times \text{circ}(\lambda\sqrt{f_x^2+f_y^2})\right]\right\} \quad (2.20)$$

Where $f_x = \alpha/\lambda$ and $f_y = \beta/\lambda$. The *circ* function is embedded in the equation to skip the evanescent beams that satisfy $\alpha^2 + \beta^2 > 1$. Therefore, the evanescent beams do not contribute to the resulting field in the observation plane. Using this simulation tool, the sampling distance in the source plane and the observation plane is the same, applying constraints to the applicability of this propagator. The phase term in the equation also imposes additional constraints to be properly sampled in simulations. This condition for a 1D function is as follows,

$$\Delta f \left| \frac{\partial \phi_H}{\partial f} \right|_{max} \leq \pi \quad \text{for} \quad \phi_H = 2\pi z \sqrt{\frac{1}{\lambda^2} - f^2} \quad (2.21)$$

Where Δf is the sampling distance in the observation plane. $\frac{\partial \phi_H}{\partial f}$ has a positive gradient, meaning that $\left| \frac{\partial \phi_H}{\partial f} \right|_{max}$ is realized for $f = f_{max}$ and $f_{max} = \frac{1}{2\Delta x}$ in which Δx is the sampling distance in the source plane. Replacing f_{max} in Eq. 2.21, results in the following constraint for N number of sampled points,

$$z < N\Delta x^2 \sqrt{\frac{1}{\lambda^2} - \frac{1}{4\Delta x^2}} \quad \text{for} \quad \Delta x \geq \lambda/2 \quad (2.22)$$

It implies that this propagator is only valid for short distances of z . In our problem of interest, if we consider for example for a wavelength of $\lambda = 600nm$ and the sampling parameters of $\Delta x = 1\mu m$ and $N = 1000$, in the source plane; the ASP is valid for $z < 1.6mm$. For this reason, we will only apply ASP for the field propagation between the diverging source and the optical element plane in which the distance z is in the range of 2 to 3 mm , in our problems. Also, as it is seen from the $\Delta x \geq \lambda/2$ constraint, this propagator cannot be applied to diffractive optical elements with very small features sizes of less than $\lambda/2$ in the source plane. The feature size in

the source plane in our problems is larger than $\lambda/2$ and for this reason, ASP is suited for field propagation from source to the optical element plane.

2.2.2 Huygens-Fresnel principle and Rayleigh-Sommerfeld diffraction formula

Here, we first briefly introduce the Rayleigh-Sommerfeld formula which is the basis of many scalar propagators. According to the Huygens-Fresnel principle, the field in the observation plane can be expressed as a superposition of spherical diverging beams that originate from secondary point sources in the source plane, as it is observed in Fig. 2.2. In this way, the complex field in the observation plane can be mathematically expressed by the following Rayleigh-Sommerfeld equation [7]

$$U(x_2, y_2; z) = \frac{1}{j\lambda} \iint_{-\infty}^{+\infty} U(x_1, y_1; 0) \frac{\exp(jkr)}{r^2} \cos\theta \, dx_1 \, dy_1 \quad (2.23)$$

Where θ is the angle between the normal vector \vec{n} and the vector r pointing from P_1 to P_2 . Also, r can be explicitly given by the following formula,

$$r = \sqrt{z^2 + (x_2 - x_1)^2 + (y_2 - y_1)^2} \quad (2.24)$$

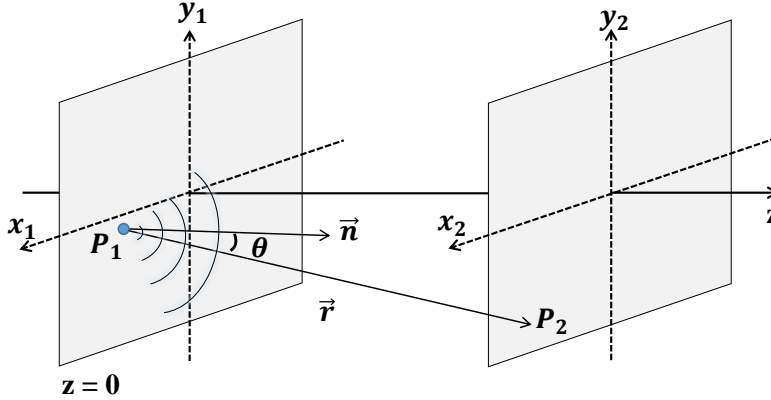


Figure 2.2: Huygens-Fresnel principle. The field in the source plane is considered to be the superposition of secondary point sources that propagate to the observation plane.

To this point, two approximations are considered in the Rayleigh-Sommerfeld Eq. 2.23; first, it is based on the scalar theory, and second the distance is much larger than the wavelength ($r \gg \lambda$). As it will be explained in the following sections, assuming more approximations, one obtains even more simplified propagators than the Rayleigh-Sommerfeld equation.

2.2.3 Fresnel approximation

To simplify the Huygens-Fresnel Eq. 2.23, we introduce an approximation to r which is the distance between P_1 and P_2 . Assuming the paraxial approximation, the diffraction angle is small, resulting in $\theta \approx \sin \theta$ and $\cos \theta \approx 1$. By applying the binomial expansion to the square root formula in Eq. 2.24 and considering only the first two terms in the expansion (because of the paraxial approximation), r can be given by

$$r \approx z \left[1 + \frac{1}{2} \left(\frac{x_2 - x_1}{z} \right)^2 + \frac{1}{2} \left(\frac{y_2 - y_1}{z} \right)^2 \right] \quad (2.25)$$

As seen in Rayleigh-Sommerfeld Eq. 2.23, r appears in the denominator as well as in the exponential term. We apply the $r \approx z$ in the denominator as the resulting error for this approximation is negligible. For the exponential term, the binomial expansion in Eq. 2.25 is applied, as more accuracy is required in the phase term. Considering these approximations, the complex field in Eq. 2.23 is simplified to

$$U(x_2, y_2; z) = \frac{e^{jkz}}{j\lambda z} \iint_{-\infty}^{+\infty} U(x_1, y_1; 0) e^{j\frac{k}{2z}[(x_2 - x_1)^2 + (y_2 - y_1)^2]} dx_1 dy_1 \quad (2.26)$$

The Fresnel equation can also be represented by the following Fourier transform,

$$U(x_2, y_2; z) = \frac{e^{jkz}}{j\lambda z} e^{j\frac{k}{2z}(x_2^2 + y_2^2)} FT\{U(x_1, y_1; 0) e^{j\frac{k}{2z}(x_1^2 + y_1^2)}\} \quad (2.27)$$

Eq. 2.26 can be expressed in two following forms; the formulas that we will apply in our simulations,

$$U(x_2, y_2; z) = IFT\{FT[U(x_1, y_1; 0)] \cdot H(f_x, f_y)\} \quad \text{where} \quad H(f_x, f_y) = e^{jkz} e^{-j\pi\lambda z(f_x^2 + f_y^2)} \quad (2.28)$$

Or

$$U(x_2, y_2; z) = IFT\{FT[U(x_1, y_1; 0)] \cdot FT[h(x_1, y_1)]\} \quad \text{where} \quad h(x_1, y_1) = \frac{e^{jkz}}{j\lambda z} e^{+j\frac{k}{2z}(x_1^2 + y_1^2)} \quad (2.29)$$

The spatial frequencies in the observation plane are $f_x = \frac{x_2}{\lambda z}$ and $f_y = \frac{y_2}{\lambda z}$. Supposing N to be the number of points in the source plane with a sampling distance of Δx , Δx_2 in the observation plane is obtained to be $\frac{\lambda z}{N\Delta x}$. On the other side, the exponential terms in Eq. 2.28 and Eq. 2.29 impose additional constraints in the sampling interval and z distance validity range. If we apply Eq. 2.28 in simulations, the following condition should be satisfied for a 1D phase function,

$$\Delta f \left| \frac{\partial \phi_H}{\partial f} \right|_{max} \leq \pi \quad \text{for} \quad \phi_H = \pi \lambda z f^2 \quad (2.30)$$

$\frac{\partial \phi_H}{\partial f}$ has a positive gradient; resulting in $\left| \frac{\partial \phi_H}{\partial f} \right|_{max} = \frac{\pi \lambda z}{\Delta x}$ and the validity region for z is obtained to be $z \leq \frac{N \Delta x^2}{\lambda}$. On the other side, if we employ the Eq. 2.29 in simulations, the following criterion is required be considered for sampling (assuming a 1D phase function),

$$\Delta x \left| \frac{\partial \phi_h}{\partial x} \right|_{max} \leq \pi \quad \text{for} \quad \phi_h = \frac{k}{2z} x^2 \quad (2.31)$$

$\frac{\partial \phi_h}{\partial x}$ has a positive gradient. As a result, the $\left| \frac{\partial \phi_h}{\partial x} \right|_{max}$ is obtained to be $\frac{k}{2} \frac{N \Delta x}{z}$. In such a condition, the validity region for z is calculated to be $z \geq \frac{N \Delta x^2}{\lambda}$. We observe that Eqs. 2.28 and 2.29 demonstrate opposite validity conditions. Although, applying both equations is valid in the so-called critical sampling condition in which

$$z = \frac{N \Delta x^2}{\lambda} \quad (2.32)$$

More details and simulated examples are presented in Ref. [8] that compares the sampling criterion by applying Eqs. 2.28 and 2.29.

2.2.4 Fraunhofer approximation

For the long propagation distance of z , the Fresnel approximation can be further simplified. Assuming $z \rightarrow \infty$, the complex field in the observation plane in Eq. 2.27 is found by

$$U(x_2, y_2; z) = \frac{e^{jkz}}{j\lambda z} e^{j\frac{k}{2z}(x_2^2 + y_2^2)} FT\{U(x_1, y_1; 0)\} \quad (2.33)$$

Which is the Fourier transform of the complex field in the source plane. This simplified diffraction model is called the Fraunhofer approximation and it is known as the field calculator for the far-field observation plane. The spatial frequencies in the observation plane are $f_x = \frac{x_2}{\lambda z}$ and $f_y = \frac{y_2}{\lambda z}$; the same as Fresnel approximation. It means that the spatial mapping between the source and the observation plane is the same as the Fresnel approximation. The following condition is assumed to drop the exponential term in the Fourier transform formula in Eq. 2.27,

$$\frac{k}{2z}(x_1^2 + y_1^2) \ll 1 \quad (2.34)$$

However, instead, we can apply a less strict condition which is known as antenna designer's formula[8]; if D is the source aperture diameter, the Fraunhofer approximation is valid for

$$z > \frac{2D^2}{\lambda} \quad (2.35)$$

In our problem, we apply the Fraunhofer approximation to calculate the far-field, by taking the Fourier transform of near-field directly after the optical element. Assuming D to be 1 mm and $\lambda = 600 \text{ nm}$, the validity range is $z > 3 \text{ m}$ for a Plane wave illumination. However, the

Fraunhofer approximation validity region is extended to smaller distances of z for a Gaussian beam illumination [8]. In our configuration, the source is a Gaussian beam instead of a Plane wave and for this reason, the far-field approximation is valid for a z distance of less than 3 m . On other hand, the Fraunhofer propagator is a proper choice to obtain the low diffraction angle far-field patterns in which the paraxial approximation is valid. Otherwise, for high diffraction angle far-field patterns, the high numerical aperture far-field propagator is applied as it is explained below.

2.2.5 High numerical aperture far-field propagator

For the high diverging light pattern generation in the far-field, the paraxial approximation is not valid in the observation plane and a fast and more accurate method is required. To obtain the far-field for a high diverging beam, we use the high NA propagator as proposed by Engelberg [8]. It is defined by the following formula assuming that the paraxial approximation is lifted in the observation plane.

$$U(x_2, y_2; z) = z \frac{e^{jkR_2}}{j\lambda R_2^2} FT\{U(x_1, y_1; 0)\} \quad (2.36)$$

with $f_x = \frac{x_2}{\lambda R_2}$ and $f_y = \frac{y_2}{\lambda R_2}$ for $R_2 = \sqrt{z^2 + x_2^2 + y_2^2}$. Applying the high NA method, the coordinate mapping between the source plane and the observation plane is not linear anymore. This is the major difference in comparison with the Fresnel and Fraunhofer approximation for which the mapping between the source plane and the observation plane is linear. It means that a uniform grid of points in the source plane is mapped to a non-uniform grid of points in the observation plane. Also, the electric field is proportional to z/R_2^2 which may significantly change the pattern envelope in comparison to the Fraunhofer propagator if the paraxial approximation is not valid in the observation plane x_2 . The x_2 and y_2 in the observation plane, can be rewritten as a function of spatial frequencies f_x and f_y ,

$$x_2 = \frac{\lambda z f_x}{\sqrt{1 - \lambda^2(f_x^2 + f_y^2)}} \quad \text{and} \quad y_2 = \frac{\lambda z f_y}{\sqrt{1 - \lambda^2(f_x^2 + f_y^2)}} \quad (2.37)$$

x_2 and y_2 non-linearly depends on spatial frequencies f_x and f_y . Also, the condition $1 - \lambda^2(f_x^2 + f_y^2) > 0$ should be satisfied in the simulations by removing the negative or zero values of $1 - \lambda^2(f_x^2 + f_y^2)$ under the square root in the denominator.

2.3 Scalar methods for optical element modeling

2.3.1 Thin element approximation (TEA)

A phase element is considered to be thin if the incoming beam passes through the optical element with negligible deflection along the propagation direction [7]. Considering the thin

element approximation (TEA), the incoming beam U_1 in Fig. 2.3 only experiences a phase delay that is proportional to the optical element thickness $f(x, y; 0)$ in each point. The phase delay is expressed by,

$$\phi(x, y; 0) = kn f(x, y; 0) + k[\Delta - f(x, y; 0)] \quad (2.38)$$

Where n is the optical element refractive index. $kn f(x, y; 0)$ is the resulting phase delay because of the optical element and $k[\Delta - f(x, y; 0)]$ is the introduced phase delay in the remaining area in the air. As a result, the field U_2 immediately behind the optical element, can be calculated by multiplying the incoming beam U_1 with a transmission function $t(x, y)$,

$$U_2 = t(x, y) \cdot U_1 \quad (2.39)$$

Where the transmission function $t(x, y)$ describes the resulting phase transformation,

$$t(x, y) = \exp(i\phi) \quad (2.40)$$

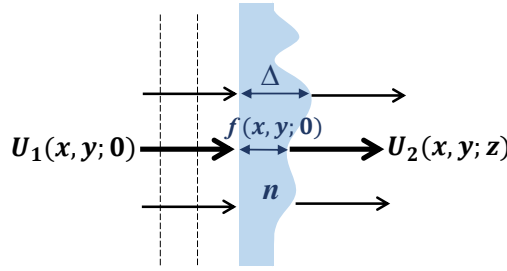


Figure 2.3: Thin element approximation (TEA). The incoming beam is considered to pass through the thin optical element without any deflection along the propagation direction.

In many design strategies for diffractive optics, TEA is used to specify the basic parameters of a configuration. Applying the TEA in simulations, the effect of diffraction inside the optical element is not included although, the method is not computationally costly. Instead, we can apply, scalar, or vectorial approaches for modeling the passage of the beam through the optical element. Here we introduce the scalar Fourier transform beam propagation method, in which the beam propagation inside the optical element is modeled, considering approximations.

2.3.2 Fourier transform Beam propagation method (FFT-BPM)

The Fourier transform beam propagation method (FFT-BPM) is a scalar numerical technique that applies the Fourier transform to solve the Helmholtz equation [9, 10]. As seen in Fig. 2.4, in this method the structure is divided into sub-sections along the propagation direction z . The spatial distribution of the refractive index n along the x and y axis in each sub-section is non-uniform; the non-uniform refractive index in each sub-section is described by $n(x, y) =$

$\bar{n} \pm \Delta n(x, y)$, where \bar{n} is an averaged refractive index and $\Delta n(x, y)$ is referred to a local refractive index change. Considering these assumptions, the beam propagation in each sub-section for a distance of Δz is expressed by

$$U(x, y, z + \Delta z) = FFT^{-1} \left[FFT \{U(x, y, z)\} \cdot e^{i\Delta z \sqrt{\bar{n}^2 k_0^2 - (k_x^2 + k_y^2)}} \right] \cdot e^{i\Delta z \cdot \Delta n(x, y) \cdot k_0} \quad (2.41)$$

Where k_0 is the wavenumber in air, k_x and k_y are the spatial frequencies along x and y axis. The expression in Eq. 2.41 splits into two propagators. The field is first propagated in a homogenous medium with a refractive index \bar{n} and a propagation distance Δz by applying the ASPW method. Then, a thin element approximation is performed to consider the phase delay due to the refractive index changes Δn along the x and y axis. Next, the fields are extracted and propagated in the subsequent layer. The process is done until the field is calculated in all the sub-sections of the optical element.

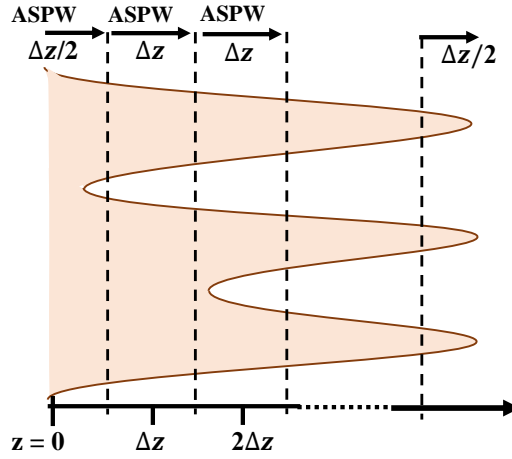


Figure 2.4: Fourier transform beam propagation method (FFT-BPM). The structure is divided into sub-sections; the field is propagated in each section by applying the ASP, and considering the local refractive index changes by applying the TEA.

The scalar FFT-BPM approach gives higher computational speed in comparison with the rigorous approaches such as FDTD and RCWA. However, this propagator is limited by some approximations. First, it is based on the paraxial approximation where $k_z^2 \gg k_x^2 + k_y^2$ [11]. Also, the effect of reflection between the subsequent layers is considered to be negligible. Moreover, the applicability of this method is limited to polarization independent structures. And finally, the refractive index modulation is considered to be small; meaning that $\delta n \ll n$. In this thesis, our structures are polarization-independent and are made of glass with a refractive index of 1.5. For this reason, applying FFT-BPM is practical for the configurations in which the effect of reflection is negligible. To perform FFT-BPM simulations, we use the VirtualLab fusion package [4]. In chapter 3, we will compare this technique with the rigorous FDTD method for thin and thick structures, by presenting simulated examples.

2.4 Discussions around the thesis problem

Here, we analytically calculate the diffraction pattern for the thesis configuration by applying scalar approximations. Our purpose in this part is to obtain an initial understanding of the interdependence of parameters. The calculations here are performed for 2D configurations and can be easily extended to 3D scenarios. As we earlier introduced the problem, the configuration is a refractive-diffractive optical element under a point source illumination. In our work, the point source is modeled by a single-mode Gaussian beam for low numerical aperture sources ($NA \approx 0.1$ to 0.15). For high NA sources, another model will be considered in chapter 6. The single-mode Gaussian beam complex amplitude at the focus is defined by:

$$u(x, z=0) = \exp\left[-\frac{x^2}{w_0^2}\right] \cdot \exp(-jkz) \quad (2.42)$$

Where w_0 is the beam waist of the Gaussian field at the focus. The problem under study is a single-mode Gaussian beam with a finite spatial dimension that illuminates a micro-lens array (MLA) of period p , as shown in Fig. 2.5. The observation plane is in the far-field. The distance between the source and the MLA is considered to be D . The Gaussian beam field distribution at $z = D$ immediately before the MLA can be calculated by solving the paraxial Helmholtz equation,

$$u(x, z) = \frac{w_0}{w(z)} \exp\left[-\frac{x^2}{w(z)^2}\right] \cdot \exp\left[-jkz - jk\frac{x^2}{2R(z)}\right] \quad (2.43)$$

Where $w(z)$ is the beam radius, $R(z)$ is the radius of curvature in the transverse coordinate x and $R(z) = z[1 + (kw_0^2/2z)^2]$.

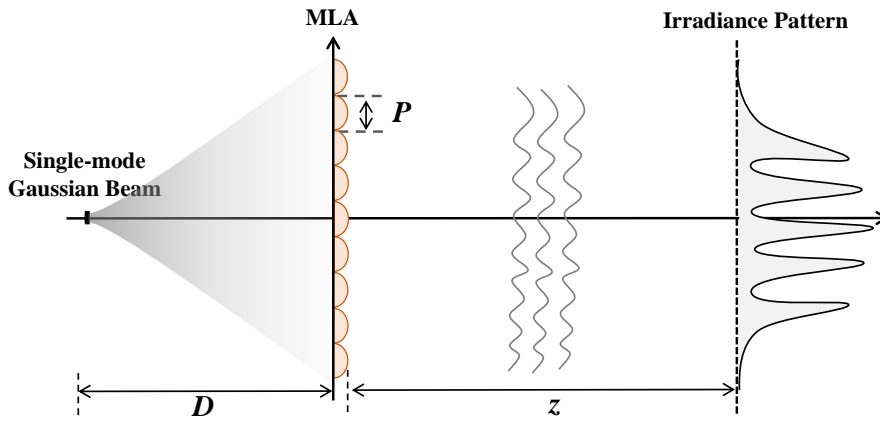


Figure 2.5: The configuration under study. An MLA with the period of P under a Gaussian beam illumination.

2.4.1 Analytical evaluation

According to the configuration in Fig. 2.5, the simulation has three steps. The first step is the Gaussian beam propagation for the distance D from the source to the plane immediately before the MLA. The second step is the propagation inside the MLA. And the third step is the field propagation from MLA to the far-field observation plane. Here, we calculate the far-field distribution analytically by applying the TEA in the MLA region. Figure 2.6 demonstrates a diagram of the source propagating to the far-field observation plane. The Gaussian beam complex field at $z = D^-$ is calculated according to Eq. 2.43. The field at $z = D^+$ is the complex field at $z = D^-$ multiplied by the phase shift generated by the MLA using the TEA. The far-field distribution at $z = D + Z$ is determined by taking the Fourier transform from the near-field at $z = D^+$, assuming the Fraunhofer approximation.

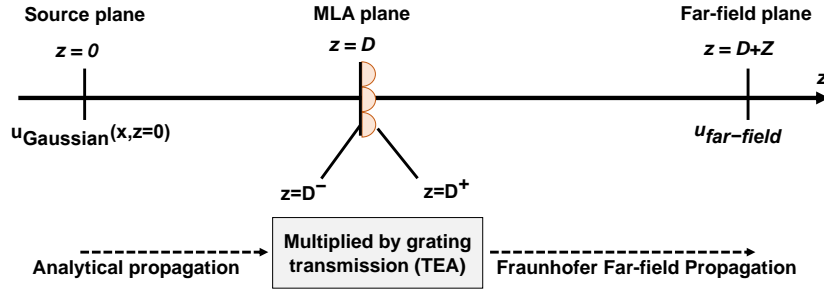


Figure 2.6: A Diagram of propagators that are applied to calculate the field in the observation plane for configuration in Fig. 2.5.

Using the TEA, the complex field at $z = D^+$ is described by

$$E(x, z = D^+) = E_{\text{GaussianBeam}}(x, z = D^-) \cdot \exp[-jk(n-1)H], \quad (2.44)$$

Where n is the MLA refractive index which is assumed to be 1.5 for glass and H is the height profile of the MLA versus x . The phase delay generated by MLA can be described by

$$\exp[-jk(n-1)H] = \left[t(x) \cdot \text{rect}\left(\frac{x}{P}\right) \right] * \text{comb}\left(\frac{x}{P}\right), \quad (2.45)$$

where $t(x)$ is the phase delay generated for one period of MLA by applying the TEA. By substituting Eq. 2.45 in Eq. 2.44, the field in the observation plane is calculated by

$$E_{\text{far-field}}(x, z = Z + D) = \frac{\exp(-jkz)}{j\lambda z} \cdot \exp\left(-\frac{jkx^2}{2z}\right) \times \text{FFT} \left[E_{\text{GaussianBeam}}(x, z = D^-) \cdot \left\{ \left[t(x) \cdot \text{rect}\left(\frac{x}{P}\right) \right] * \text{comb}\left(\frac{x}{P}\right) \right\} \right] \quad (2.46)$$

By rewriting the Fourier transform in convolution form,

$$E_{\text{far-field}}(x, z = Z + D) = \frac{\exp(-jkz)}{j\lambda z} \cdot \exp\left(-\frac{jkx^2}{2z}\right) \cdot \left[E_{\text{GaussianBeam}}\left(x, \frac{z}{\lambda Z}\right) * FFT\left[\left\{t(x) \cdot \text{rect}\left(\frac{x}{P}\right)\right\} * \text{comb}\left(\frac{x}{P}\right)\right] \right] \quad (2.47)$$

The FFT in this equation represents the diffracted field if the source is a plane wave illumination. By simplifying the FFT in Eq. 2.47, the complex field is obtained as follows,

$$E_{\text{far-field}}(x, z = Z + D) = \frac{\exp(-jkz)}{j\lambda z} \cdot \exp\left(-\frac{jkx^2}{2z}\right) \cdot \left[E_{\text{GaussianBeam}}\left(x, \frac{z}{\lambda Z}\right) * \left[\left\{ FFT(t)\left(\frac{x}{\lambda Z}\right) * \text{sinc}\left(\frac{Px}{\lambda Z}\right) \right\} \times \text{comb}\left(\frac{Px}{\lambda Z}\right) \right] \right] \quad (2.48)$$

Considering the $\text{comb}(Px/\lambda Z)$, the pattern period is $\lambda z/P$ that confirms the diffraction theory. Moreover, under paraxial approximation, the convolution between the comb function and the scaled Gaussian beam in the observation plane is physically interpreted as a periodical imaging of the source near-field in the observation plane via the MLA. Also, the $FFT(t)\left(\frac{x}{\lambda Z}\right) * \text{sinc}\left(\frac{Px}{\lambda Z}\right)$ is slowly varying compared to the comb function. It means that the pattern envelope is controlled by the lens curvature. In summary, analytical Eq. 2.48 demonstrates that

1. The period of pattern distribution in the far-field is controlled by the source wavelength λ , as well as MLA period P .
2. The pattern envelope is controlled by the lens curvature.
3. The dots size in the observation plane is dependent on the source near-field distribution and also the size of the illumination spot on MLA.

Also, to obtain a high-contrast pattern, the distance D between the source and the MLA is required to be Lau distance, as we explained in the introduction chapter.

Although our analytical calculations are based on paraxial approximation, it gives us an insight into interdependence among the parameters and is a good starting point for applying new ideas. In this work, we will study two strategies for modifying the diffracted pattern in the far-field: changing the periodic optical element curvature and modulating the source near-field. We first evaluate the contrast of pattern by changing the distance D and choose the distance in which we obtain a high contrast pattern in the far-field. Next, we will focus on the effect of periodic optical element curvature especially for modifying the pattern envelope and increasing the number of dots in the pattern. We consider a sinusoidal phase grating instead of a lens array, in this case. In the last part of the thesis, we will study the effect of source near-field modulation by applying an optical element such as a dielectric microsphere around

the source near-field and compare the pattern distributions that are generated under different illumination conditions.

References

- [1] J. B. Schneider. “Understanding the finite-difference time-domain method”. *School of electrical engineering and computer science Washington State University*:28, 2010.
- [2] M. Moharam, D. A. Pommet, E. B. Grann, and T. Gaylord. “Stable implementation of the rigorous coupled-wave analysis for surface-relief gratings: enhanced transmittance matrix approach”. *JOSA A*, 12(5):1077–1086, 1995.
- [3] F. Solutions. “Lumerical solutions inc”. *Vancouver, Canada*, 2003.
- [4] W. V. Fusion. “Lighttrans gmbh, jena, germany”.
- [5] K. Yee. “Numerical solution of initial boundary value problems involving maxwell’s equations in isotropic media”. *IEEE Transactions on antennas and propagation*, 14(3):302–307, 1966.
- [6] B. E. Saleh and M. C. Teich. *Fundamentals of photonics*. john Wiley & sons, 2019.
- [7] J. W. Goodman. *Introduction to Fourier optics*. Roberts and Company Publishers, 2005.
- [8] V. Arrizón, M. Testorf, S. Sinzinger, and J. Jahns. “Iterative optimization of phase-only diffractive optical elements based on a lenslet array”. *JOSA A*, 17(12):2157–2164, 2000.
- [9] M. Feit and J. Fleck. “Light propagation in graded-index optical fibers”. *Applied optics*, 17(24):3990–3998, 1978.
- [10] W. Eckstein, E.-B. Kley, and A. Tünnermann. “Comparison of different simulation methods for effective medium computer generated holograms”. *Optics express*, 21(10):12424–12433, 2013.
- [11] M. Fertig and K.-H. Brenner. “Vector wave propagation method”. *JOSA A*, 27(4):709–717, 2010.

3 Structured pattern generation for 1D sinusoidal phase grating

We investigate here micro-optical elements with a period of 75λ which allows us to control both diffractive and refractive effects [1]. Using a regular micro-optical element such as a lens array under plane wave illumination, one obtains a periodic pattern in the far-field with the period of $\sim\lambda/P$ according to the diffraction theory. To increase the numbers of diffraction orders, one solution is to increase the lens array period P . By increasing the period P , the refraction becomes predominant and the effect of diffraction is reduced which is not desirable. Alternatively, introducing a point source instead of plane wave, the periodic element field distribution would reproduce in the far-field including a magnification factor for certain distances between the source and the periodic element based on the known self-imaging phenomenon [2, 3], as it is mentioned in the introduction chapter. Numbers of publications are devoted to using this phenomenon for pattern generation using a lens array in which the point source is modeled by a single-mode Gaussian beam [4, 5].

3.1 Configuration

In this chapter, we make use of the self-imaging phenomenon under point source illumination for a sinusoidal phase grating. We investigate the pattern generation using a 1D sinusoidal phase grating. The configuration is a sinusoidal phase grating with a period of P and a thickness of h under a single mode TEM Gaussian beam illumination, as shown in Fig. 3.1(a). The phase grating thickness h is much higher than the wavelength ($h \gg \lambda$). All the simulations in this chapter are 2D.

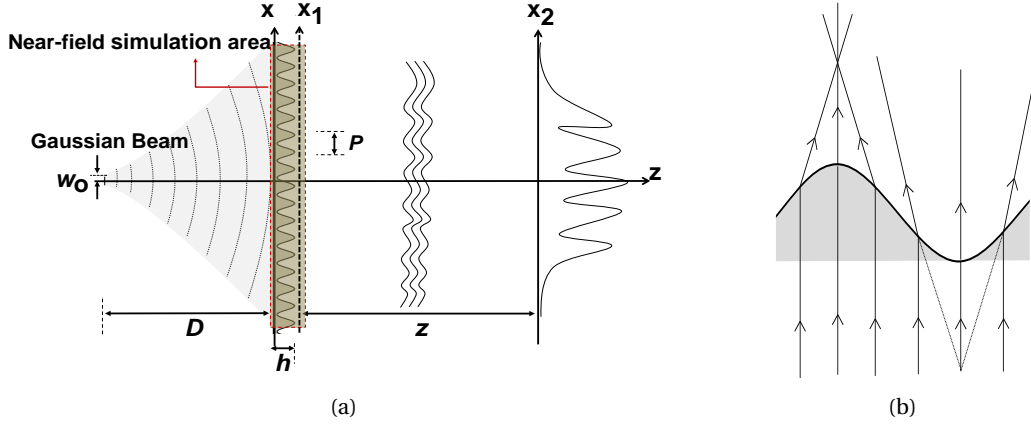


Figure 3.1: (a) Configuration under study, (b) Ray tracing for one period of a sinusoidal phase grating which shows two different focal points in one period

3.2 Why the sinusoidal shape?

In this section, we compare the far-field distribution when a sinusoidal phase grating is illuminated by a point source and a plane wave[6] analytically using self-imaging theory to show the reason behind choosing the sinusoidal curvature. We use TEA for a principle design and show how more numbers of points in the far field can be generated for point source. The effect is based on self-imaging[2, 4]. Figure 3.2 gives a diagram of the point source propagating to the far-field observation plane. For a clear understanding of the self-imaging phenomenon for point source illumination, we use the notation and formulas as found in [2].

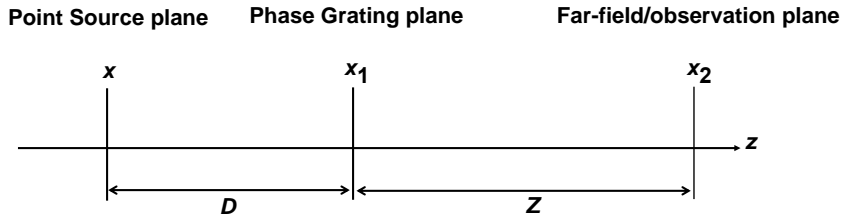


Figure 3.2: Schematic of analytical calculation propagators for point source illumination.

The far-field is given by the following integral

$$E_{far-field}(x_2, z = Z + D) = C_1 \left[E(x_1, z = D^+) * \exp\left(\frac{i\pi}{\lambda z} x_1^2\right) \right] \quad (3.1)$$

C_1 is a constant complex value.

Using the TEA, the complex field at $z = D^+$ is described by

$$E(x_1, z = D^+) = E_{source}(x_1, D^-) \cdot \exp[-ik(n-1)H] \quad (3.2)$$

and

$$E_{source}(x_1, z = D^-) = E_{source}(x_1, z = 0) * \exp\left(\frac{i\pi}{\lambda D} x_1^2\right) \quad (3.3)$$

n is the refractive index of the phase grating which is assumed to be 1.5. H is the height profile of the phase grating and a function of position in x . The height profile H for the sinusoidal surface is defined as

$$H = \frac{h}{2} \times \left(\sin \frac{2\pi x}{P} \right) + \frac{h}{2} \quad (3.4)$$

Where P is the phase grating period and h is the phase grating thickness. The exponential term in Eq. (3.2) can be written in the following Fourier series

$$\exp\left[-0.5ik\frac{h}{2} \sin\left(\frac{2\pi}{P}x\right)\right] = \sum_{q=-\infty}^{+\infty} J_q\left(-0.5k\frac{h}{2}\right) \times \exp\left(2\pi i q \frac{x}{P}\right) \quad (3.5)$$

Based on [2], the far-field for a point source meaning $E_{source}(x, z = 0) = \delta(x)$ can reproduce the object phase modulation for certain values of D . For $D = \frac{P^2}{\lambda}$, the far-field can be written as the following summation

$$E_{far-field}(x_2, z = Z + D) = C_2 \exp\left(\frac{i\pi}{\lambda z} x_2^2\right) \sum_{q=-\infty}^{+\infty} J_q\left(-0.5k\frac{h}{2}\right) \exp\left(2\pi i q \frac{Dx_2}{zP}\right) (-1)^{q^2} \quad (3.6)$$

According to this equation, the phase modulation which is generated by a sinusoidal phase grating is reconstructed although they are not exactly the same. To clarify more, we expand the equation in the following form

$$\begin{aligned} \sum_{q=-\infty}^{+\infty} J_q\left(-0.5k\frac{h}{2}\right) \exp\left(2\pi i q \frac{Dx_2}{zP}\right) (-1)^{q^2} &= J_0 - 2i \left[J_1 \sin\left(\frac{2\pi D}{zP}x\right) + J_3 \sin\left(\frac{6\pi D}{zP}x\right) \right. \\ &\quad \left. + J_5 \sin\left(\frac{10\pi D}{zP}x\right) + \dots \right] + 2 \left[J_2 \cos\left(\frac{4\pi D}{zP}\right) + J_4 \cos\left(\frac{8\pi D}{zP}\right) + J_6 \cos\left(\frac{12\pi D}{zP}\right) + \dots \right] \end{aligned} \quad (3.7)$$

This equation demonstrates that the real and imaginary parts of the summation are reconstructed in the far-field using cosine and sine functions, respectively. We calculate this approximation series for $\lambda = 650 \text{ nm}$, $P = 50 \text{ }\mu\text{m}$, $z = 1 \text{ m}$ and $h = 12 \text{ }\mu\text{m}$. Now we can compare the phase modulation generated by a sinusoidal phase grating using TEA with the series in Eq. (3.7). The result is shown in Fig. 3.3. As seen, the phase modulations are comparable except

that one graph is flipped around x axis and the scale in x has changed. The sinusoidal phase grating modulation is imaged in the far-field. Interestingly this leads to the appearance of two peaks in one period of the far-field pattern. We will investigate this effect in more detail in the simulation part.

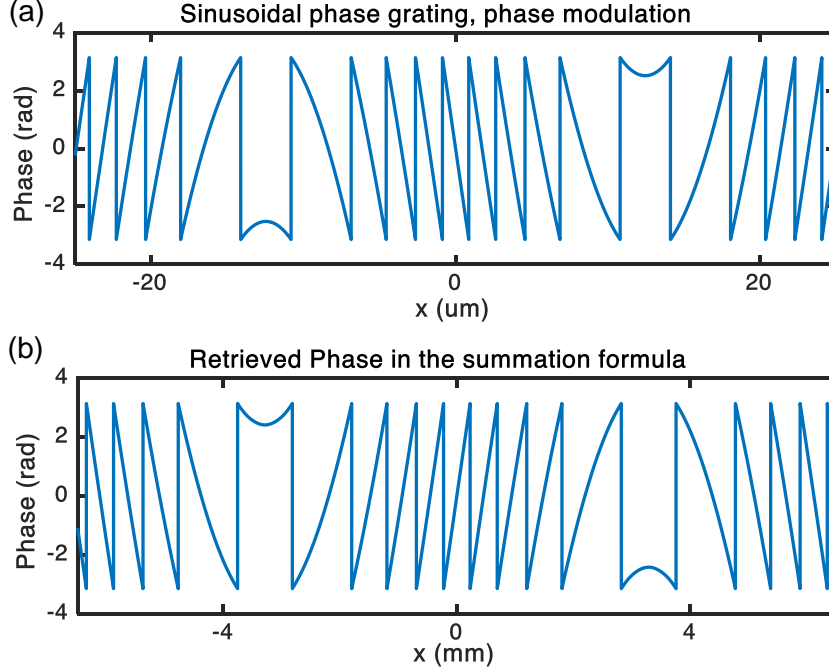


Figure 3.3: (a) Phase modulation generated by the sinusoidal phase grating using TEA, (b) The retrieved phase in the far-field according to eq. (3.7).

Now, we consider the sinusoidal phase grating under the plane wave illumination. For the plane wave illumination, the far-field pattern is simply the Fourier transform of the sinusoidal phase modulation based on TEA

$$E_{far-field} = FT \left\{ \exp \left[-0.5ik \left(\frac{h}{2} \times \sin \left(\frac{2\pi x}{P} \right) + \frac{h}{2} \right) \right] \right\} \quad (3.8)$$

Writing the exponential term in the summation form of Eq.(3.5) and taking the Fourier transform, the far-field is

$$E_{far-field} = \sum_{q=-\infty}^{+\infty} J_q \left(-0.5k \frac{h}{2} \right) \delta \left(\frac{x}{\lambda z} - \frac{q}{P} \right) = \dots + J_{-1} \left(-0.5k \frac{h}{2} \right) \delta \left(x + \frac{\lambda z}{P} \right) + J_0 \left(-0.5k \frac{h}{2} \right) \delta(x) + J_1 \left(-0.5k \frac{h}{2} \right) \delta \left(x - \frac{\lambda z}{P} \right) + \dots \quad (3.9)$$

This equation is the summation of delta functions with the period of $\lambda z/P$, which is the diffraction angle. It demonstrates that there is one peak in each diffraction angle period of

$\lambda z/P$ under the plane wave illumination. For a point source by making use of the self-imaging, the sinusoidal phase grating modulation is imaged to the far-field and generates two peaks within the same period. It is worth to note that the pattern envelope highly depends on the phase grating thickness h because of the Bessel function of $J_q(-0.5k\frac{h}{2})$ in equations (3.7) and (3.9). Furthermore, it becomes clear that the source characteristics are of great importance. To approach a real case scenario we replace the point source with a single-mode Gaussian beam in our following models. In the rest of this chapter, we investigate the effect of the size of the Gaussian beam waist and the phase grating thickness h , which are the key factors that influence the far field irradiance pattern. In all the simulations we keep the period of phase grating P fixed.

3.3 Diffractive/refractive element simulations

Consider a Gaussian beam with a finite spatial dimension that illuminates a sinusoidal phase grating of period P , as shown in Fig. 3.1(a). The observation plane is in the far-field and we aim to generate high contrast patterns. As we discussed in the previous section, for particular values of the distance D , high contrast intensity peaks are observed because of interference effects of the curved wavefront and the grating [2, 5]. We choose D to fulfill the self-imaging condition to be 3.84 mm for a period $P = 50 \text{ }\mu\text{m}$ in all simulations. As a source, a single-mode Gaussian beam with $\lambda = 650 \text{ nm}$ is chosen.

According to our configuration in Fig. 3.1(a), the simulation is approached in three steps. The first step is the Gaussian beam propagation for the distance D from the source to the phase grating. Immediately before the phase grating, one finds an amplitude and phase distribution which can be calculated using the single mode Gaussian beam formula. The second step is the propagation inside the phase grating. There are different means depending on the complexity and dimensions of the structure. We use three methods: thin element approach TEA, beam propagation method FFT-BPM and the rigorous FDTD method. In the thin element approach TEA, phase profiles are used that are calculated from the local phase difference a structure will produce. In our case, there is no amplitude variation as we consider a pure phase grating. The thin element approach is known to deliver false results for high spatial frequency diffractive optical elements or thick elements but is useful to obtain basic specifications of the systems.

3.3.1 Variable source beam waist

In this section, we explore the dot pattern generation in the far field under the diverging Gaussian beam in comparison with the plane wave illumination. We investigate the effect of the source divergence angle on the irradiance pattern and compare TEA, FFT-BPM for modeling the passage of the beam through the thin phase grating of $12 \text{ }\mu\text{m}$. The Fraunhofer approximation is applied for the far-field calculation of this thin periodic phase grating. For the plane wave illumination, the simulation dimension along the x -axis is 3 mm .

Thin element approach (TEA) calculations

In Fig. 3.4(a) and (b), the irradiance patterns for a plane wave in comparison to the Gaussian beam with the beam waist of $2\ \mu\text{m}$ are given. The pattern period matches in both cases the diffraction theory: a period of $50\ \mu\text{m}$ for $\lambda = 650\text{nm}$ delivers 0.74° diffraction angle. Under plane wave illumination, the energy is not uniformly distributed over the diffraction orders. When comparing the inset of Fig. 3.4(a), a number of peaks have almost zero intensity and the field of view is small in comparison to the Gaussian beam illumination in Fig. 3.4(b). However, as we discussed in the analytical part for the Gaussian beam, two non-equal peaks with a period of 0.74° are repeated in the pattern as it is seen in the inset figure of 3.4(b). The two series of peaks have different intensities and diameters. They are caused by the convex-concave curvature form of the sinusoidal phase grating which can be interpreted as a combination of concave and convex lenses, as it was shown in Fig. 3.1(b). Assuming the Gaussian beam as a spectrum of plane waves with different incident angles allows interpreting the increase of the field of view when compared to the plane wave illumination.

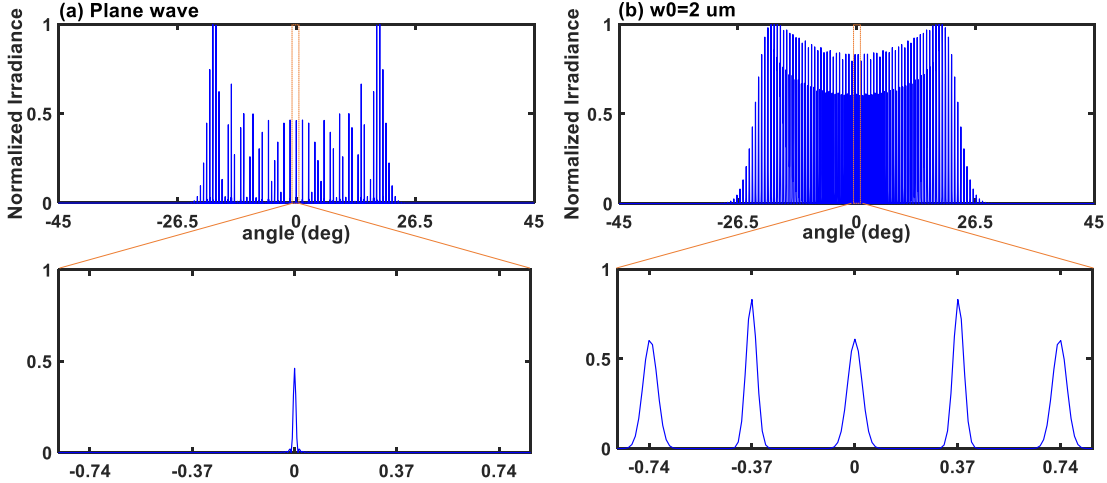


Figure 3.4: Irradiance pattern using TEA for (a) plane wave illumination and (b) Gaussian beam with the beam waist of $2\ \mu\text{m}$.

In Fig. 3.5 the irradiance patterns are illustrated for the Gaussian beam waists $w_0 = 1, 2$ and $3\ \mu\text{m}$ in comparison to plane wave illumination using the TEA. The pattern field of view increases by decreasing the source beam waist down to $1\ \mu\text{m}$. Enlarging the pattern field of view is more pronounced from 2 to $1\ \mu\text{m}$ beam waist in comparison with 3 to $2\ \mu\text{m}$ beam waist. The reason is that the Gaussian beam divergence angle is proportional with $1/w_0$ and it indicates that the divergence angle increment is higher from 2 to $1\ \mu\text{m}$ in comparison with 3 to $2\ \mu\text{m}$ beam waist which results in a more pronounced enlargement in the pattern field of view.

3.3. Diffractive/refractive element simulations

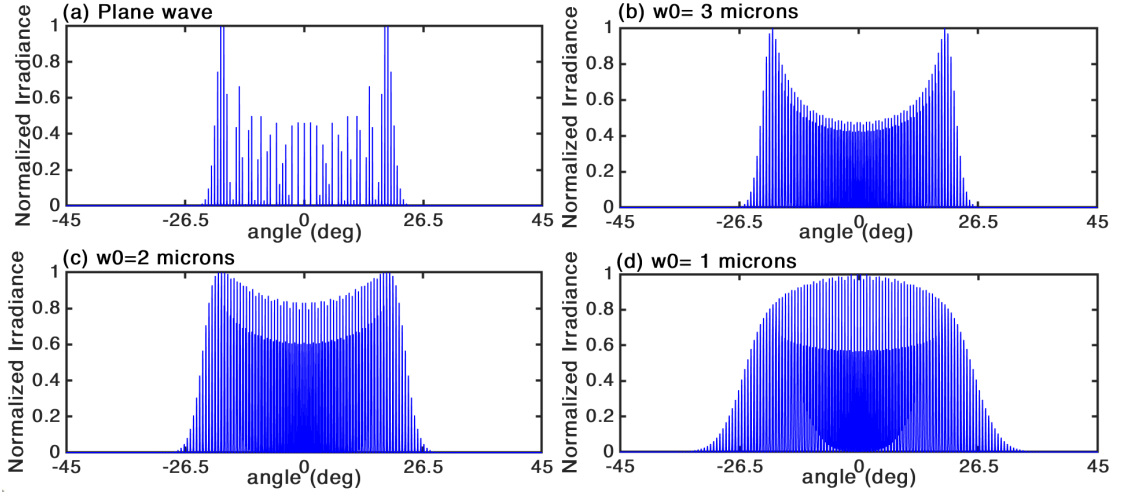


Figure 3.5: Irradiance pattern using TEA for (a) Plane wave and the Gaussian beam with the beam waist of (b) $3\ \mu\text{m}$, (c) $2\ \mu\text{m}$ and (d) $1\ \mu\text{m}$.

To explore the effect of the Gaussian beam waist w_0 on the irradiance pattern in more detail, we calculate the pattern envelope in the far field which is the Fourier transform of one single period of the phase grating near field. Our configuration is sketched in Fig. 3.6 (a) and we illuminate only one single period of the phase grating with a Gaussian beam with $1\ \mu\text{m}$ beam waist. If the element is centered the result is a symmetric distribution of peaks as visible in Fig. 3.6(b). Next, we move the element along x -axis to probe the influence of the tilted local phase and compare the pattern envelope for different positions at $-400\ \mu\text{m}$ and $-800\ \mu\text{m}$. As seen in Fig. 3.6 (b), the pattern envelope moves in the observation plane by moving the optical element along x -axis because of the tilted source phase profile. This clearly shows the reason for an increased field of view: the different illumination angles that are present in the Gaussian beam.

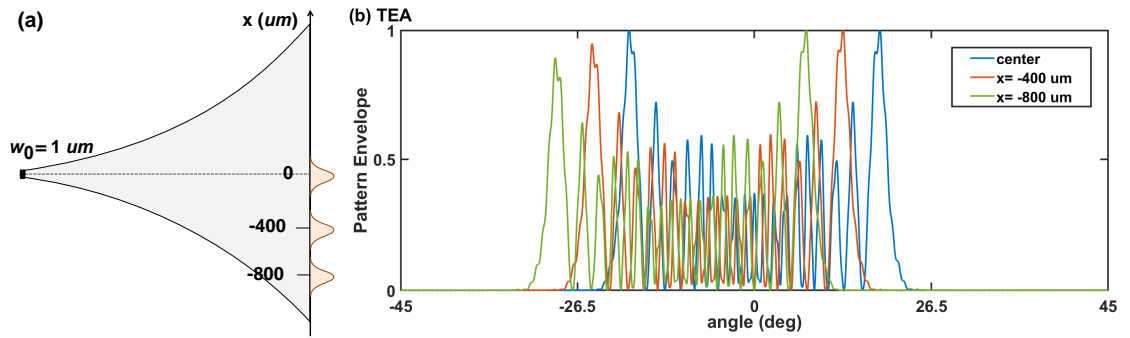


Figure 3.6: (a) Moving one single period of the phase grating along the x -axis and (b) taking the Fourier transform from near field to obtain the pattern envelope for $x = 0$, -400 and $-800\ \mu\text{m}$.

TEA versus FFT-BPM

For the thin phase grating of $12\ \mu\text{m}$ thick, using a rigorous method is not required but using a propagator like FFT-BPM which includes the beam propagation inside the structure including some approximations is necessary for evaluating the TEA results. In Fig. 3.7, we compare the irradiance patterns using TEA and FFT-BPM for the Gaussian source beam waists $w_0 = 1, 2$ and $3\ \mu\text{m}$ and a plane wave. The major difference for FFT-BPM is that the effects that arise because of the propagation through a certain thickness of the structure are now considered. As seen, for the plane wave illumination, FFT-BPM predicts a wider field of view in comparison with the TEA although the pattern envelope is still similar. For the Gaussian beam illumination using the FFT-BPM method, both the pattern field of view and the pattern envelope differ significantly from the TEA. It demonstrates that the TEA is not accurate even for a rather shallow surface profile of $12\ \mu\text{m}$ thickness and the field of view calculated with FFT-BPM is about 20% wider.

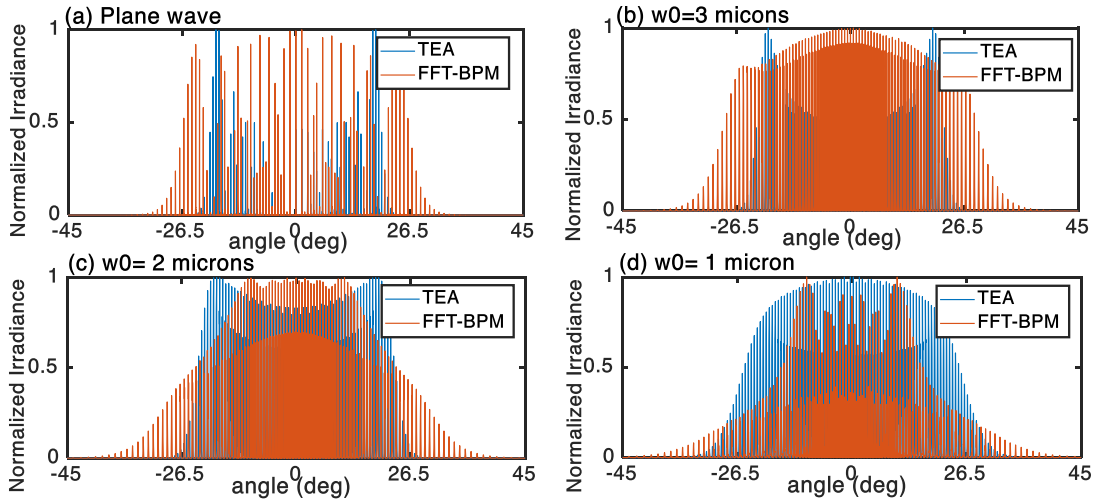


Figure 3.7: Normalized far-field irradiance using TEA and FFT-BPM under (a) plane wave and Gaussian beam with the beam waist of (b) $3\ \mu\text{m}$, (c) $2\ \mu\text{m}$ and (d) $1\ \mu\text{m}$.

Transmission

One important practical criterion is the total transmission of the phase grating. We define the transmission as the normalized transmitted power immediately after the phase grating with respect to the source power immediately before the phase grating. As mentioned in the beginning, different effects influence transmission such as total internal reflection. Figure 3.8 shows the transmission versus the source beam waist w_0 using the FDTD simulation. As seen, by increasing the source beam waist w_0 the transmission increases until it reaches a constant value which is identical with the transmission for the Plane-wave illumination. As

the Gaussian beam divergence angle is proportional to $1/w_0$, small changes in w_0 for $w_0 \rightarrow 0$ correspond to big changes in divergence angle and as a result large changes in transmission. Thus for $w_0 < 3\mu m$, the smaller the beam waist the lower the transmission (maximum 4% reduction in transmission). On the other side according to Fig. 3.7, the smaller the beam waist the higher the field of view. It demonstrates a trade-off between obtaining higher transmission and higher field of view for small source beam waist w_0 .

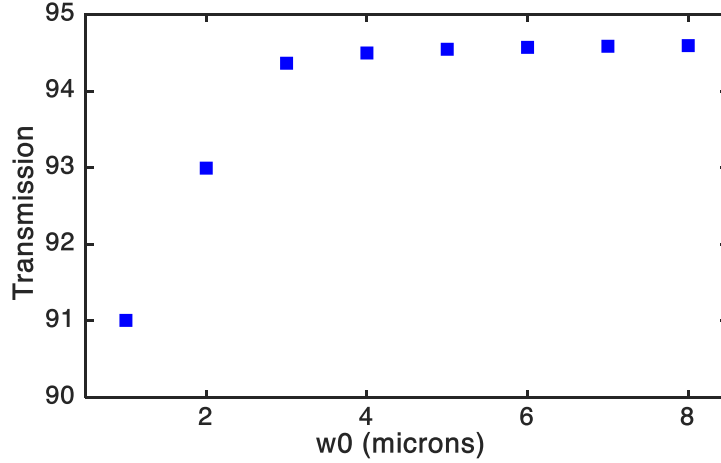


Figure 3.8: Transmission versus source beam waist.

3.3.2 Variable Phase profile thickness h

In the previous section, we have shown that even for the small height of the sinusoidal phase grating, one obtains large numbers of peaks with a uniform distribution. The thickness of the structure also plays an important role in the design and may generate a bigger field of view. In this section, we, therefore, compare the irradiance pattern for different structure heights and three aspect ratios of $h/P = 0.24, 0.5$ and 1 for $P = 50\mu m$ that represents the transition between thin to thick gratings. For thick structures, a careful analysis needs to be done as the non-uniform illumination condition modifies the angular spectrum of the arriving wavefront and hence influences the far-field pattern. As we discussed in the previous section, TEA is not enough accurate even for thin phase gratings and we concentrate here on comparing the FFT-BPM and FDTD and discuss their accuracies for different thicknesses. The source beam waist is fixed at $w_0 = 2\mu m$ for all the simulations.

Near field simulations, FFT-BPM versus FDTD

In Figure 3.9, the field amplitude is shown around the structure for different $h/P = 0.24, 0.5$ and 1 ratios. As one can see heavy amplitude modulations can be noticed and two hot spots are observed behind the structure. The structure seems to behave like lenses and the hotspots move toward the phase grating surface by increasing the thickness h . For thin height $h = 12\mu m$,

the near field is the same using the FFT-BPM and FDTD as the effect of reflection is negligible. As seen in Fig 3.9 (b) and (c) by increasing h , near field distribution is more complicated due to the effect of reflections. Especially for the height of $25 \mu m$, we observe that some of the beams that are transmitted using FFT-BPM, are reflected back using FDTD and it significantly changes the near-field distribution.

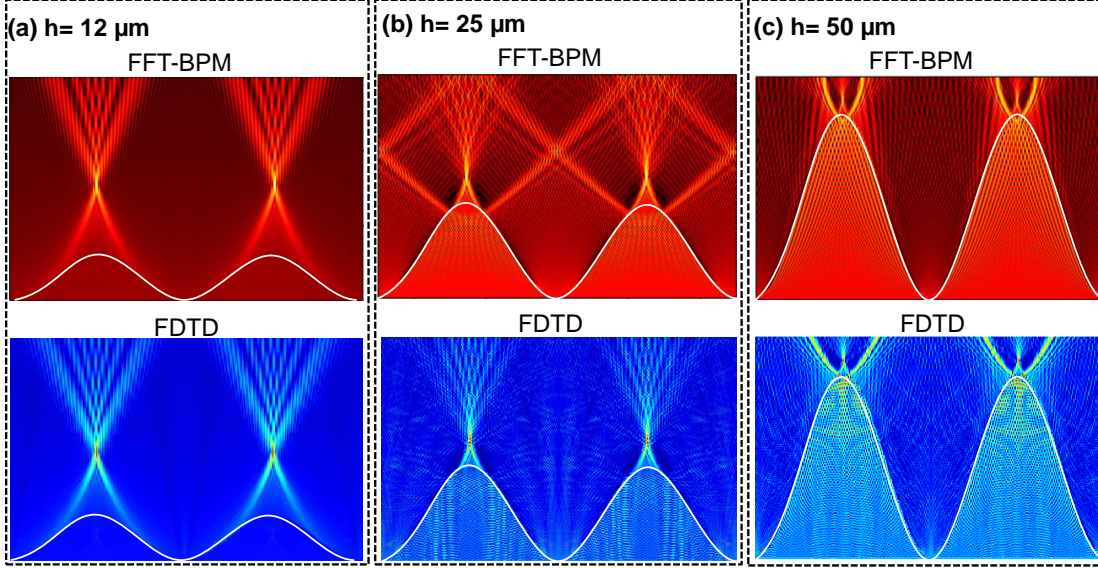


Figure 3.9: Near-field simulation using FFT-BPM and FDTD for (a) $h/P = 0.24$, (b) 0.5 and (c) 1 .

The near-field simulations demonstrate that both the phase grating thickness and surface profile remarkably influence the near field distribution for thick sinusoidal phase gratings. The near field simulation done by FFT-BPM is not enough accurate for thick sinusoidal phase gratings as it is still based on some approximations and does not take into account the effect of reflection. In the following section, we will determine the limits of using FFT-BPM by comparing it with FDTD.

Far-field simulations, Fraunhofer versus High NA propagator

One of the problems in determining the correct field of view of a diffractive structure is the validity of the far-field propagator. For large fields, a simple Fourier transform might not be valid anymore to describe the situation correctly. In this section, we investigate the validity of using the Fraunhofer approximation in comparison with the high NA propagator for thin and thick sinusoidal phase gratings. We start by showing in Figure 3.10 the near field and far field simulations for a grating height of $h = 12 \mu m$. As seen, the near field amplitude and phase distributions are the same using FFT-BPM and FDTD. The far-field patterns are similar using Fraunhofer and high NA approximations because the pattern field of view does not go far beyond the paraxial approximation and most of the energy is distributed in $+/- 25^\circ$

angles which $\sin(\theta) \cong \theta$ with less than 5% error. Nevertheless, the pattern field of view is slightly bigger using the high NA propagator. The pattern envelope is also calculated by taking the Fourier transform from one single period of phase grating near-field at $x = 0$ which is basically the pattern envelope under the plane wave. By comparing the pattern envelope and the irradiance pattern, we can observe how the Gaussian beam modifies and smoothens the energy distribution over the peaks.

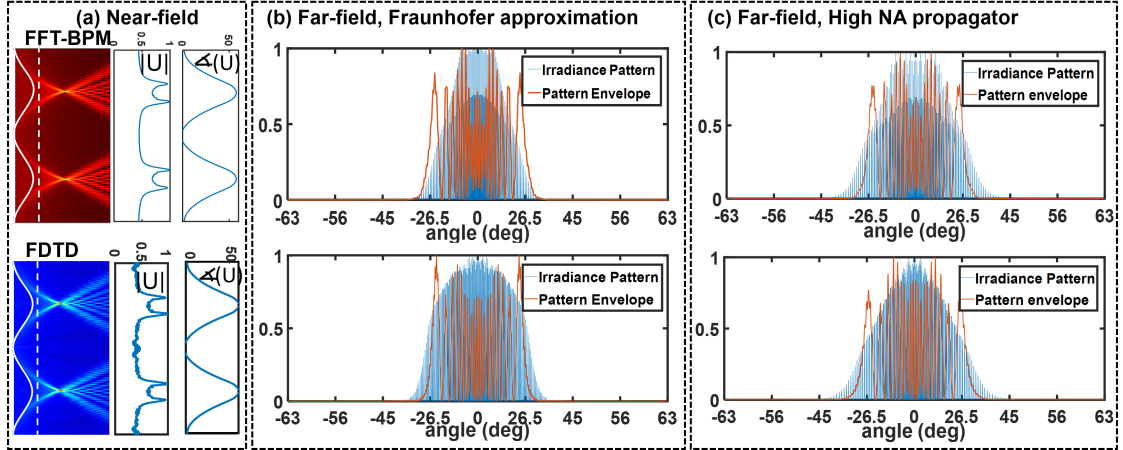


Figure 3.10: Near field and far field for $h = 12 \mu m$. (a) Near field distribution using FFT-BPM and FDTD and near field line plot of the amplitude and phase distribution. The corresponding far-field distributions and pattern envelopes using (b) Fraunhofer approximation and (c) high NA approximation.

In Fig.3.11, the far-field patterns are compared using the Fraunhofer approximation and high NA propagator for both the FFT-BPM and FDTD near field simulations for $h = 25 \mu m$. As seen in Fig 3.11 (a), the amplitude and phase near field distributions are different using FFT-BPM and FDTD. According to Fig 3.11 (b), the far-field distributions using Fraunhofer approximation for FFT-BPM and FDTD are similar although their near-field distributions are different. In Fig 3.11 (c) the far-field pattern using the high NA propagator is totally different for the FDTD near-field simulation in comparison with the FFT-BPM. Especially the peaks in the far-field pattern at around $\pm 45^\circ$ vanish for the FDTD calculations using the high NA propagator.

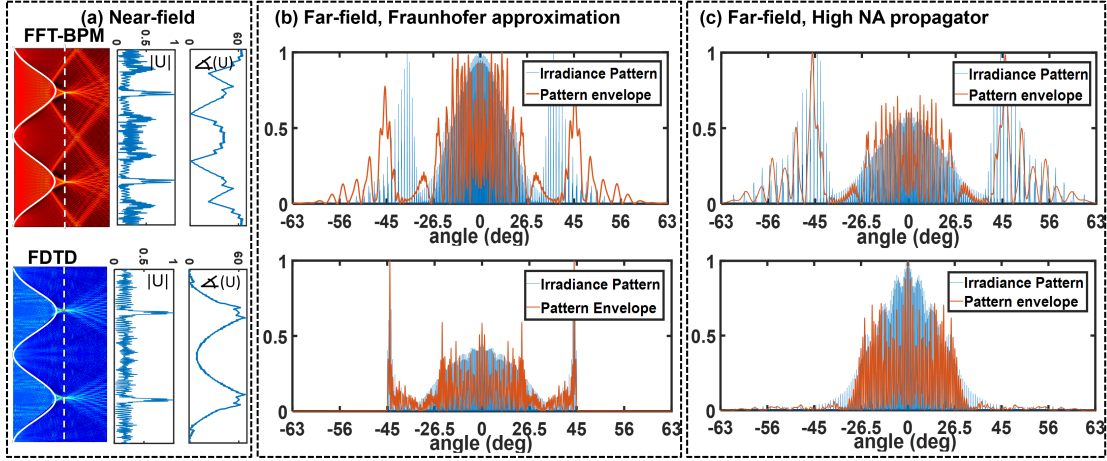


Figure 3.11: Near field and far field for $h = 25 \mu m$. (a) Near field distribution using FFT-BPM and FDTD and near field line plot of the amplitude and phase distribution. The corresponding far-field distributions and pattern envelopes using (b) Fraunhofer approximation and (c) high NA approximation.

The far-field distributions for the grating height of $h = 25 \mu m$ indicate that the Fraunhofer propagator is not valid because the pattern field of view goes beyond the paraxial approximation and using a non-paraxial far-field propagator is necessary to obtain the correct field of view. Also, it is demonstrated that obtaining the same far-field distribution for the FFT-BPM and FDTD near field simulations (as shown in Fig 3.11 (b)) does not guarantee the validity of the used near field and far-field approximations.

In Fig. 3.12, the near field and far-field patterns are compared for $h = 50 \mu m$. As seen in Fig 3.12 (a), the near field phase distribution is different using the FFT-BPM and FDTD. According to Fig. 3.12 (b) for the Fraunhofer approximation, the null in the center of the pattern is deeper using the FDTD in comparison with the FFT-BPM. In Fig 3.12 (c) using the high NA propagator, the null in the center of the pattern is much wider using the FDTD in comparison with the FFT-BPM. Finally, Fig. 3.11 and 3.12 demonstrate that both the amplitude and phase near field modulations determine the far-field distribution. Also, a rigorous method (eg. FDTD) should be used to find the correct near-field distribution for thick sinusoidal phase grating and FFT-BPM is not valid for thick phase gratings of more than 0.5 aspect ratio. Besides, the paraxial approximation is not valid in the far-field observation plane for thick sinusoidal phase gratings.

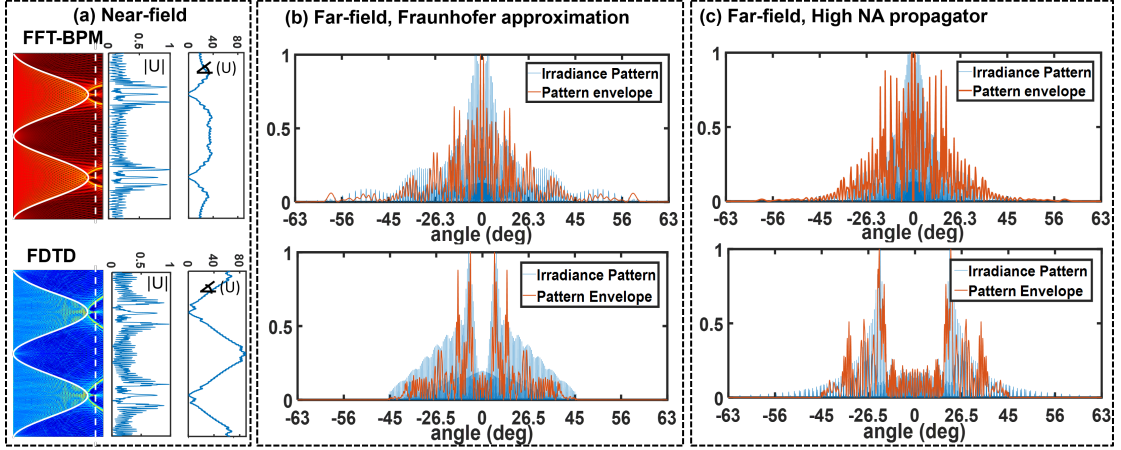


Figure 3.12: Near field and far field for $h = 50 \mu m$. (a) Near field distribution using FFT-BPM and FDTD and near field line plot of the amplitude and phase distribution. The corresponding far-field distributions and pattern envelopes using (b) Fraunhofer approximation and (c) high NA approximation.

Evaluation of the spot generators

In this section, we compare the performance of our gratings of different heights (12, 25 and $50 \mu m$) as spot generators. The distribution for $50 \mu m$ thickness is very non-uniform and not a practical point generator. To compare the 12 and $25 \mu m$ height, the pattern uniformity and the number of peaks are applied, as the criterion. We calculate three critical parameters for the patterns. The first parameter is the pattern intensity standard deviation which measures uniformity. The second and the third parameters are the number of points in the pattern and the pattern field of view (FOV). We consider only dots intensities higher than 13% of the maximum intensity. Table 3.1 summarizes the findings. As seen, for $25 \mu m$ thick phase grating, 165 numbers of points in a $\pm 30^\circ$ FOV is realized which is a better point generator compared to a $12 \mu m$ thick phase grating.

Table 3.1: Pattern standard deviation and numbers of points for 12 and $25 \mu m$ thicknesses .

$h(\mu m)$	Standard deviation	Number of points in the pattern	FOV
12	0.008	142	$\pm 26^\circ$
25	0.0038	165	$\pm 30^\circ$

3.3.3 Transmission versus phase grating thickness using FDTD

Reflection from phase grating influences on both the amount of power transmitted to the observation plane and the pattern envelope. Figure 3.13 demonstrates the transmission with respect to grating thickness h . For a sinusoidal function $\sin(x)$, the reflection starts to happen

around points with $\max(\frac{d \sin x}{dx})$. The reflection area start to enlarge around these points. The first reflected beam may be reflected or transmitted from the front surface depending on the grating height. So, the transmission analysis becomes more complex for thick phase gratings. As seen in Fig.3.13, the transmission curve does not change linearly with respect to height h and has two deeps at around 18 and 22 μm . For the height of 18 and 22 μm , the first reflected beam from sinusoidal curvature is reflected back to the source from its front surface and for this reason, the transmission drops for these thicknesses.

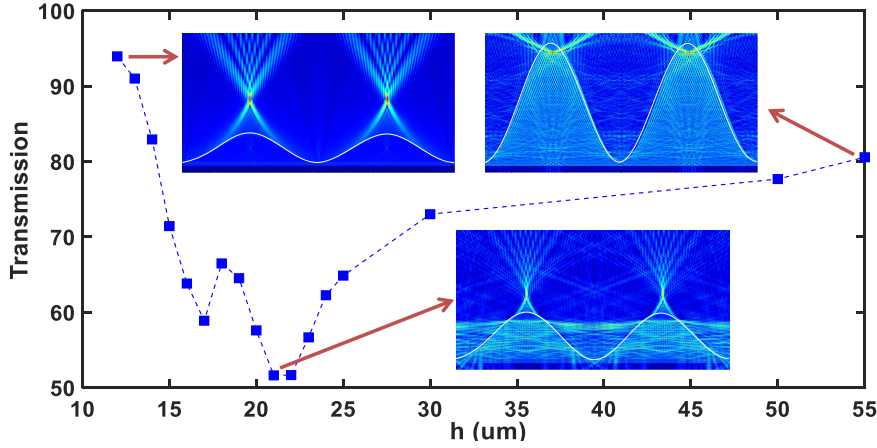


Figure 3.13: Transmission versus the grating thickness h .

Analysis of the problem using different approximations demonstrates that TEA is only valid for thin phase gratings and low Gaussian beam divergence angles. By increasing the phase grating thickness and source divergence angle, the problem becomes more complex to analyze. Especially, increasing the reflection influences on the near field distribution and far field pattern which necessitates using rigorous FDTD method.

3.4 Experimental Evaluation

3.4.1 Sample Fabrication using two photon absorption

The Nanoscribe Photonic Professional GT is a 3D printer that uses an infrared (780 nm) femtosecond laser to expose and polymerize UV-sensitive photoresists (IP-S, Nanoscribe GmbH, Germany)[7–9]. The laser is focused through an objective and the light intensity at the focal point is sufficient to initiate the two photon absorption and photo-polymerization. The two photon absorption is only triggered at the focus spot of the objective where the intensity is high enough to absorb two photons, simultaneously. In contrast, one photon absorption can occur along the light propagation in a bigger area and for this reason, a high resolution polymerization is not achieved for one photon absorption. Figure 3.14 shows the difference between the imaging fluoresce of two photon and one photon absorption.

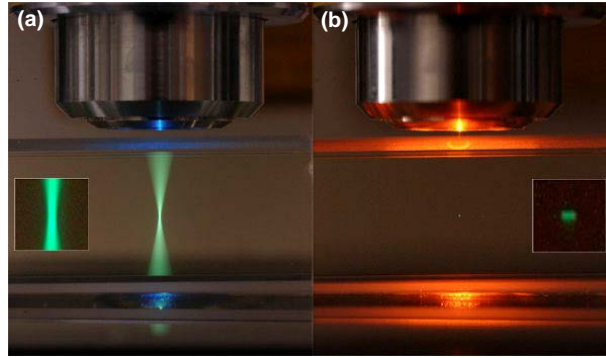


Figure 3.14: Imaging florescence of (a) One photon absorption in which the laser excites a large cone area of sample and (b) Two photon absorption in which the laser excites only a small area of sample.(courtesy of S. Ruzin and H. Aaron, UC Berkeley)

The smallest printable volume is called a voxel. The voxel dimensions determine the fabrication resolution and depend on the objective that we use for writing the structure. By moving the laser focus along our desirable trajectory in space, we can print 2D and 3D structures. Figure 3.15 shows the printing process for an arbitrary shape[10]. After developing the sample, the unpolymerized parts remove and our desirable structure remains on the substrate.

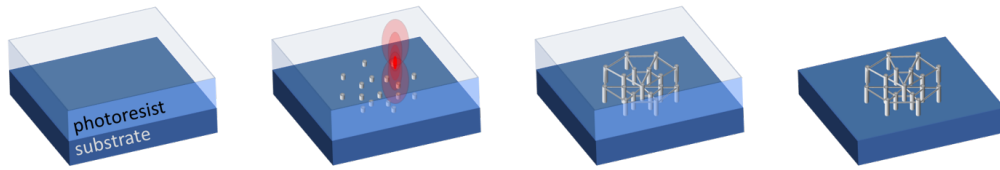


Figure 3.15: The printing process for an arbitrary shape using two photon absorption polymerization

The Nanoscribe machine that we use is shown in Figure 3.16(a). The machine is in communication with a software called Describe that converts our CAD generated structure in STL format to a language that is understandable for the machine to write the structure. We use the open-access Blender software to generate the CAD generated structure in STL format. The machine comes with different objectives with different magnifications, 20x (in the air), 10x (immersion), 25x (immersion), 63x (immersion) according to our desirable printing resolution and speed. Different objectives come with different types of photoresists and substrates in immersion mode. For our sinusoidal phase grating fabrication, we use the 25x (immersion) objective with an ITO coated glass substrate and IP-S photoresist for polymerization as shown in Figure 3.16(b).

Different parameters such as the laser power, laser scanning speed, and the exposure time of laser influence the fabrication quality. For example, if the laser power is too high for a voxel dimension, the material is over-exposed and bubbles are created in sample meaning that the

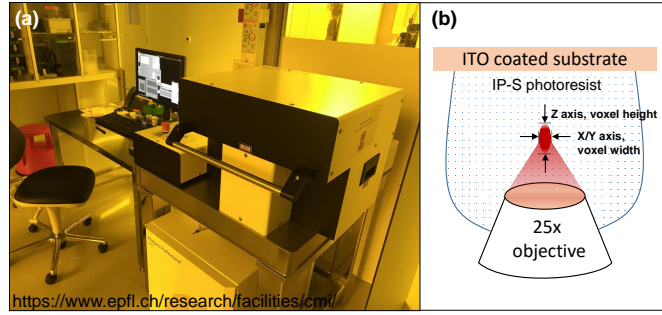


Figure 3.16: (a) A picture from the Nanoscribe machine that is used for fabrication and (b) A schematic of the objective, photoresist, substrate and voxel dimensions of focused beam. The voxel has an elliptic shape

sample temperature increases and the sample is destroyed. If the laser power is too low for a voxel dimension, the energy is not enough to initiate the photo-polymerization and the structure is not written. For optimization purpose, we fabricate several samples with different laser powers and voxel dimensions. Then, we choose the optimum parameters for the final sample fabrication.

We fabricated the sinusoidal phase grating for $h = 12$ and $25 \mu m$. The laser is focused through a 25x immersion objective and the light intensity is optimized to be sufficient at the focal point to initiate the photo-polymerization. The polymerization is done layer by layer by focusing the objective in different planes. The distance between planes is 100 nm and 200 nm for 12 and $25 \mu m$ thickness, respectively and the solid laser power intensity is optimized to be 40 in both cases. The piezo actuator moves the sample in the axial direction after fabricating each layer. For the lateral movement of the sample, the Galva actuator is used. As we explained earlier, the glass substrate is coated with ITO to obtain a refractive index contrast of more than 0.1 between IP-S and the substrate. After the writing process, the sample is developed in a bath of PGMEA for 10 min to remove the non-polymerized photoresists. Afterward, rinsing in the bath of Isopropanol for 2 min is done.

The photograph of one of the samples is shown in Fig. 3.17(a). Figure 3.17(b) demonstrates the scanning electron microscopy (SEM) of the sample. There are small gaps between the stitched areas [9]. It is due to the lateral movement of the sample during the exposure using the Galvano actuator which is not as accurate as piezo-actuators. Using the piezo is not practical as the writing time dramatically increases for the big lateral dimension of $0.5 \text{ mm} \times 1.2 \text{ mm}$ needed in the experiment. In Fig. 3.17(c), the zoom-in SEM image of the structure illustrates the surface roughness for this sample.

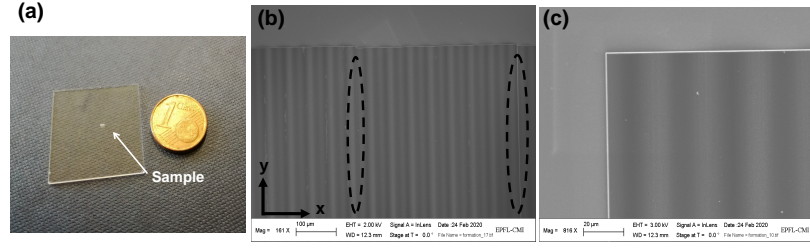


Figure 3.17: (a) Photograph from one of the fabricated samples. (b) Scanning electron microscopy (SEM) of the sample, showing a small gap between the stitched areas. (c) Zoom at a small area demonstrating the surface roughness.

3.4.2 Comparison of simulation and experiment

The schematic of the measurement setup is given in Fig. 3.18. A laser at 660 nm wavelength is coupled into an optical monomode fiber (P1-630Y-FC Thorlabs) with an NA between 0.1 and 0.14. Using the subsequent 1:1 aspheric pair lenses (Thorlabs, C110M-B, mounted match pair), the beam coming out of the fiber is imaged 8 mm away from the second lens flat front and a Gaussian beam source is created in very good approximation. In such a way, the setup is very versatile even for sample substrate of $700 \mu\text{m}$ thick and avoids small distance to phase gratings surface. Distance between Gaussian beam waist and grating surface D is chosen to be 3.8 mm , the same as the value for simulations. The pattern is projected on a screen 24 cm away from the sample and the image of the far-field distribution on the screen is captured by a camera (IDS CMOS camera) using an objective (JC10M Kowa lens series) with a big field of view of 80 degrees along the x -axis. The 24 cm distance between the sample and the screen is not in the far-field region under plane wave illumination but for the Gaussian beam, the far-field region is at smaller distances from the sample [11] and for this reason, we are able to observe the far-field already at 24 cm .

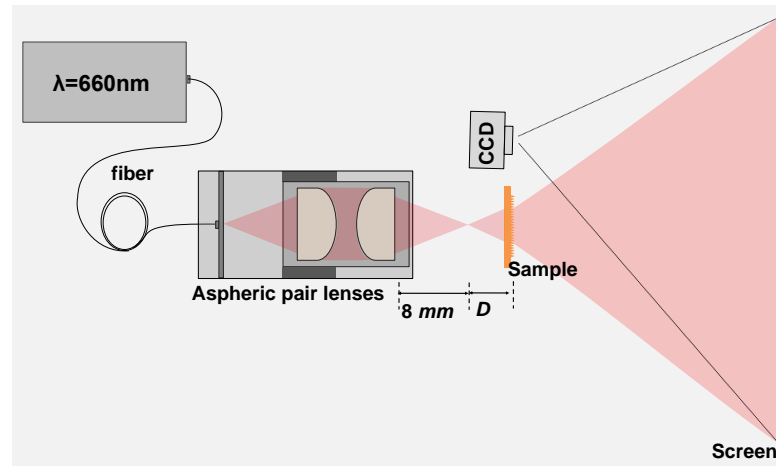


Figure 3.18: The schematic of the optical setup.

In Fig. 3.19 (a) and (b), the experimental far-field pattern is compared with the simulation result for $h = 12$ and $25 \mu m$, respectively. All the simulations are done using FDTD and high NA propagator. The measurements verify the simulation results especially the pattern distributions match very well for $25 \mu m$ thick sample. For $12 \mu m$ thick configuration, the experiment pattern envelope is not exactly the same as simulation although the number of peaks clearly matches with simulation. Also, the measurement verifies that more numbers of peaks are generated for $25 \mu m$ in comparison to $12 \mu m$ thick phase grating. The quality of the experimental result is limited by two constraints: First, the fabrication of high quality micro-optical periodic structures is challenging with a period of $50 \mu m$ and a big lateral dimension of $0.5 mm \times 1.2 mm$. As we discussed in the fabrication part, there are small gaps between the stitched areas which may influence the pattern quality although we have optimized the fabrication parameters for a high-quality sample. The second and most important limitation is the limited resolution (1280×1024) and dynamical range of the camera which lowers the contrast in measurements and the lines are not resolved with high quality in the picture.

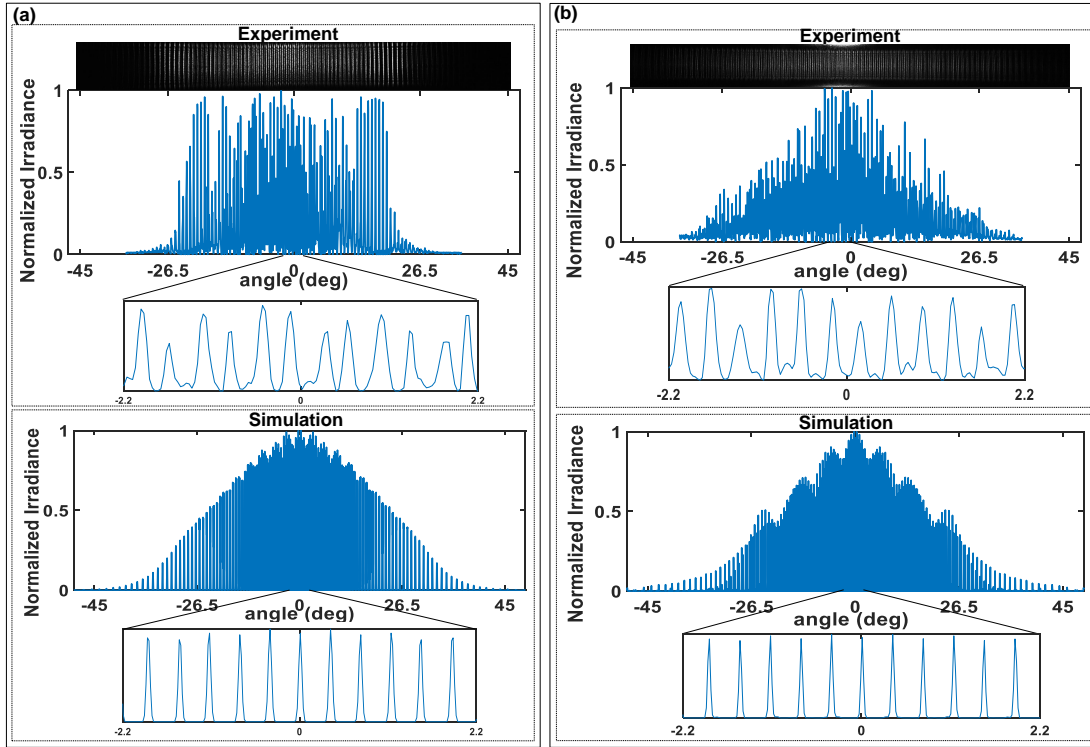


Figure 3.19: Experimental versus simulation far-field pattern for (a) $h = 12$ and (b) $25 \mu m$, respectively.

The measurements for 12 and $25 \mu m$ thick sinusoidal phase grating confirm the high accuracy simulation results. It demonstrates that choosing accurate near-field and far-field simulation tools is essential to find the correct pattern distribution. The accurate simulation tool is defined according to the phase grating thickness and surface curvature as well as the generated pattern

field of view in the far-field. Especially in the thick case of $25\mu m$, only the high precision FDTD simulation tool leads to the correct pattern distribution. To calculate the far-field for high diverging patterns in which the paraxial approximation is not valid, but the high NA propagator is enough accurate[12]. Also, the measurements confirm that $25\mu m$ thick phase grating generates the most number of points with uniform distribution as a dot pattern generator.

3.5 Far-field pattern contrast evaluation versus D

As we discussed, for particular values of the distance D between the source and the phase grating in Fig. 3.18, high contrast pattern in the far-field is achieved as a result of interference effects of the curved wavefront and the grating. In this part, we evaluate the contrast by changing D for $12\mu m$ thick sinusoidal phase grating by comparing the simulation and experiment. The phase grating near-field is calculated using the rigorous FDTD simulation tool. As we explained earlier, for a period of $50\mu m$ and the source wavelength of $650nm$, the high contrast peaks are observable for $D = 3.8mm$. We are most interested in the contrast variation by changing D around high contrast pattern distance. The contrast is defined by the following formula,

$$\text{contrast} = \frac{\text{pattern standard deviation}}{\text{pattern mean value}} \quad (3.10)$$

The 1D sinusoidal phase grating is fabricated using the introduced direct laser writing system (Photonic Professional GT, Nanoscribe machine). The sample dimensions are $0.5mm \times 1.2mm$. The scanning electron microscopy (SEM) images of the sample are shown in Fig. 3.20. As seen in Fig. 3.20(a), the dark vertical and horizontal lines show a gap between the stitched areas. Also, the resolution of sample fabrication is three times lower than the fabricated samples in the previous section, reducing the quality of the experimental results. Although, the recorded irradiance pattern quality is good enough for demonstrating the contrast variation versus the distance D .

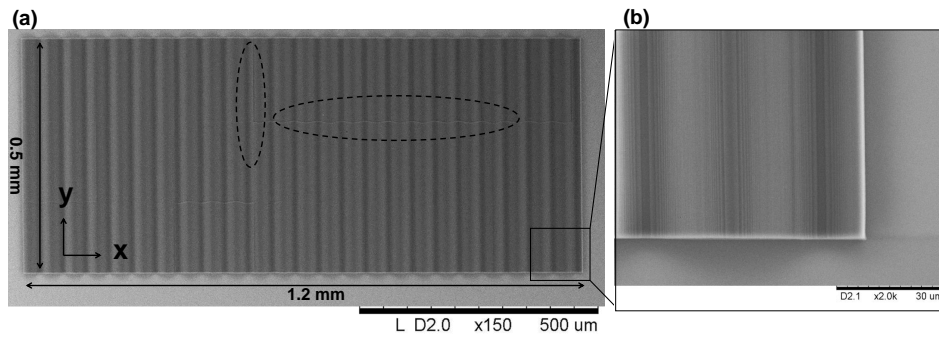


Figure 3.20: ((a) Scanning electron microscopy (SEM) of the sample, showing horizontal and vertical small gap between the stitched areas. (c) Zoom at a small area demonstrating the surface roughness.

The calculated contrast using simulation is shown in Fig. 3.21(a). There is one peak in the contrast curve, which is almost symmetric around $D = 3.8 \text{ mm}$. In the experiment evaluation, the far-field irradiance pattern is recorded by changing D around 3.8 mm and the contrast is calculated for each measurement. We plot the experimentally obtained pattern contrast versus D in Fig. 3.21. The simulated and experimental contrast curves match very well except that the contrast variation around its peak is higher using the rigorous simulation tool in comparison with experiments because the sample quality is not high. Figure 3.21(c) demonstrates the experimental far-field patterns for points A, B, and C which are determined in Fig. 3.21(b). As seen in the line plots, the pattern has a higher contrast in point B in comparison to points A and C. Also, the far-field patterns are horizontally divided into three sections. It is due to the space between stitched areas in the fabricated sample. Here, we experimentally and numerically demonstrated that the high-contrast pattern in the far-field is achieved for the particular distances of D in which the self-imaging condition is satisfied.

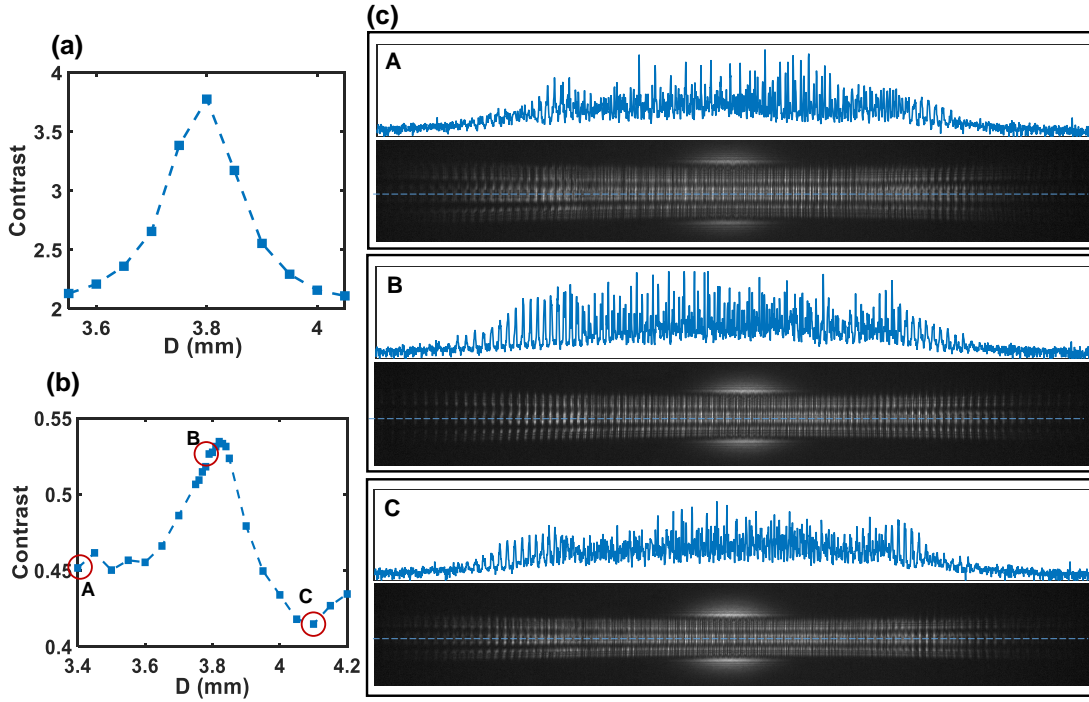


Figure 3.21: (a) Calculated contrast versus D using near-field FDTD simulations (b) Calculated contrast for experimental irradiance patterns versus D and (c) Experimental irradiance pattern for points A, B and C which correspond to $D = 3.4, 3.8$ and 4.1 mm , respectively.

3.6 Surface profile optimization

In this chapter, we demonstrated that for double curvatures in one period of a phase grating, we can double the number of points in the far-field compared with a regular lens array that would only contain a single radius of curvature as a parameter. In this part, we would like to optimize the curvature to achieve a high pattern uniformity in the far-field. The aspherical

surface profile of a conic lens (without considering the polynomial coefficient) is shown by

$$f(x) = \frac{cx^2}{1 + \sqrt{1 - (1+k)c^2x^2}} \quad (3.11)$$

Where $c = 1/R$ is the curvature (R Radius of curvature) and k is the conic constant of the lens. For $k = 0$, the surface is spherical and for $k = -1$, the lens surface is paraboloidal. To perform lens surface optimization for the double lens geometry, we consider the configuration in Fig. 3.22. A concave and a convex lens are illuminated by a plane wave. By taking the Fourier transform of two lenses near-field, the pattern envelope for periodic lens array under Gaussian beam is obtained. The figure of merit for optimization is defined by

$$u = \frac{\text{Pattern envelope standard deviation}}{\text{Pattern envelope mean}} \quad (3.12)$$

u is a criterion for evaluating the uniformity of pattern distribution. One more important parameter in practical applications is the amount of reflection (r) from the surface profile, demonstrating the amount of loss by passing through the lens. For this purpose, we evaluate the amount of reflection from the lens's surface profile. All the simulations inside the lens area have been performed using the FDTD method. We calculate u and r for $-1 \leq k \leq 0$ and $12.5 \mu m \leq R \leq 25 \mu m$ (for a 25×25 matrix). Performing 625 simulations is time-consuming for Gaussian beam illumination. For this reason, u and r are calculated for only one single period under plane wave illumination.

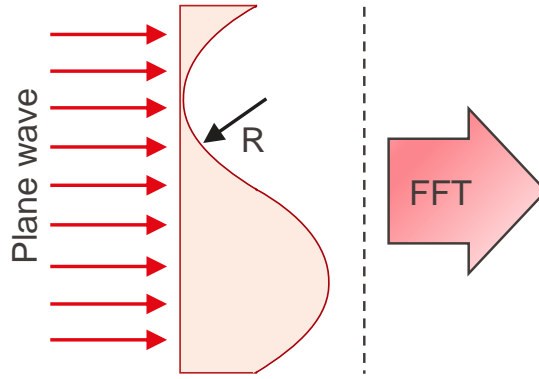


Figure 3.22: The configuration is a concave and convex lens under plane wave illumination. We study the effect of lens curvature on reflection (r) from lenses and pattern envelope which is the Fourier transform of the two lenses near-field.

As shown in Fig. 3.23(a), for the small conic constant k and radius of curvature R , a pattern with better uniformity and larger FOV is obtained. It means that the lens curvatures close to the paraboloid are a better choice in terms of pattern uniformity and FOV. On the other side, as seen in Fig. 3.23(b), the higher the lens curvature, the larger the amount of reflection from the surface. For spherical lens curvatures ($k = 0$), the effect of reflection is more pronounced

however, by going to paraboloidal shape ($k = -1$), the amount of reflection becomes negligible for most of the lens curvatures. Considering the colormap graphs in Fig. 3.23., our purpose is to choose a region in which the highest uniformity and the least amount of reflection are realized in the 2D plots. This area is determined with a dashed line square in Fig. 3.23(a); it means that the best point generators with respect to uniformity and reflection are obtained for $-1 \leq k \leq -0.7$ and $15 \mu m \leq R \leq 17.5 \mu m$.

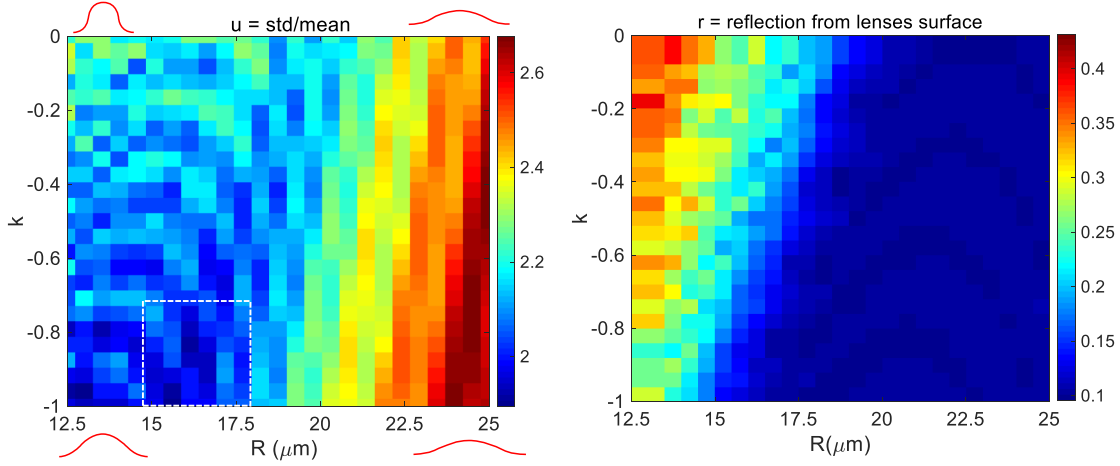


Figure 3.23: (a) u is calculated with respect to lens conic constant k and radius R . (b) Reflection from the surface is shown with respect to lens conic constant k and radius R .

Next, we compare the pattern distribution under Gaussian beam illumination for three curvatures, inside and outside the optimized area, as seen in Fig. 3.24. For $R = 12.5 \mu m$, a high FOV as large as $\pm 33.8^\circ$ is achieved however, the amount of reflection is higher in this case compared to the radius of 16 and $25 \mu m$. For $16 \mu m$ radius of curvature, a high FOV ($\pm 32^\circ$) and low reflection (11.3%) is achieved. Finally, for the radius of $25 \mu m$, a pattern with low FOV ($\pm 19.7^\circ$) is generated. In this case, the amount of reflection is negligible however, it is not a good point generator.

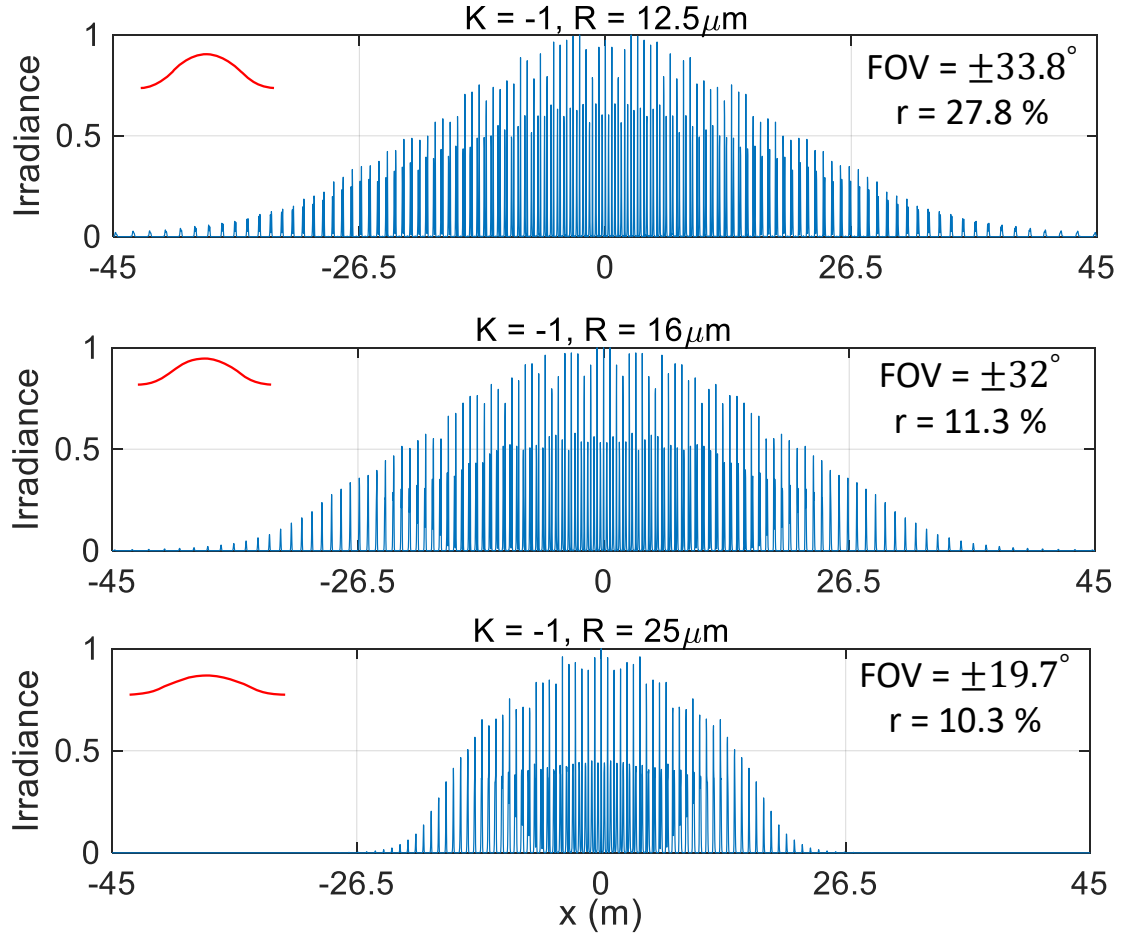


Figure 3.24: Far-field distribution under Gaussian beam for $k = -1$, and (a) $R = 12.5 \mu\text{m}$, (b) $R = 16 \mu\text{m}$, and (c) $R = 25 \mu\text{m}$.

Now, we briefly compare the optimized point generator ($K = -1$, $R = 16 \mu\text{m}$) that is shown in Fig. 3.24(b) with the point generators of sinusoidal curvature in the previous section. For the sinusoidal curvature, we obtained a pattern with $\pm 30^\circ$ FOV and reflection of 35.15% however with the optimized curvature, we can obtain a high FOV ($\pm 32^\circ$) and low reflection of 11.3%.

Next, we examine the pattern uniformity and reflection for inverted lens configuration. The configuration is shown in Fig. 3.25(a). As seen from Fig. 3.25(b), u is obtained to be small for high surface curvatures ($R = 12.5 \mu\text{m}$), especially for spherical geometries ($k = 0$). According to Fig. 3.25(c), the amount of reflection for all the curvatures is negligible (less than 11%). For this reason, there are no constraints concerning the reflection from curvature for such configuration. Figure 3.25(d) shows the field distribution for two of these geometries under the Gaussian beam illumination. As seen, the pattern FOV can be as large as $\pm 40^\circ$ for $k = 0$ and $R = 12.5 \mu\text{m}$. Also, for lens paraboloidal curvature ($k = -1$) and $R = 12.5 \mu\text{m}$ a pattern distribution with a very different envelope is generated. By further increasing this paraboloidal lens curvature ($R = 7.5 \mu\text{m}$), the FOV can reach $\pm 40.6^\circ$. Compared with the sinusoidal curvature in

the previous part, both the FOV and the number of points in the pattern are increased (FOV: $\pm 30^\circ$ to $\pm 40.6^\circ$; the number of points: 165 to 170). The simulations show that the inverted lens configuration is a better candidate in terms of the amount of reflection, pattern FOV, and the number of points in the pattern. A more comprehensive study can be done by applying the optimization algorithms and including non-zero polynomial coefficients to have more freedom for surface optimization.

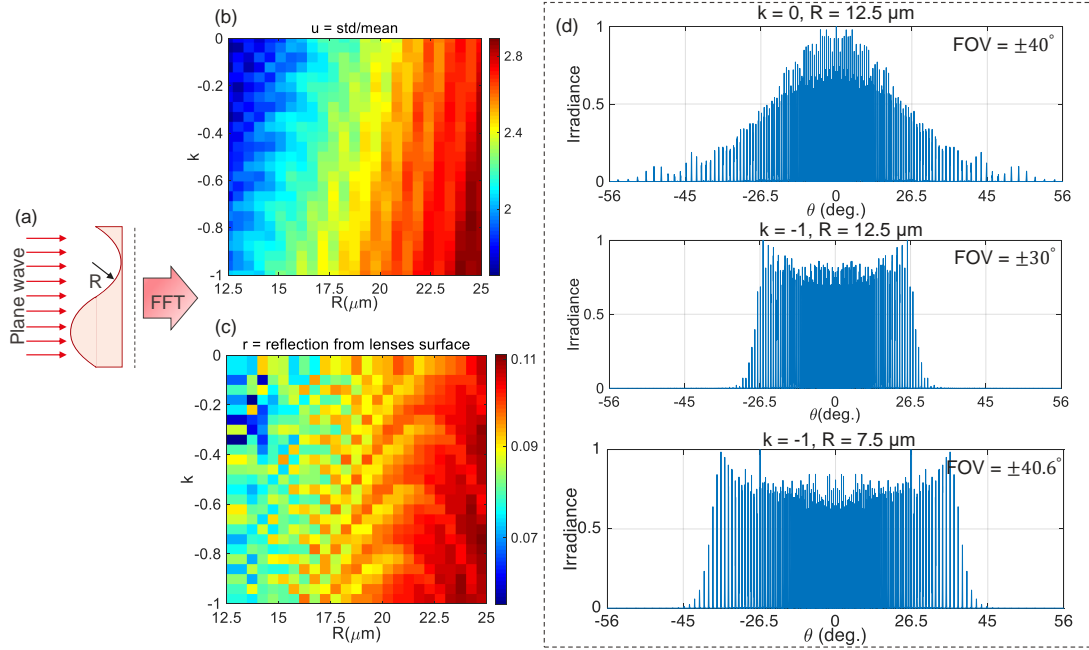


Figure 3.25: (a) Configuration is the inverted lens in which the incoming beam first hits the lens curvature. (b) u is calculated with respect to lens conic constant k and radius R . (c) Reflection from the surface is shown with respect to lens conic constant k and radius R . (d) Far-field distribution under Gaussian beam for $k = 0, R = 12.5 \mu\text{m}$, $k = -1, R = 12.5 \mu\text{m}$ and $k = -1, R = 7.5 \mu\text{m}$.

3.7 Summary

In this chapter, structured dot pattern generation under diverging Gaussian beam illumination for sinusoidal phase grating is investigated using the self-imaging phenomenon. Under the Gaussian beam illumination, large numbers of peaks with a wider field of view are generated in the far-field for sinusoidal curvature in comparison to the plane wave illumination. The influence of the source beam waist and the sinusoidal phase grating thickness on the far-field pattern is studied. We compared using TEA, FFT-BPM and the rigorous FDTD method for the near field simulations. TEA is not accurate for the simulation of shallow phase gratings for different source beam waists, especially in terms of far-field pattern envelope and field of view. According to the rigorous FDTD simulations, the reflection from sinusoidal phase grating increases by 4% for the smallest source beam waist in comparison with the plane wave

illumination due to the source wave-front curvature.

We studied the effect of changing the sinusoidal phase grating thickness on the far-field pattern using the FFT-BPM in comparison with the FDTD for near field simulation and Fraunhofer approximation compared with the high NA propagator for far-field simulation. The far-field intensity distribution is very sensitive to the phase grating thickness and completely different pattern distributions are obtained for different thicknesses. As a result of the FDTD simulations, we found that the total internal reflections inside the thick phase grating due to both the thickness and also the sinusoidal curvature of phase grating influence the near field distribution considerably. Consequently, using the scalar approach of FFT-BPM is not valid for thick sinusoidal phase gratings with more than 0.5 aspect ratio. Moreover, we demonstrated that the far-field Fraunhofer approximation cannot be used for thick sinusoidal phase gratings as the pattern field of view is large and using the high NA far-field propagator is obligatory. On the other hand, the comparison between thick and thin sinusoidal phase gratings demonstrates that very high structures with the unity aspect ratio generate non-uniform pattern distribution which is not suitable for point pattern generation. The 0.24 and 0.5 phase grating aspect ratios generate large numbers of peaks with uniform distribution which makes them suitable as point pattern generators. Finally, we demonstrated that the experimental results confirm the FDTD and high NA propagator simulations.

We experimentally and numerically showed that the high-contrast pattern for sinusoidal phase grating is achieved for particular distances between the source and the phase grating, in which the self-imaging condition is satisfied.

Finally, we optimized the surface profile of the phase grating to further improve the point generator in terms of pattern FOV and the number of generated points.

References

- [1] B. C. Kress. "Field guide to digital micro-optics". In SPIE, 2014.
- [2] S. Som and A. Satpathi. "The generalised lau effect". *Journal of Modern Optics*, 37(7):1215–1225, 1990.
- [3] J. Jahns and A. W. Lohmann. "The lau effect (a diffraction experiment with incoherent illumination)". *Optics communications*, 28(3):263–267, 1979.
- [4] N. I. Petrov and G. N. Petrova. "Diffraction of partially-coherent light beams by microlens arrays". *Optics express*, 25(19):22545–22564, 2017.
- [5] A. Naqavi, H. P. Herzig, and M. Rossi. "High-contrast self-imaging with ordered optical elements". *JOSA B*, 33(11):2374–2382, 2016.
- [6] U. Levy, C.-H. Tsai, H.-C. Kim, and Y. Fainman. "Design, fabrication and characterization of subwavelength computer-generated holograms for spot array generation". *Optics express*, 12(22):5345–5355, 2004.

- [7] B. H. Cumpston, S. P. Ananthavel, S. Barlow, D. L. Dyer, J. E. Ehrlich, L. L. Erskine, A. A. Heikal, S. M. Kuebler, I.-Y. S. Lee, D. McCord-Maughon, et al. “Two-photon polymerization initiators for three-dimensional optical data storage and microfabrication”. *Nature*, 398(6722):51–54, 1999.
- [8] T. Gissibl, S. Thiele, A. Herkommer, and H. Giessen. “Two-photon direct laser writing of ultracompact multi-lens objectives”. *Nature Photonics*, 10(8):554, 2016.
- [9] A. Radke, B. Fries, D. Eicke, F. Niesler, C. Baretzky, T. Bückmann, M. Wegener, and M. Thiel. “High-speed 3d direct laser writing of micro-optical elements”. In *CLEO: Applications and Technology*, ATu2N–4. Optical Society of America, 2013.
- [10] F. Klein, T. Striebel, J. Fischer, Z. Jiang, C. M. Franz, G. von Freymann, M. Wegener, and M. Bastmeyer. “Elastic fully three-dimensional microstructure scaffolds for cell force measurements”. *Advanced materials*, 22(8):868–871, 2010.
- [11] L. M. Sanchez-Brea, F. J. Torcal-Milla, and E. Bernabeu. “Talbot effect in metallic gratings under gaussian illumination”. *Optics communications*, 278(1):23–27, 2007.
- [12] Y. M. Engelberg and S. Ruschin. “Fast method for physical optics propagation of high-numerical-aperture beams”. *JOSA A*, 21(11):2135–2145, 2004.

4 Interferometry setup

Interference is the superposition of traveling beams in space. For two or more coherently illuminating beams, the resulting interference can be constructive or destructive depending on the phase difference between the traveling fields. Two beams are temporally coherent with each other if they travel with the same frequency, and a constant phase difference between them. If the beams are in phase, the interference is constructive meaning that the resulting wave amplitude increases; for out of phase traveling beams, the interference is destructive meaning that the two waves cancel out each other.

Consider two coherently traveling beams along the same direction with the same frequency and wavelength. Two-beam interference is the superposition of the fields; the resulting irradiance I , is described by [1],

$$I = A_1^2 + A_2^2 + 2A_1 A_2 \cos(\phi_1 - \phi_2) \quad (4.1)$$

Where A_1 , A_2 are the amplitude and ϕ_1 , ϕ_2 are the phase of the two traveling beams. In practice, detectors can only distinguish the intensity I which is proportional with the square of beam amplitude A^2 . Rewriting Eq. 4.1,

$$I = I_1 + I_2 + 2\sqrt{I_1}\sqrt{I_2} \cos(\phi_1 - \phi_2) \quad (4.2)$$

Where I_1 and I_2 are the irradiance of two superposing beams. The working principle of an interferometer setup is to extract the phase difference $\Delta\phi = \phi_1 - \phi_2$ by recording the irradiance of two superposing reference beams and object beam. As it is seen in Eq. 4.2, we extract the relative phase difference between the beams and not the pure phase of each incoming beam [2]. In summary, to observe the interference between the two beams, the first beam must be temporally and spatially coherent to the second beam. Also, the two beams must be compatible in terms of polarization properties. As an example, if the first beam is linearly polarized along x and the second beam is linearly polarized along y , the beams do not interfere [1].

4.1 Interferometer setup

The interferometer working principle is to split a beam into two arms, reference and object arm. The beams travel in two different paths and experience different phase delays. The beams are then recombined and the resulting interference pattern is recorded on the detector. For optical interferometry, two common configurations can be applied. As it is seen in Fig. 4.1(a), the Michelson interferometer is one of the setups that was first presented by Albert Abraham Michelson [3]. The beam is split into two arms using a beam splitter. The beam in each arm is then reflected from a mirror. The reflected beams are superposed in a beam splitter and collected on the detector.

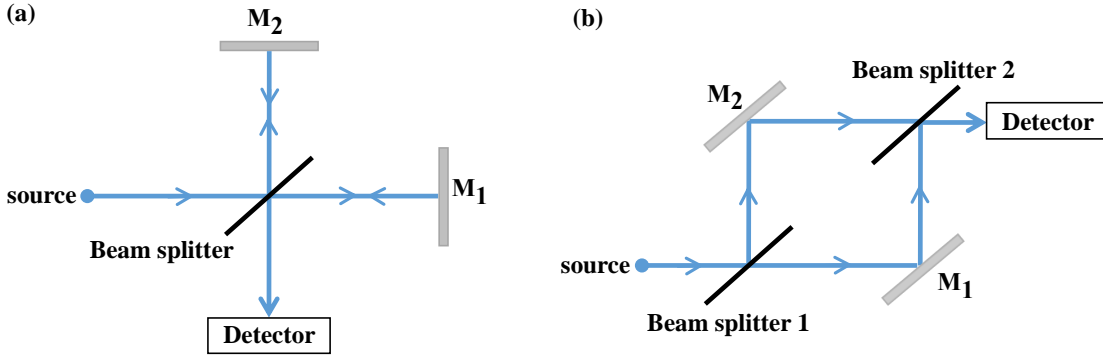


Figure 4.1: (a) Michelson interferometer, and (b) Mach-Zehnder interferometer.

In another configuration in Fig. 4.1(b), a Mach-Zehnder interferometer is adopted that was first proposed by Ludwig Zehnder in Ref. [4] and was refined by Ernst Mach in another work [5]. As seen, the beam is split into reference and object arms by applying the first beam splitter. In the reference arm, the wave properties are preserved; the beam is considered as a reference for extracting the phase difference. In the object arm, the beam can be modulated by introducing an optical element or changing the optical length. The reflected beams from the first and second mirrors are then collected by the second beam splitter and displayed on the detector. Finally, the generated phase difference by introducing a disturbance in the object arm is extracted from the interference pattern on the detector. In this thesis, we will adopt a high-resolution interference microscopy system that is based on a Mach-Zehnder interferometer to extract the phase disturbance as a result of introducing micro-optical elements in the object arm.

4.2 Phase-shifting interferometry technique

As we discussed, the phase difference is extracted based on the two-beam interference Eq. 4.2. Rewriting Eq. 4.2 in the following simplified form,

$$I = I' + I'' \cos[\phi(x, y) + \delta(t)] \quad (4.3)$$

Where $\phi(x, y)$ is the introduced unknown phase delay in the object arm and $\delta(t)$ is a known phase shift that we apply to solve the equation. As seen, Eq. 4.3 has three unknown variables of I' , I'' and $\phi(x, y)$, and at least three interference patterns should be recorded in the detector to solve the problem. To produce the phase shift $\delta(t)$, we apply a piezo-electric driven mirror in the reference or object arm to precisely change the optical path in the nanometer range. A common phase shift of $\delta(t)$ is $\pi/2$ that is equivalent to the optical path difference of $\lambda/4$. As an example, considering $\delta_1 = 0$, $\delta_2 = \pi/2$, $\delta_3 = \pi$, $\delta_4 = 3\pi/2$, and $\delta_5 = 2\pi$, the recorded intensities are as follows

$$\begin{aligned} I_1 &= I' + I'' \cos(\phi) \\ I_2 &= I' - I'' \sin(\phi) \\ I_3 &= I' - I'' \cos(\phi) \\ I_4 &= I' + I'' \sin(\phi) \\ I_5 &= I' + I'' \cos(\phi) \end{aligned} \tag{4.4}$$

Although three equations are enough to derive the phase profile, by increasing the number of equations, the resulting errors of the experimentally obtained phase shift are reduced. Extracting the phase by recording 5 images is called the Schwider-Hariharan or five-steps phase-shifting interferometry [6]. The extracted phase is calculated by the following equation,

$$\phi = \tan^{-1} \left[\frac{2(I_2 - I_4)}{2I_3 - I_5 - I_1} \right] \tag{4.5}$$

The error can be further reduced by increasing the number of recorded images. In the last section of this chapter, we will study the effect of increasing the number of recorded images on measurement error, in more detail. Here in this thesis, we apply the 8-steps algorithm to extract the phase and further reduce the errors in comparison with the five-steps phase-shifting algorithm, where the phase is extracted by

$$\phi = \tan^{-1} \left[\frac{\frac{1}{2}(I_4 + I_8) - \frac{1}{2}(I_2 + I_6)}{\frac{1}{2}(I_1 + I_5) - \frac{1}{2}(I_3 + I_7)} \right] \tag{4.6}$$

4.3 High-resolution interference microscopy

We employ high-resolution interference microscopy (HRIM) which is a special type of microscopy technique to be able to extract both the phase and intensity of electromagnetic fields. In the following, we first demonstrate the schematic of our HRIM setup under plane wave illumination and briefly explain the working mechanism. Then, we introduce the modified setup for different illumination conditions. Finally, we explicitly explain the optical components and their functionality in the setup.

4.3.1 High-resolution interferometry setup under plane wave

A schematic of the initial interferometry setup is shown in Fig. 4.2. Based on the two-beam interference phenomenon, a Mach-Zehnder interferometer is utilized to retrieve the phase profile. The beam is split into two arms using a fibered beam splitter. In the object arm, a Plane-wave illumination is generated by applying a collimating lens with a focal length of 4.6 mm (CFC-5X-A, Thorlabs), as it is seen in the inset Fig. 4.2. The collimated beam is collected using a microscope objective and reflected from a piezo-driven mirror. The reflected beam is then interfered with the collimated beam from the reference arm, in a second beam splitter, and displayed on the CCD camera. Before starting the actual measurements under a modified source, the objective position should be optimized for further measurements. To do so, we optimize the objective and tube lens position as well as the piezo-driven mirror tilting angle to observe a flat interference pattern having a single fringe on the CCD camera. The flat intensity distribution on the CCD camera assures that the plane wave illuminations in the object arm and the reference arm travel the same optical path length. The microscope objective and the tube lens positions are now fixed and the setup is ready for replacing the plane wave with a focused beam source and inserting microoptical elements in the object arm for real measurements.

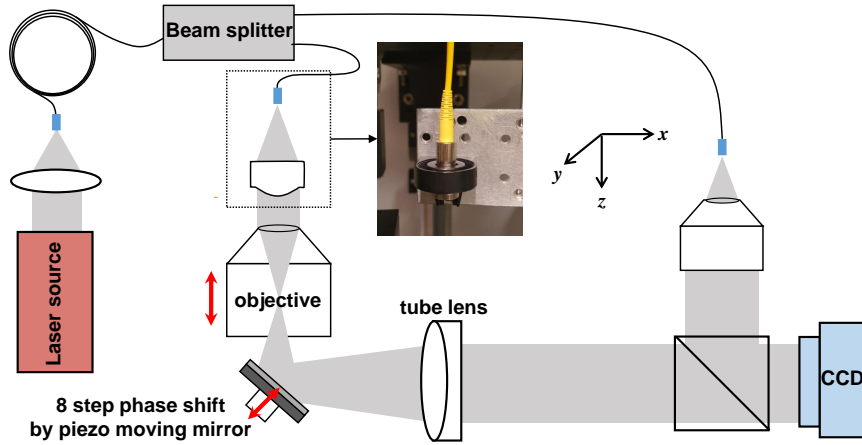


Figure 4.2: Setup schematics for adjusting the objective, tube lens position, and tilt of the mirror.

In the object arm in Fig. 4.2, the fiber NA is between 0.1 and 0.12. The collimated beam by applying the lens has a diameter of 1 mm for a lens focal length of 4.6 mm . The beam diameter of 1 mm is collected by 50x or 20x magnification objectives. The captured field diameter on the CCD camera by the objectives is 0.14 mm and 0.4 mm for 50x and 20x magnifications, respectively. It demonstrates that the collimated beam is efficiently collected by the objectives.

4.3.2 High-resolution interferometry setup under focused beam

The standard configuration for setup calibration is under plane wave illumination, as it was shown in Fig. 4.2. To apply this standard interferometry setup for our problem in which the source is a focused beam instead of a plane wave, we consider two configurations as shown in Fig. 4.3 (a) to modify the source in the object arm. The first configuration is an MLA under a focused Gaussian beam at a certain distance D . The second geometry is an MLA under a focused Gaussian beam in which the source near-field is modulated by applying a microstructure for instance a microsphere. The schematic of the modified setup is shown in Fig. 4.3 (b) for these configurations. The setup works in the transmission mode and the fields propagate in free-space.

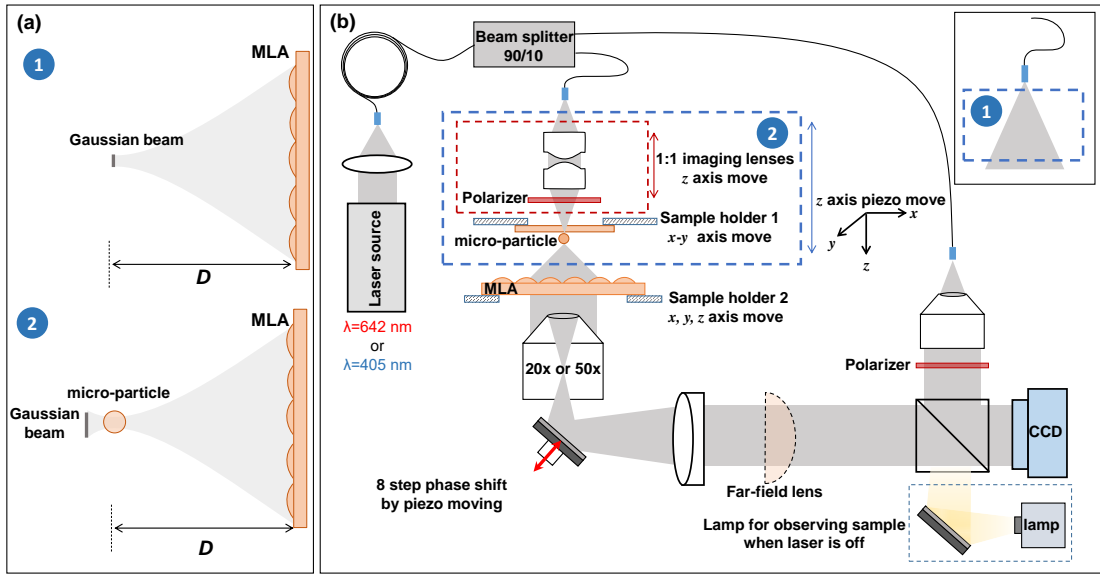


Figure 4.3: (a) The schematic of configurations for different source illumination conditions and (b) The corresponding schematic of high-resolution interference microscopy setup (HRIM) which is based on a Mach-Zehnder interferometer.

As it is seen in Fig. 4.3 (b) for configuration number 2, a single-mode linearly polarized laser diode is utilized as the source. A beam splitter divides the intensity into the reference and object arm. In the object arm, the beam out of the fiber is imaged using an aspheric pair lenses. This imaged focused beam corresponds to the focused Gaussian beam in configuration 1 and 2 in Fig. 4.3 (a). The aspheric pair lenses can freely move together along z axis to precisely focus the beam on the micro-particle which is attached to the sample holder 1. Sample holder 1 can freely move along x and y axis to precisely focus the beam at the center of the micro-particle. The aspheric pair lenses and the sample holder 1 are mounted on a precision piezo stage to translate along the z axis. This allows us to record the micro-particle near-field amplitude and phase distribution with high precision by moving the sample and illumination part together along the z axis. Sample holder 2 retains the MLA and can freely move along x , y , and z axis.

The beam is then collected by the objective. The MLA and the objective are mounted on a translation stage to freely move along x , y , and z axis, especially for adjusting D which is the distance between the MLA and the micro-particle. The incoming beams from the reference arm and object arm are collected on the CCD camera. By moving the piezo-electrically driven mirror, an optical path length shift is generated in the object arm. Eight interference patterns are recorded by adding an optical path length of $\lambda/4$ and the phase profile is extracted by employing the 8-step phase-shifting interferometry technique.

To apply the geometry number 1 (shown in Fig. 4.3 (a)) in setup, the components that are determined in the dashed line box 2, will be replaced by the configuration in dashed line box 1 in the inset Fig. 4.3 (b) which is a fiber exit. The fiber output is used to model the focused Gaussian beam. The tested micro-optical elements include MLAs with a period of 30 and 50 μm ; the microspheres and spheroids to modify the source near-field are in the range of 10 to 20 μm diameter.

4.3.3 Setup optical components and their functionality

In this section, we illustrate the used optical components in our setup, with more details. An image of our high-resolution microscopy optical setup is shown in Fig. 4.4.

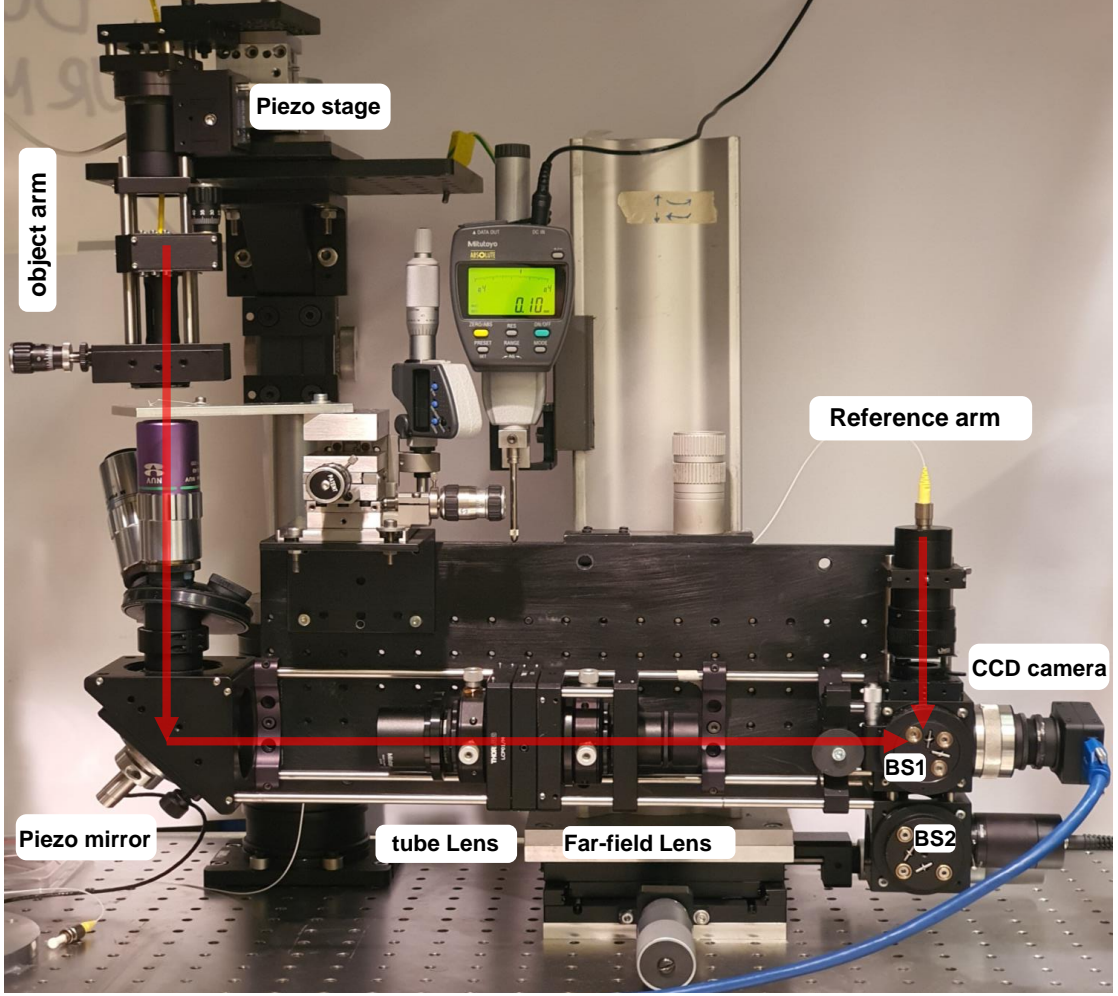


Figure 4.4: High-resolution interference microscopy optical setup.

Optical source

Here, we start by explaining the laser source specifications. The light sources are two single-mode polarized laser diodes with different powers and wavelengths (CrystaLaser, 642 nm: DL640-050-3, 405 nm: BCL-040-405-S), to investigate the structured light generation for different wavelengths. The beam diameter of laser sources is approximately 1 mm ($1/e^2$ intensity). As it is seen in Fig. 4.5 (a), the beam out of the laser source is coupled into a fiber by making use of a focusing lens. The incoming beam out of the fiber is split into two arms by applying a beam splitter (TW630R2F2, Thorlabs) with the 90/10 aspect ratio, as it is shown in Fig. 4.5 (b). The 90% of power is transmitted to the object arm to compensate for the losses because of the field propagation through the optical components including lenses and also the samples. To observe high contrast fringes on the detector due to the interference between the object arm and reference arm beams, we have to more precisely equalize the beam intensities in the two arms. For this purpose, we apply Neutral density filters with different transmission

efficiencies, as is seen in Fig. 4.5 (c). Depending on the number of samples in the object arm, we apply those filters in the reference arm or/and object arm.

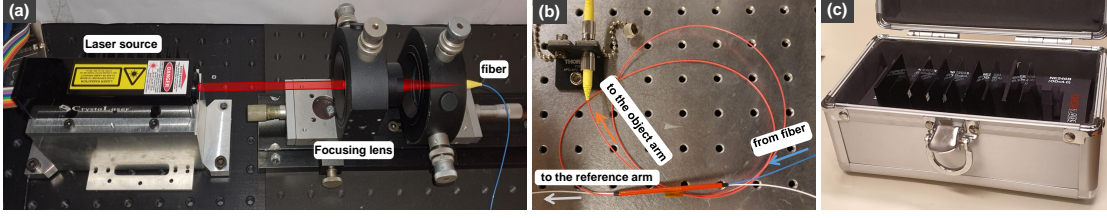


Figure 4.5: (a) Laser source output is coupled into the fiber by using a focusing lens and (b) the beam out of the fiber is split into the object arm and the reference arm. (c) Neutral density filters with different transmission efficiencies to adjust the intensity in reference or object arm.

Illumination part in the object arm

Here, we focus on the illumination part number 2 in Fig. 4.3 (b) in which the focused source near-field is modulated by a micro-particle. In Fig. 4.6, the schematic of the illumination part as well as the corresponding used optical components are shown. As seen in Fig. 4.6 (b), the actual setup includes the piezo stage along z , translation stage along z , aspheric pair lenses, and translation stage along x and y . Figures 4.6 (c) to 4.6 (f) more specifically show each of the optical parts in Fig. 4.6 (b). The optical cage and the translation stages are mounted on a precision piezo stage with a z scan range of $100\ \mu m$ (MadCityLabs, Nano-F100S), as seen in Fig. 4.6 (c). This allows us to record the micro-particle near-field amplitude and phase distribution with high precision by moving the sample and illumination part together along the z axis. By applying the z -axis translation mount (SM1Z, Thorlabs) in Fig. 4.6 (d), the tube lens containing the aspheric lens pair (C220MP-B, Thorlabs), and the polarizer can freely move together along z axis to precisely focus the beam on the micro-particle. The z -axis translation mount travel range is $2\ mm$ with $1\ \mu m$ increment which is sufficiently accurate in our application. According to Fig. 4.6 (e), we use a $1/2$ inch tube lens whose diameter is small enough to freely move in our $30\ mm$ cage system. As seen in Fig. 4.6 (f), the sample is attached under the $x - y$ translation mount (which is called sample holder 1 in schematics). The $x - y$ translation mount (ST1XY-D/M XY, Thorlabs) translates with differential drivers in a $+/- 3\ mm$ travel range and $0.5\ \mu m$ increment step. With the increment step of $0.5\ \mu m$, precisely focusing the beam to the center of a micro-particle with a diameter of around $10\ \mu m$, is challenging to do in comparison with using a piezo-driven stage. On the other side, for our two-level configuration in which the distance between the micro-particle and MLA is in the range of 2 to $3\ mm$, the differential translation mount has the advantage of being compact and having enough space to position the MLA very close to the micro-particle.

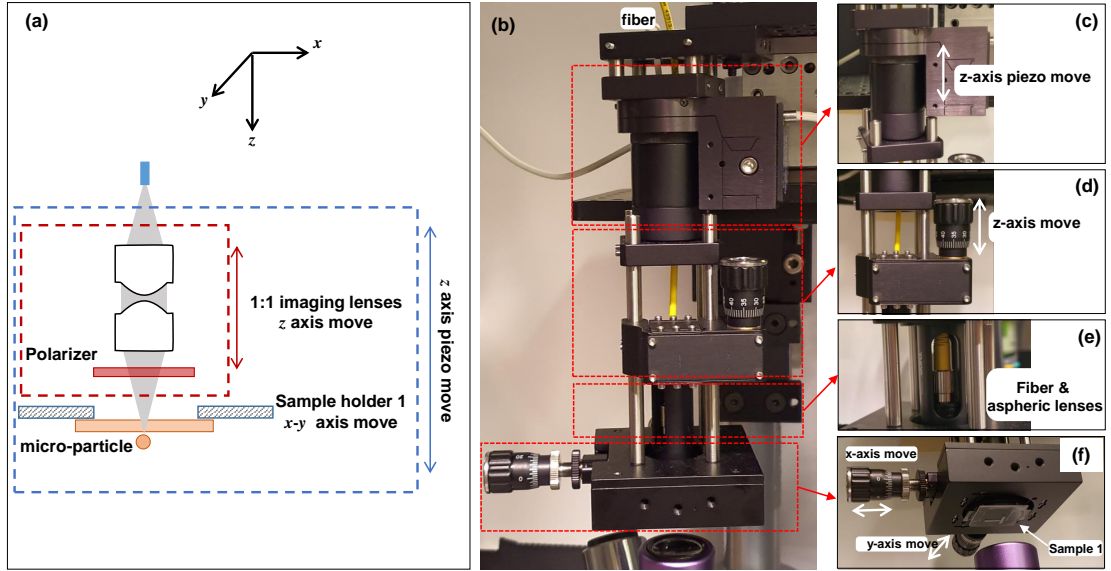


Figure 4.6: (a) The schematic of the illumination part in the object arm for an MLA under a focused Gaussian beam which is modulated by a micro-particle (b) The actual illumination part. (c) to (f) separate pictures of optical components that are shown in (b).

For configuration number 1 in Fig. 4.3 (b) in which there is no micro-particle, the illumination part is simply replaced by a fiber exit, or sample 1 moves along the x and y axis to focus the beam on the glass substrate parts where there is no structure. Although both configurations give similar results, in the latter case, the Gaussian beam propagates in a glass substrate of $700\ \mu\text{m}$ thick before passing through the MLA.

Objective and MLA parts in the object arm

Sample holder 2 in Fig. 4.3 (b) retains the MLA and can freely move along x , y and z axis. An image of the actual setup is shown in Fig. 4.7 (a). The stage is equipped with a digital micrometer along z axis with $1\ \mu\text{m}$ travel increment to precisely adjust the MLA position with respect to the micro-particle and the objective. The objective is adjusted to focus the beam on the sample and collect the information on the CCD camera. Two types of objectives (Mitutoyo APO 50x /NA 0.42 or APO 20x /NA 0.4) are used for recording the fields. A turret carries the two objectives to more conveniently switch between the two magnifications, as is shown in Fig. 4.7 (b).

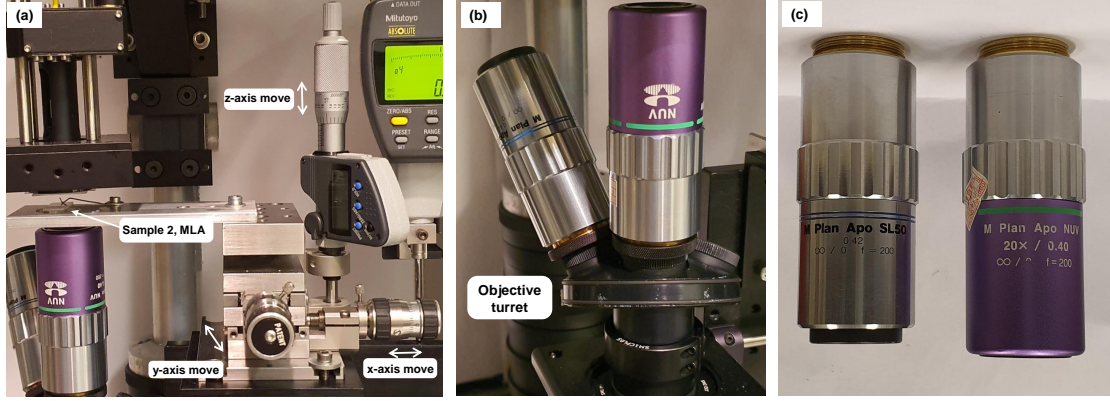


Figure 4.7: (a) Sample holder 2 which retains the MLA and is equipped with a translation stage to freely move the MLA along the x , y , and z axis. (b) The objective turret that holds the objectives and (c) The used objectives, 50x for micro-particle near field, and 20x for MLA near-field recording.

A picture from the two objectives is also shown in Fig. 4.7 (c). Using the 50x objective for collecting light in the near-field of the micro-particle, the lateral resolution is limited according to the objective numerical aperture ($NA = 0.42$) and is described by the Abbe diffraction spot size limit $\Delta x = \lambda / (2NA) = 764 \text{ nm}$ in the air for $\lambda = 642 \text{ nm}$. On the CCD camera (CM3-U3-50S5M-CS) with 2048 x 2448 number of pixels and pixel size of $3.45 \times 3.45 \mu\text{m}$, each pixel size corresponds to 69 nm in the object plane which is smaller than the resolution limit. We employ the 20x objective to collect the MLA near-field; using this objective the field can be recorded in a large area of $422 \mu\text{m} \times 353 \mu\text{m}$ that covers enough numbers of lenses in our setup. The 20x objective lateral resolution is 802 nm (for $\lambda = 642 \text{ nm}$, $NA = 0.4$).

Piezo mirror and tube lens in object arm

The incoming beam from the objective is reflected by a mirror and then imaged by a tube lens on the CCD camera, as shown in Fig. 4.8 (a). Moving the mirror with a precision piezo actuator and changing the optical path length in the object arm, eight interference patterns will be recorded to extract the phase by applying an 8-step phase retrieval algorithm.

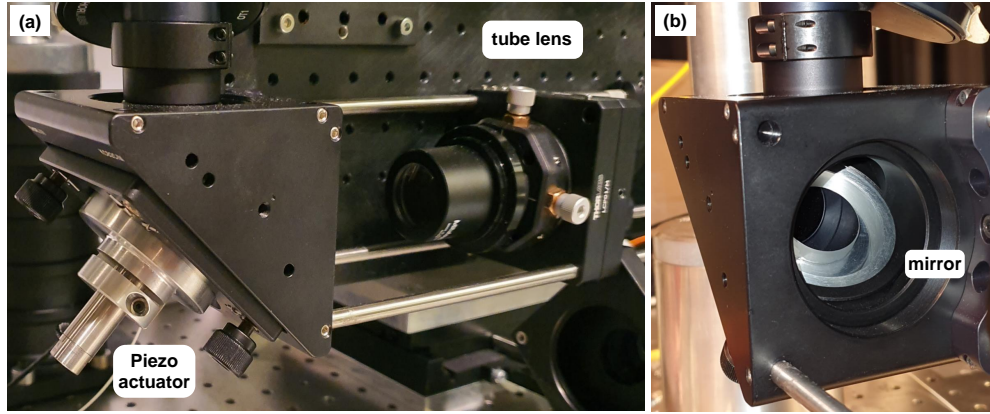


Figure 4.8: (a) The tube lens and the piezo-driven mirror which is mounted in the object arm to precisely change the optical path length for extracting the phase, (b) the front view of the mirror.

Reference arm

As seen in Fig. 4.9 (a), in the reference arm, the incoming beam out of the fiber is collimated by a lens and then is linearly polarized along the x axis by applying a polarizer. According to Fig. 4.9 (b), the beam from the reference arm and the object arm interfere in beam splitter 1 (BS_1) and the field distribution is displayed on the CCD camera. The setup is equipped with a lamp and a second beam splitter (BS_2) to observe the sample when the laser source is off.

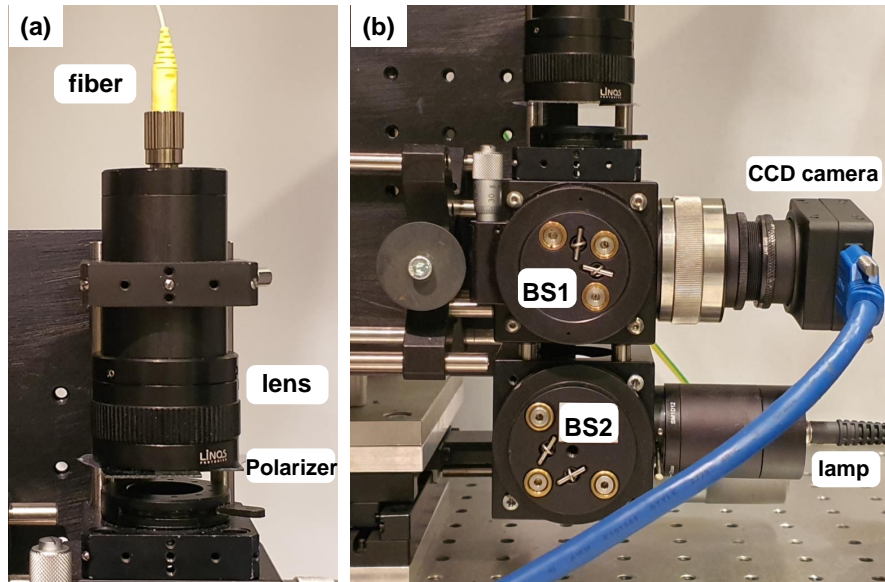


Figure 4.9: (a) The beam in the reference arm is collimated by a lens and linearly polarized by the polarizer, (b) the beam from reference and object arm interfere in beam splitter 1 (BS_1), and the interference pattern is displayed on the CCD camera. The lamp is for observing the sample if the laser is off.

Setup translation along x , y , and z

According to Fig. 4.10, the object arm components including the sample holder 2, objective, piezo-driven mirror, tube and far-field lenses as well as the reference arm can freely move along x , y , and z using a translation stage. Along the z -axis, the setup is equipped with a digital micrometer gauge of $10\text{ }\mu\text{m}$ interval increment. The ten-micrometer interval increment is enough accurate to adjust D which is the distance between the focused source and the MLA. The moving parts are determined in a dashed line area in Fig. 4.10.

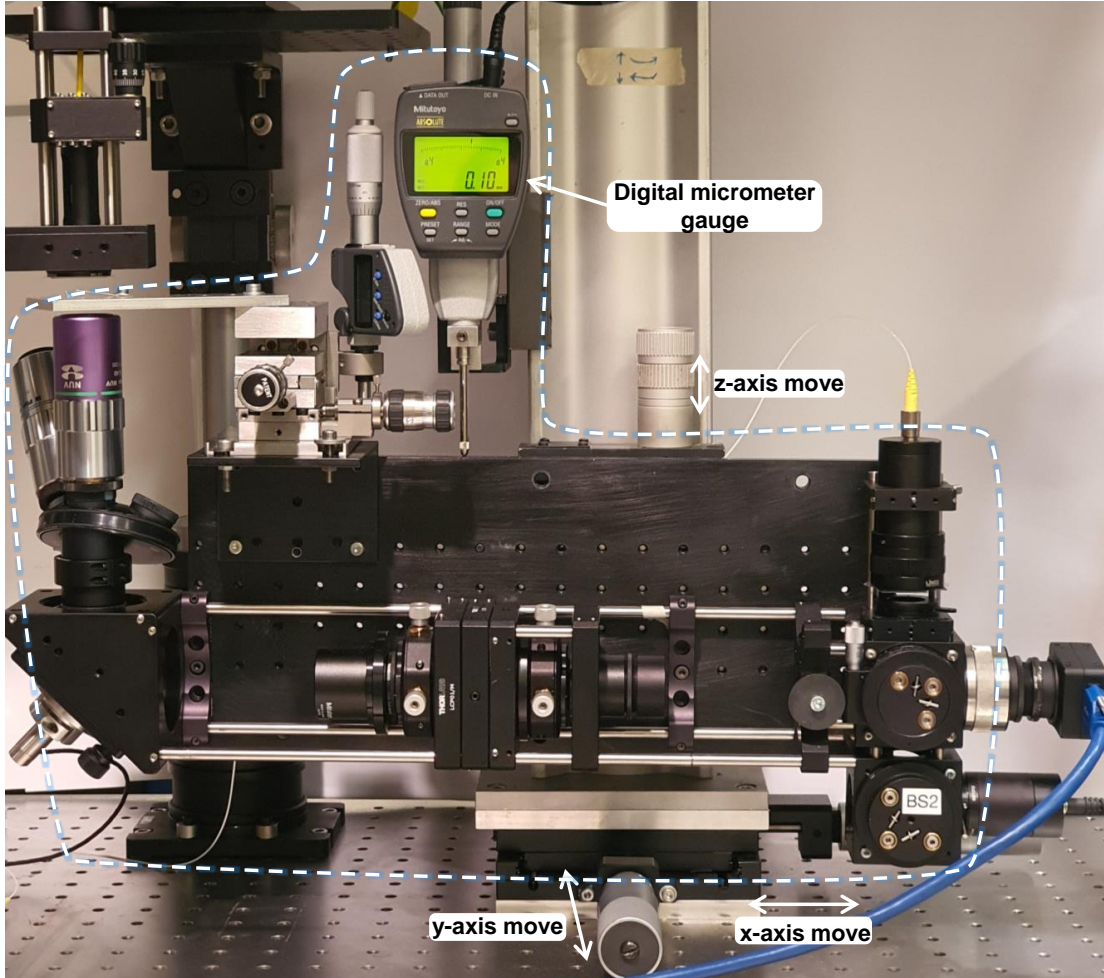


Figure 4.10: The moving parts of the setup by applying the translation stage are determined in a dashed line area. With the digital micrometer gauge along z axis, we precisely adjust the distance between the MLA and the focused source.

Recording far-field distribution

To record the far-field intensity distribution, we first block the reference arm, and then we apply a lens at its focal distance of 200 mm from the CCD camera, as it is shown in Fig. 4.11.

For a CCD camera at a lens focal distance, the field distribution is the Fourier transform of the incoming beam which is mathematically equivalent with the Fraunhofer approximation [7].

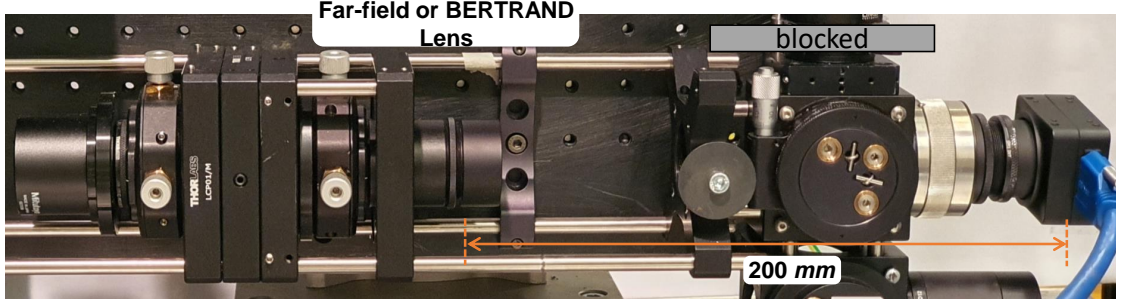


Figure 4.11: Recording far-field distribution. The incoming beam from the reference arm is blocked and then the far-field lens is inserted in the setup at its focal distance from the CCD camera.

Data extraction steps

To summarize our interferometry measurement steps, we review our two configurations that have been introduced in this chapter. The geometries are shown in Fig. 4.12.

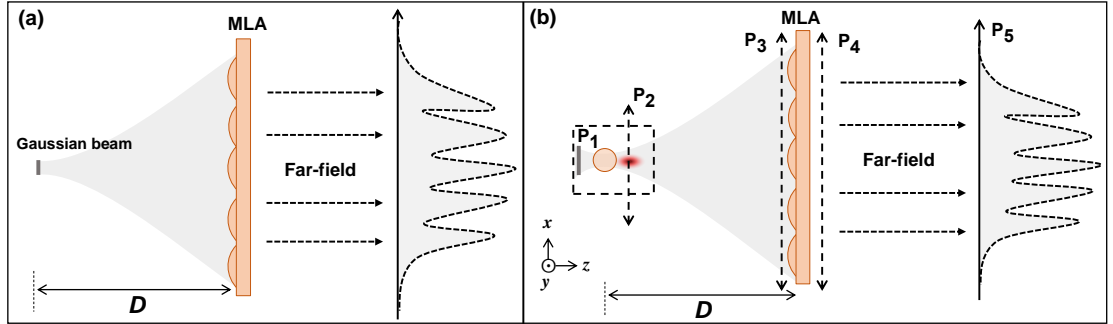


Figure 4.12: Two configurations are studied using the interferometry setup. (a) MLA under a focused Gaussian beam and, (b) MLA under a focused Gaussian beam which is modulated by a micro-particle.

In the first configuration in Fig. 4.12 (a), the MLA is illuminated by a focused Gaussian beam, and the field distributions are compared for different values of distance D . The measurement steps for this configuration are as follows:

1. The objective is focused on the MLA surface and the MLA near-field is recorded.
2. To measure the far-field distribution, the reference arm is blocked and the far-field lens is put into place to record the intensity distribution on the CCD camera.

In the second geometry in Fig. 4.12, the MLA is illuminated by a focused beam in which the focused source near-field is modulated by a micro-particle. For this geometry, we record the fields in the planes P_1 to P_5 in Fig. 4.12 (b). The measurement procedures are as follows:

1. Micro-particle near-field planes of P_1 (x - z plane) and P_2 (x - y plane): Remove MLA from setup. Focus the 50x objective on the micro-particle. Record phase and intensity in the near-field planes of the micro-particle.
2. Plane of P_3 immediately before MLA: Put into place the MLA. Adjust the distance between the MLA and micro-particle to be our designed value of D . Focus the 20x objective on the MLA surface. Remove the MLA and record the phase or amplitude distributions.
3. Plane of P_4 immediately after MLA: Again, put into place the MLA. Record the phase and intensity which is collected by the 20x objective.
4. The far-field intensity in the plane of P_5 : Block the reference arm. Put into place the far-field lens at its focal distance from the CCD camera to record the far-field pattern while the 20x objective is focused on the MLA surface.

In chapter 5, chapter 7 and chapter 8, we will present the measured fields for both configurations in Fig. 4.12 and compare them with simulation results.

4.4 Sources of error

Different errors contribute to the phase measurement by applying the phase-shifting interferometers PSI. Many of the errors can be reduced by applying some particular algorithms, however, there exist fundamental errors that influence the accuracy. These errors are classified into three groups; errors originating from the data acquisition process; environmental errors and errors that come from the optical setup deflection. The explicit study of these errors and the contribution of different types of phase-shifting algorithms are presented in Ref. [1, 8]. Based on this reference, here, we briefly discuss these errors and strategies to diminish them.

4.4.1 Phase shift error

The error resulting from phase shift influence the data acquisition process using the PSI algorithm. Ideally, the intensity in each point by linearly changing the phase is purely sinusoidal. However, in practice, the phase shift increment is not the predicted ideal phase shift. Therefore, we have to choose the algorithm that is less sensitive with respect to phase shift errors. In general, by acquiring more images, the algorithm can extract the phase with less error because of a higher sampling [9, 10].

4.4.2 Detector nonlinearity

Detector nonlinearity introduces an error which is especially important for very high contrast fringes. In Ref. [11], it is shown that by applying the four-step algorithm ($\alpha = \pi/2$), there is no error in phase measurement for linear and second-order detector nonlinearity however this cannot be said for the three-step algorithm. By further increasing the number of steps in PSI algorithm, the effect of high order nonlinearities decreases. However, these errors, in general, do not affect.

4.4.3 Source stability

Stability of source frequency and amplitude is a critical parameter. The frequency instability of the laser source, give rise to the instability of fringes that directly reduces the phase measurement accuracy. Considering a path length difference of ΔL , the frequency stability of the source satisfies the following inequality

$$\Delta\nu = \frac{c \cdot k}{\Delta L} \quad (4.7)$$

Where c is the light velocity and $k = 2\pi/\lambda$. This shows that the source instability is more problematic for large optical path differences. For example for a path difference of 2 m , $\Delta\lambda < \pi/\lambda$. For the source wavelength of 642 nm in our case, $\Delta\lambda < 2\mu\text{m}$ should be satisfied. Our laser source wavelength is $642\text{ nm} \pm 4\text{ nm}$, meaning that the source is stable enough with respect to frequency.

Instability in source intensity can be degraded by averaging if the intensity variation is random. For this reason, the resulting error depends on the used algorithm. For example, it is shown that for N -step least square algorithm, the standard deviation of the extracted phase is proportional with $1/\sqrt{N}$ [12]. In our experimental setup, we apply an 8 step PSI algorithm instead of regular 5 steps to reduce the effect of noise in the extracted phase.

4.4.4 Quantization error

To apply the PSI algorithm which is based on digital computing, we first require to convert the analog intensity signals to digital. There can be quantization errors in this step. However, nowadays computers and cameras, there is no issue with this subject.

4.4.5 Vibration error

Vibrations and mechanical instability in the optical setup can impose the error on the extracted phase. Normally, one uses mechanical tools such as vibration isolation mounts, vibration isolation table for mounting the whole setup, and also, stably building the optical setup. Location of optical setup is also important and it should be in a quiet place. Small vibrations can

be shown by perturbations in phase shift increment. Considering high-frequency vibrations, the effect of vibration induced by intensity fluctuations depends on the used PSI algorithm. The extracted phase standard deviation is roughly proportional to $1/\sqrt{N}$ [13] where N is the number of recorded images. It means that for more number steps, less error is induced due to small setup vibrations.

Several methods can be applied to reduce the effect of vibration when using PSI algorithms. A system can be applied in which all frames are taken simultaneously. One of these methods is based on using the Twyman-Green interferometer in combination with a holographic optical element (HOE), as seen in Fig. 4.13. Four identical copies of the beam are generated by applying the HOE. The beams are then collected by a CCD camera that is equipped with four different phase masks and polarizers to generate four different interferograms. In this strategy, all the interferograms are captured simultaneously and this way, the system is not sensitive with respect to vibrations. However, to record four images simultaneously, one requires a camera with a large number of pixels.

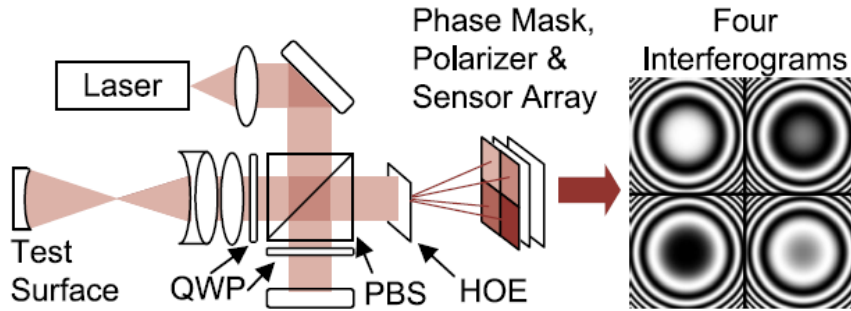


Figure 4.13: HOE based Twyman-Green interferometer setup to extract all frames simultaneously [1].

In our work, we develop our setup on the vibration isolated table to avoid vibration errors. Also, we apply an 8 step instead of a regular 5-step PSI algorithm to decrease the effect of errors resulting from optical setup vibrations.

4.4.6 Air currents and turbulence

Air currents and turbulence are also a source of errors in measurements. Fibered optics can be used to reduce this effect.

4.4.7 Coherent noises

The reflected beam from one surface within the coherence length can interfere with another incoming beam and generate measurement errors. These kinds of measurement errors, in some cases, can be eliminated. In Ref. [14], it has been shown that the three-step algorithm is

much more sensitive to reflections than the four-step algorithm. There exist other kinds of coherent noises; for example, dust and scratches on optical surfaces, inhomogeneities, etc., can generate measurement errors.

In summary, increasing the number of recorded frames in the PSI algorithm can reduce many of the errors and make the system very robust. The increased measurement time is not important for investigations in the laboratory. Here we compare the three, five, and eight steps PSI algorithms for extracting the phase, considering no filtering in the extracted phase. As seen in Fig. 4.14, the extracted phase for the three steps is very noisy. For five and eight steps, the images are much less noisy because of the averaging over more frames; however, the phase modulation is not the same for five and eight steps. In our experiments, we apply the 8-step PSI algorithm to extract the phase.

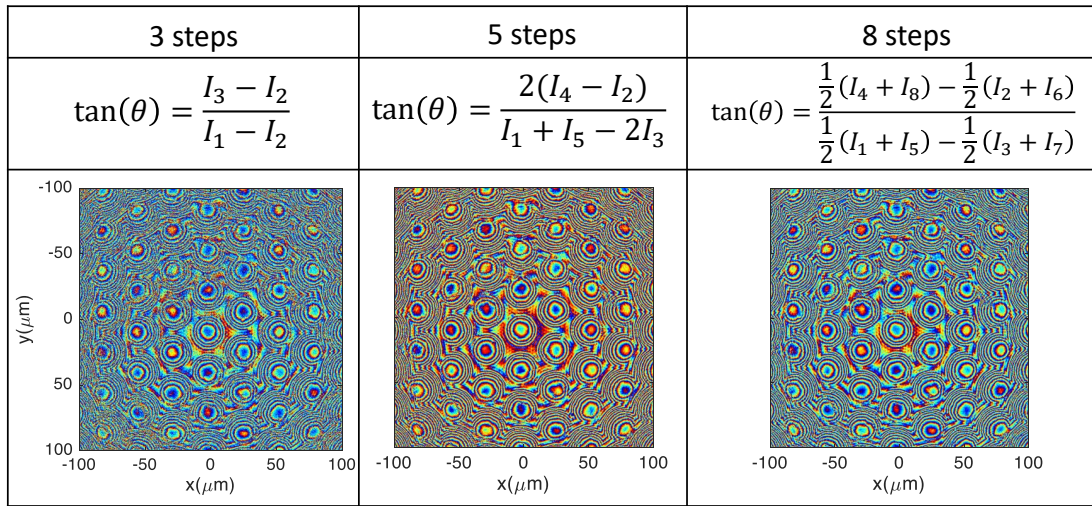


Figure 4.14: Extracting phase using 3, 5, and 8 steps PSI algorithms

References

- [1] E. P. Goodwin and J. C. Wyant. “Field guide to interferometric optical testing”. In SPIE Bellingham, WA, 2006.
- [2] M. S. Kim. On the Characteristics of Highly Confined Light Fields. Technical report, EPFL, 2011.
- [3] M. A. M. EW. “The relative motion of the earth and the luminiferous aether”. *The American Journal of Science. Third Series*, 34:333–345, 1887.
- [4] L. Zehnder. “Ein neuer interferenzrefraktor”, 1891.
- [5] L. Mach. “About an interference refractor”. *Zeitschrift f "u r Instrumentenkunde*, 12(3):89, 1892.

- [6] V. Arrizón, M. Testorf, S. Sinzinger, and J. Jahns. “Iterative optimization of phase-only diffractive optical elements based on a lenslet array”. *JOSA A*, 17(12):2157–2164, 2000.
- [7] J. W. Goodman. *Introduction to Fourier optics*. Roberts and Company Publishers, 2005.
- [8] D. Malacara. *Optical shop testing*, volume 59. John Wiley & Sons, 2007.
- [9] J. Schmit and K. Creath. “Extended averaging technique for derivation of error-compensating algorithms in phase-shifting interferometry”. *Applied optics*, 34(19):3610–3619, 1995.
- [10] J. Schmit and K. Creath. “Window function influence on phase error in phase-shifting algorithms”. *Applied optics*, 35(28):5642–5649, 1996.
- [11] K. Kinnstaetter, A. W. Lohmann, J. Schwider, and N. Streibl. “Accuracy of phase shifting interferometry”. *Applied optics*, 27(24):5082–5089, 1988.
- [12] C. L. Koliopoulos. “Interferometric optical phase measurement techniques”, 1981.
- [13] C. P. Brophy. “Effect of intensity error correlation on the computed phase of phase-shifting interferometry”. *JOSA A*, 7(4):537–541, 1990.
- [14] P. Hariharan, B. Oreb, and C. Freund. “Stroboscopic holographic interferometry: measurements of vector components of a vibration”. *Applied optics*, 26(18):3899–3903, 1987.

5 Near-field and far-field measurement for a focused source

In chapter 4, we introduced the used high-resolution interferometry microscopy (HRIM) setup. In this chapter, we present the experimentally recorded near-field and far-field for a micro-lens array (MLA) under the Gaussian beam illumination using the HRIM setup and compare with simulation results. We use an MLA with a period of 74λ which is in the refraction-diffraction regime [1] under 405 nm source wavelength. The configuration is shown in Fig. 5.1. We demonstrate that for certain values of the distance D , a high contrast pattern with a larger field of view compared to Plane wave illumination can be generated in the far-field.

5.1 Configuration

Considering the configuration in Fig. 5.1(a), a Gaussian beam illuminates the MLA at a certain distance D and the pattern distribution is recorded in the far-field observation plane. The Gaussian beam is a single-mode TEM wave with the following complex field, as we earlier explained in chapter 2 :

$$u(x, y, z = 0) = \exp\left[-\frac{x^2}{w_0^2}\right] \cdot \exp(-jkz) \quad (5.1)$$

Where w_0 is the beam waist of the Gaussian beam and $k = 2\pi/\lambda$ is the wavenumber. As we introduced the basic principles of dot generation in this thesis, for particular values of the distance D , high contrast patterns in the far-field can be achieved based on the known self-imaging phenomenon [2, 3]. According to this theory, by introducing a point source, the MLA field distribution would reproduce in the far-field for certain values of $D = \frac{mP^2}{n\lambda}$, where P is the MLA period, and m and n are integer values. However, here we employ a 2D hexagonal MLA as it is shown in the SEM image of Fig. 5.1(b). The MLA is made of fused silica with a circular lens shape and no aperture for each lens. For this geometry, there is a trigonal symmetry in the arrangement of lenses. As a result, the high contrast distance D for the hexagonal MLA is modified to be $D = \frac{3mP^2}{n\lambda}$ [4], where $P_y = 30 \mu\text{m}$. Here, we consider $n = 2$ and $m = 1$. In this case, for $\lambda = 405 \text{ nm}$, D is calculated to be 3.4 mm .

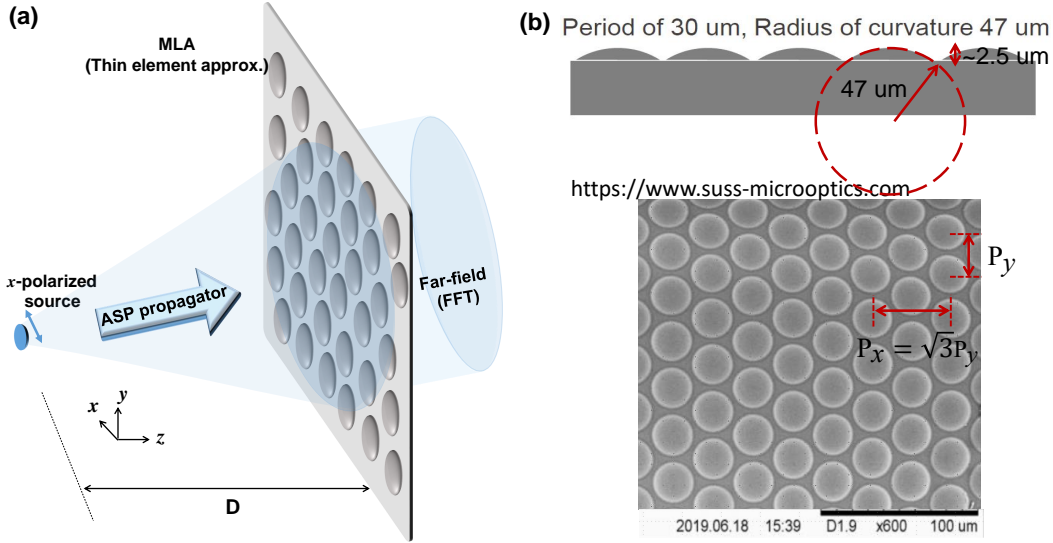


Figure 5.1: (a) Configuration under study which is an MLA under the Gaussian beam illumination, (b) lens array drawing from side view and a scanning electron microscopy (SEM) images of sample from top view.

5.2 Simulation of near-field distribution and far-field intensity

According to Fig. 5.1(a), the optical system is split into three regions. The first zone is the beam propagation from the source to MLA in which we use the angular spectrum of plane waves method (ASP) [5] that its theory is explicitly explained in chapter 2. Right after, the light propagation through the MLA is modeled using the thin element approximation (TEA) [5] because the MLA under investigation is rather flat. In our case, an MLA with a period of 30 μm and a 47 μm radius of curvature is applied. Also, the MLA refractive index is assumed to be 1.5 (fused silica). The lens is considered to be thin because its height which is 2.5 μm is much smaller than its radius of curvature of 47 μm , as it is seen in the lens drawing in Fig. 5.1(b). For a thin MLA in the experiment part, the far-field distribution field of view is small ($\pm 8^\circ$) and all the information can be easily captured by the camera in our setup. Also, we choose a thin MLA to be able to apply TEA which is not computationally extensive in a 3D simulation. In chapter 3, we discussed the validity of TEA in comparison with the rigorous simulation tools for thin and thick 1D sinusoidal phase gratings. We concluded that for a period of 50 μm , TEA is valid for a thickness of less than 12 μm or the aspect ratio of 0.24. As a result, for this optically thin MLA, applying the TEA is valid. Considering the TEA, the incoming beam only experiences a phase delay that is proportional to the MLA thickness in each point. With the output of the phase profile after the MLA, the far-field can be found by Fraunhofer approximation which is the Fourier transform of the MLA near-field [5]. The source wavelength is 405 nm. We simulated the MLA near-field phase and amplitude modulation as well as the far-field intensity for $D = 3.4$ and 4.25 mm as shown in Fig. 5.2. We choose these values to compare two high and low contrast cases according to the distance D .

5.2. Simulation of near-field distribution and far-field intensity

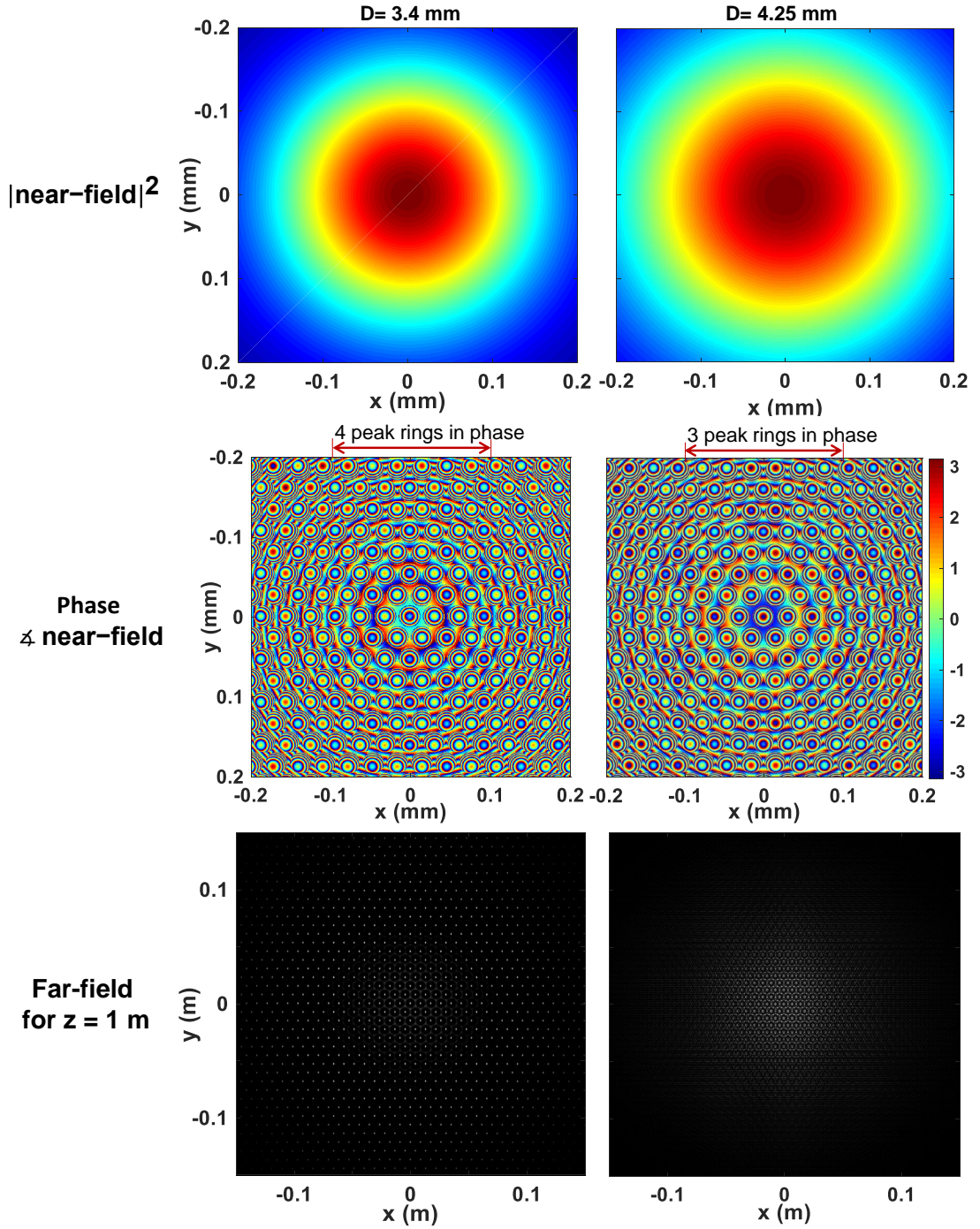


Figure 5.2: Intensity and phase near-field as well as the far-field intensity for $D = 3.4$ and 4.25 mm.

As it is seen in the near-field intensity distributions, for a larger distance $D = 4.25$ mm, the incoming beam covers more number of lenses compared to $D = 3.4$ mm. Also, the near-field intensity is not modulated by passing through the MLA, as we employ TEA in which the

field only experiences a phase delay due to the MLA surface profile. The phase near field shows a typical appearance of a phase profile for a Gaussian beam with circular equal phase rings modulated by the additional local phase distribution of the MLA. The near-field phase modulations are different due to the effect of the distance D of the source to the MLA. Although the phase profiles look similar in appearance, phase modulation is larger for $D = 3.4 \text{ mm}$ compared with $D = 4.25 \text{ mm}$ as it can be seen in the phase profiles in Fig. 5.2; it means that the incoming beam wavefront curvature is higher in the former configuration.

Here, we conclude that the two situations lead to two very different far-field patterns because of different phases and intensity distributions in the near-field. Although, finding a simplified relation between the near-field and far-field distributions is not straightforward because the far-field is the Fourier spectrum of the near-field in space. A high contrast pattern in the far-field is obtained for $D = 3.4 \text{ mm}$ with very sharp spots in comparison to the situation at distance $D = 4.25 \text{ mm}$ in which we obtain a low contrast pattern with a modified distribution of points.

5.3 HRIM setup

As shown in Fig. 5.3, we use the HRIM system in which we measure the fields for Gaussian beam and plane wave illumination. The objective (APO 20x / NA 0.4) creates an image of an observation plane on the camera. Using the 20x objective, the lateral resolution is limited by the Abbe diffraction spot size $\Delta x = \lambda / (2NA) = 506 \text{ nm}$ in air, which is sufficiently accurate for recording the MLA near-field.

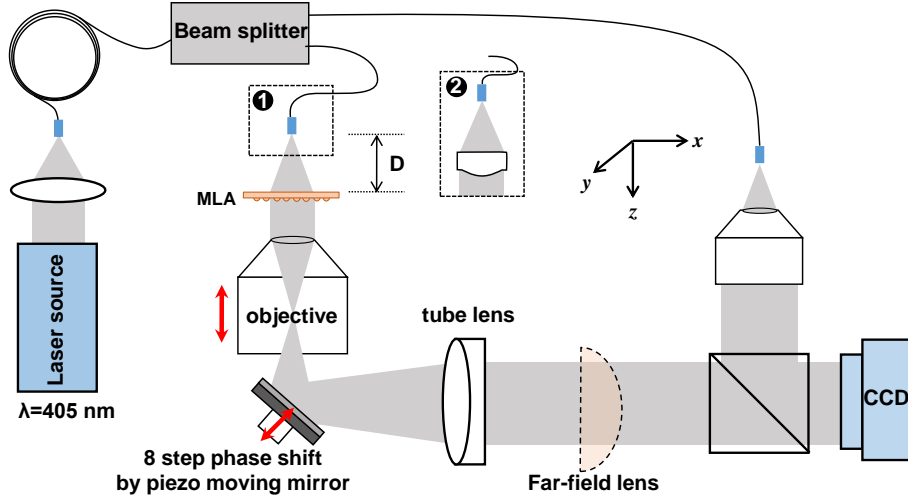


Figure 5.3: The schematic of HRIM setup for recording the phase and intensity.

For Gaussian beam illumination, we use the configuration number 1 in Fig. 5.3 as the source. For the plane wave illumination, we replace this configuration with configuration number 2 in

Fig. 5.3 and use the collimated beam. To record the far-field intensity pattern, we block the reference arm and use the far-field lens (as shown in Fig. 5.3) to observe the Fourier image on the camera sensor (projected far field). All details of optical setup and measurement steps are explained explicitly in chapter 4.

5.4 Experimental results

Here, we record the near-field and far-field for different configurations; the plane wave illumination and Gaussian beam source for $D = 3.4$ and 4.25 mm. Figure 5.4 shows near field intensity (similar to normal microscope image), the near-field phase which is extracted based on the interferometry technique, and the corresponding far-field distribution. As seen, there is no strong near-field intensity modulation for this thin lens array. As we also observed in the simulated near-field intensities, the incoming beam covers more number of lenses for plane wave and $D = 4.25$ mm compared to $D = 3.4$ mm. Furthermore, the near-field phase modulation shows the effect of the Gaussian beam wave-front in comparison to the uniform wave-front of plane wave illumination.

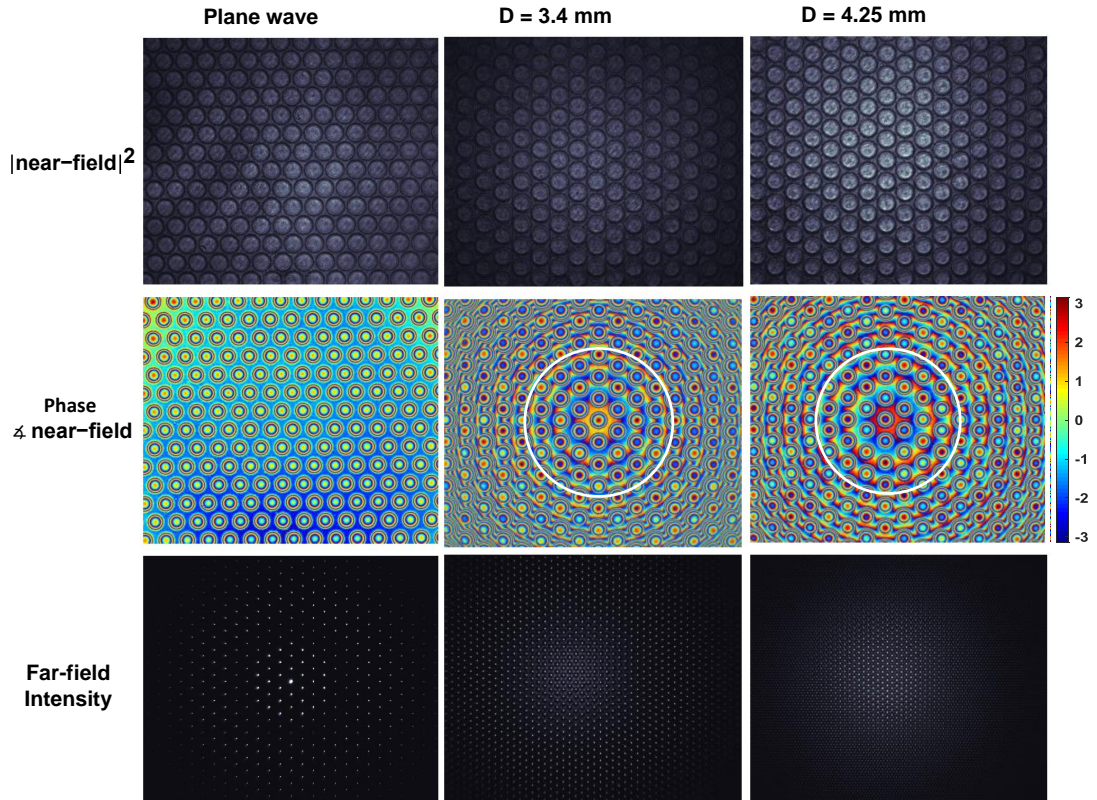


Figure 5.4: The recorded phase and intensity near-field as well as the far-field intensity distribution using the HRIM setup. Two areas are determined by white circles in the phase profile images, for comparison.

As shown in the areas which are determined by white circles in the phase images in Fig. 5.4, the wave-fronts modulation is larger for $D = 3.4 \text{ mm}$, showing that the Gaussian beam has higher curvature in this case. According to the phase and intensity modulation in the near-field, one obtains a high contrast pattern in the far-field for $D = 3.4 \text{ mm}$ and a low contrast pattern for $D = 4.25 \text{ mm}$, as it is seen in far-field distributions.

Finally, we observe a high contrast dot pattern with a wider field of view under the Gaussian beam illumination for $D = 3.4 \text{ mm}$ in comparison to a plane wave. It demonstrates that by applying a diverging Gaussian beam instead of a Plane wave, we can obtain more number of points with a larger field of view if D is set to the appropriate values that were discussed in the simulation part. Our experimental approach allows us to record both the phase and amplitude in different planes and compare with simulation results to obtain a deeper understanding of our structured generator configuration.

5.5 Summary

We theoretically and experimentally investigated the structured pattern generation in far-field for an MLA under the Gaussian beam illumination in comparison to the Plane wave. The MLA period is 74λ , the regime in which the optical effects are governed by both diffraction and refraction. For Gaussian beam illumination, a high contrast pattern is observed in the far-field for certain distances between the source and the MLA in which the self-imaging condition for point source illumination is satisfied. In the simulation part, we compared the MLA near-field and the resulting far-field distributions for different distances between the source and the optical element. In the experimental part, we used the HRIM setup for recording both the phase and intensity of MLA near-field and also the far-field distribution. Using this setup, by recording both the phase and amplitude distributions, more information can be extracted compared to a normal microscopy configuration. In this setup, we added this flexibility to be able to compare the Plane wave with the Gaussian beam illumination condition. We demonstrated that the near-field phase modulation and the resulting far-field distribution are not the same for Plane wave and Gaussian beam. Under the Gaussian beam, we obtained more number of points in the far-field with a larger field of view in comparison with the Plane wave illumination, for particular distances between the Gaussian beam and MLA.

References

- [1] B. C. Kress. "Field guide to digital micro-optics". In SPIE, 2014.
- [2] J. Jahns and A. W. Lohmann. "The lau effect (a diffraction experiment with incoherent illumination)". *Optics communications*, 28(3):263–267, 1979.
- [3] S. Som and A. Satpathi. "The generalised lau effect". *Journal of Modern Optics*, 37(7):1215–1225, 1990.

- [4] J. Wen, Y. Zhang, and M. Xiao. “The talbot effect: recent advances in classical optics, nonlinear optics, and quantum optics”. *Advances in optics and photonics*, 5(1):83–130, 2013.
- [5] J. W. Goodman. *Introduction to Fourier optics*. Roberts and Company Publishers, 2005.

6 Analysis of Photonic Nanojet (PNJ) for different illumination conditions

A photonic nanojet (PNJ) is a high intensity narrow propagating electromagnetic beam with a sub-wavelength dimension that is generated in the shadow side surface of a dielectric micro-particle under the plane wave[1], as seen in Fig. 6.1. Furthermore, the PNJ is generally a non-evanescent propagating beam and a non-resonant phenomenon that can be applied to a wide range of sphere diameters until a certain limit [2]. Due to this property of the PNJ and also its small dimensions that can be smaller than the diffraction limit of $\lambda/2$, the PNJ is regarded as foundation of a wide range of applications including super-resolution optical imaging [3, 4], nanoparticle optical detection [5, 6], nanoparticle optical trapping [7, 8], data storage [9], etc.

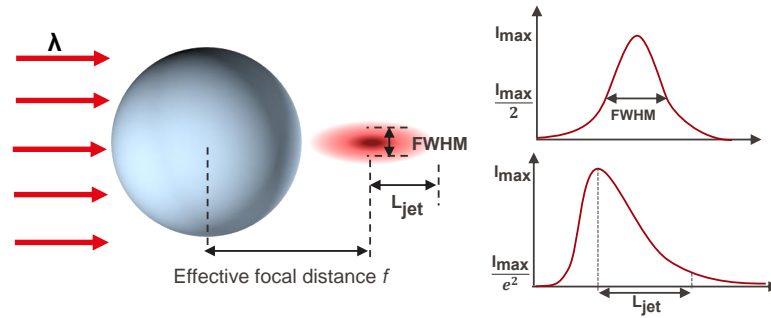


Figure 6.1: Schematic of the PNJ parameters for a dielectric sphere under an illuminating beam with the wavelength of λ .

As it is seen in Fig. 6.1, the PNJ can be characterized by key parameters including the full-width at half maximum (FWHM), effective focal length or distance of hotspot from the structure, nanojet length, and the field enhancement that has been studied and manipulated in various works. The most important property, influencing the PNJ characteristics is structure geometry (i.e. particle size and shape) that has been studied and manipulated in numerous works [10–15]. Also, the effect of structure optical properties i.e the contrast between the particle and the surrounding medium refractive index on PNJ parameters has been investigated [1, 16],

especially multi-layer graded-index structures that have been applied in numerous studies [12, 17–22]. Furthermore, we can manipulate the PNJ properties by modifying the source characteristics including wavelength, polarization, intensity distribution, coherence, etc.[16, 22].

6.1 PNJ as source near-field modulator for structured light generation

As we discussed in previous chapters, one of our structured light generation strategies is the diverging source modulation by applying a micro-particle in the source near-field, as it can be seen in Fig. 6.2, as a reminder from previous chapters. Applying the micro-particle at the Gaussian beam near-field, a PNJ is generated in the shadow side surface of the structure depending on the particle geometry, size, refractive index, and also illumination condition. The generated PNJ in the Fig. 6.2, is a new source with new optical properties that engineers the structured light generation. For this reason, it is important to study the PNJ generation under different illumination conditions and micro-particle sizes. In this chapter, we will theoretically study the PNJ behavior under different illumination conditions of source numerical apertures and also particle sizes.

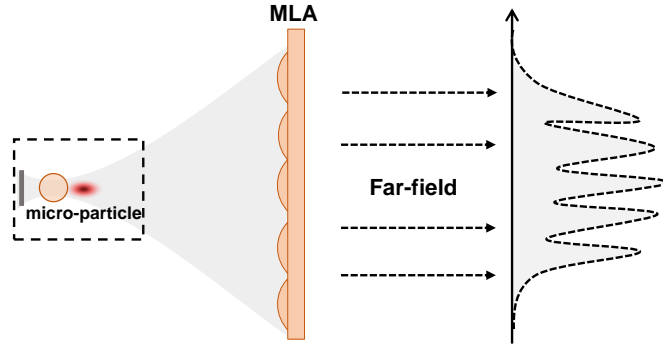


Figure 6.2: Schematic of engineering structured light generation by applying a micro-particle at diverging source near-field.

In most of the works, the configuration assumed is under plane wave illumination. One reason is that it is much easier to do the calculations. A few papers have been reported, considering the non-planar and spherical wavefront sources [23–27]. In Ref. [26], the PNJ has been experimentally observed for a sphere diameter of $12\ \mu\text{m}$ under diverging and converging spherical wavefront curvatures but no detailed study and guidelines have been presented for different sphere diameters and source curvatures. In this chapter, we propose a configuration in which we can systematically investigate the effect of curved wavefront sources (from low to high NA of 0.8) apart from the effect of beam diameter for sphere sizes of 1 to $20\ \mu\text{m}$. To our knowledge, such a situation is neglected by papers but leads to a fundamentally different PNJ behavior for converging and diverging source curvatures.

From the practical point of view, the PNJ is often generated using a microscope objective to illuminate a microsphere, as seen in Fig. 6.3(a). In such a setting which is similar to the illumination part in our interferometry setup, it is very tricky to determine the absolute position of the sphere with respect to the incoming beam. It is because of that the active alignment is used in the experiment and one usually searches for the best spot which might not be at the plane wave illumination distance [3]. For heavily focused beams using a large NA objective, a small displacement of the sphere along the axis around the incoming beam focal point can significantly influence on the generation of PNJ. Our theoretical findings show that the PNJ has completely different behaviors for different positions of the particle around the microscope objective focal point and our investigation is helpful to understand the observations in the experiments from our interferometry setup measurements.

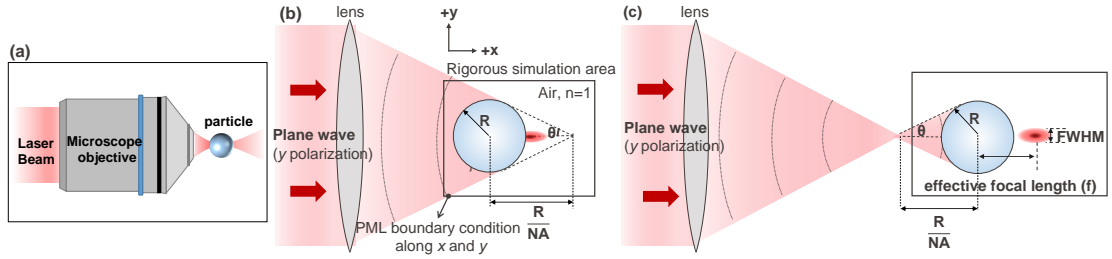


Figure 6.3: (a) Using a microscope objective to illuminate a microparticle in practical applications. (b) and (c) The schematics of our configuration under study for converging and diverging beam hitting the particle, respectively. The microscope objective is modeled by a thin lens under the plane wave that focuses the beam with the numerical aperture of NA.

6.2 Configuration

Our proposed configurations are shown in Fig. 6.3(b) and (c). The illuminating beam that in practice is focused by employing a microscope objective in Fig. 6.3(a), is modeled by making use of a lens under plane wave illumination (beam propagation is along $+x$). The focusing beam wave-front curvature changes by changing the lens focal distance, and in such a way sources of different NAs from low to high are generated. Then, the beam out of lens illuminates a microsphere of radius R to form PNJ. Assuming the sphere position to be before the lens focal point along x axis, the converging beams hit the sphere, as shown in Fig. 6.3(b) and considering the sphere to be located after the lens focal point, the diverging beams cover the sphere, according to Fig. 6.3(c). A similar configuration has also been proposed in Ref. [28] for investigating the effect of high NA sources on PNJ for a fused silica particle with a diameter of $2\ \mu\text{m}$. To do a systematic investigation by changing the source NA for all the sphere sizes, we choose the sphere position such that it is fully covered by the illuminating beam but the beam does not transmit through the surrounding medium in the air. To design such configuration, assuming the lens numerical aperture to be $\text{NA} = \sin(\theta)$, the sphere position with respect to lens focal point can be geometrically calculated which is $+\frac{R}{\text{NA}}$ for converging area and $-\frac{R}{\text{NA}}$ for

diverging area. The advantage of implementing such configuration is that the whole sphere is fully illuminated by the beam for all the sphere radii of R and we can consistently compare the effect of source wavefront curvature for different sphere sizes.

Several techniques have been used to solve the problem such as the analytical Mie theory [26], finite difference time domain (FDTD) and finite element method (FEM) [20, 24–26]. We perform 2D FDTD simulations using the software package of Lumerical FDTD [29] in which the focused beam out of the lens is modeled using thin element approximation [30] to generate a high NA source input for rigorous simulations. The rigorous 2-D simulation area is shown in Fig. 6.3 (b) and (c) and the perfect match layers (PML) boundary condition is implemented along x and y axis. The source wavelength is 600 nm and polarized along y axis. The sphere has a refractive index of $n = 1.5$ and the surrounding medium is air with a refractive index of unity. In this work, we investigate two main parameters of a PNJ: Effective focal length (f) and the full width at half maximum (FWHM). As seen in Fig. 6.3(c), the effective focal length f is the distance between the center of the sphere and the point in which the PNJ intensity is maximum [24].

We start by comparing the PNJ behavior under a converging, diverging, and plane wave illumination for a sphere of $5\text{ }\mu\text{m}$ diameter to illustrate the effect of source curvature. Plane wave illumination case is considered as a reference for comparison. Later on, we compare a small ($2\text{ }\mu\text{m}$ diameter) and a large microsphere ($15\text{ }\mu\text{m}$ diameter). In the rest of the paper, we analyze the PNJ in more detail for different source NA of 0.1, 0.2, 0.4, 0.6, and 0.8 and for various sphere diameters of 1, 2, 5, 10, 15, and $20\text{ }\mu\text{m}$. The simulation results show that the PNJ has a completely different behavior under converging and diverging illuminations by changing the sphere size. For diverging beam, the PNJ is localized outside the sphere, and its FWHM increases for large source NAs. For the very high NA of 0.8 and large sphere sizes of 15 and $20\text{ }\mu\text{m}$, no PNJ is generated as the sphere behaves as a diffractive-refractive ball lens. In contrast, under the converging beam, the FWHM in most cases is smaller than plane wave and the PNJ moves toward the center of the sphere by increasing the source NA. For the high NA converging beam, the PNJ is located inside the sphere. Finally, we find an analogy between the PNJ behavior by changing the source NA for the sphere refractive index of n in comparison with changing the sphere refractive index of n under plane wave illumination.

6.3 Results and discussion

To introduce the subject, we choose an example with fixed parameters. We first investigate the PNJ of a microsphere under the diverging and converging sources with NA of 0.4 and compare it with the plane wave illumination for a sphere diameter of $5\text{ }\mu\text{m}$ at 600 nm wavelengths (sphere diameter 8.3λ). Results are shown in Fig. 6.4 in three representations: amplitude, phase, and Poynting vector streamlines. From the amplitude distributions in Fig. 6.4, one observes that the hot spot is formed inside the sphere for the converging source, while it moves to the outside of the sphere for plane wave and diverging beam i.e providing a bigger effective

focal length f . It demonstrates that the sphere behaves like a ball lens and for this reason, the hotspot moves along the propagation direction by going from converging to the diverging source.

The FWHM under plane wave is 0.53λ . Compared to plane wave illumination, the FWHM is increased by 92% from 0.53λ to 1.02λ , for the diverging beam while it is decreased by 25% from 0.53λ to 0.4λ for converging beam. Rather than the source wavefront curvature, the FWHM can also be explained by the refractive index of the medium in which the hot spot is formed. In the case of a converging beam, as the hot spot is localized inside the sphere of refractive index n , the FWHM is n times smaller than the hot spot in the air; meaning that the FWHM is $0.53\lambda/1.2 \approx 0.44\lambda$. In the following sections, we will demonstrate that the FWHM can even go down to smaller dimensions than FWHM/n for high NA converging beams.

As seen from Poynting vector streamlines, the energy flow around the hot spot is not the same for all illuminating beam curvatures. For the converging beam, the Poynting vectors around hot spot are mostly scattered outside although for diverging beam, the hot spot is elongated along the propagation direction since the Poynting vectors around the focal point are almost parallel. Furthermore, the Poynting vector streamlines confirm the propagating character of the PNJ as the vector's intensity is higher at the hot spot position for all the illuminating beam conditions. Also, the phase distributions in Fig. 6.4 compare the incoming beam wave-front curvatures as well as the wave-front modulations around the hot spot. As seen, a hot spot with a higher NA is generated for a converging beam in comparison with diverging beam and plane wave illumination.

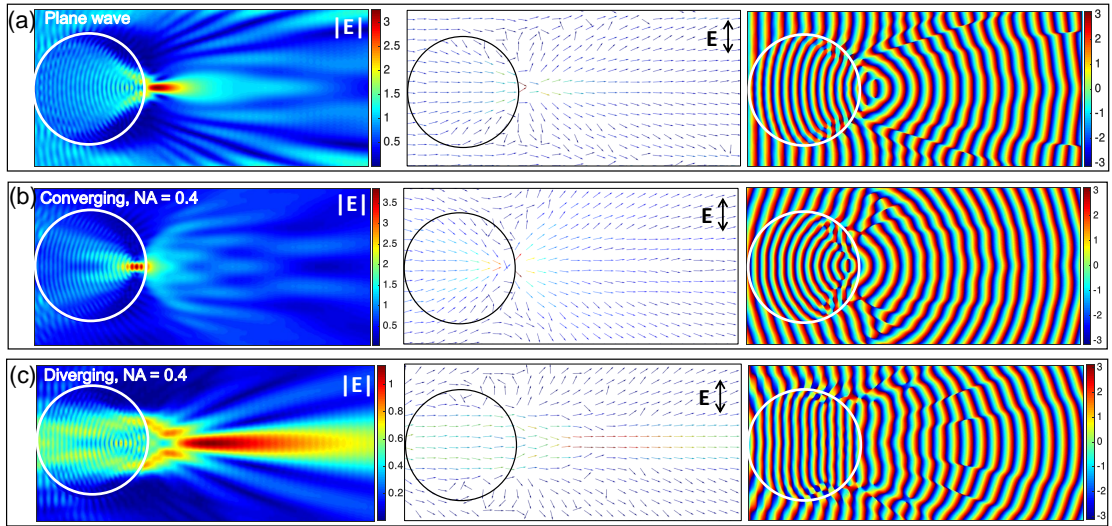


Figure 6.4: The dielectric microsphere under different source curvatures for the sphere diameter of $5\ \mu\text{m}$. The field distribution, Poynting vector streamline and phase distribution for (a) the Plane wave, (b) converging source, $\text{NA} = 0.4$, and (c) diverging source, $\text{NA} = 0.4$. Please note that the scale for amplitude distributions are different.

6.3.1 Comparison of the PNJ for the sphere diameter of 3.3λ and 25λ

Here, we demonstrate that even for small diameters of the spheres, the PNJ, still strongly depends on the incident wavefront of the illumination and hence cannot be seen as a scattering phenomenon only. Figure 6.5 shows the evolution of PNJ for the small sphere diameter of $2\ \mu m$ (or 3.3λ) in comparison with a much larger diameter of $15\ \mu m$ (or 25λ) under the diverging, converging beam of $NA = 0.4$ and plane wave illumination. The PNJ for the sphere diameters of 2 and $15\ \mu m$ have the following common aspects which were also observed in Fig. 6.4 for the sphere diameter of $5\ \mu m$: From the field distributions, one observes that for the converging beam the hot spot is formed inside the particle with a smaller FWHM in comparison with diverging and plane wave illumination in which the hot spot is localized outside the sphere and elongated along the propagation direction with a bigger FWHM. Also as seen from the phase modulations for both sphere dimensions, a hot spot with a higher NA is obtained for the converging beam compared with the plane wave and diverging beam.

On the other side, the PNJ for small and big diameters of 2 and $15\ \mu m$ has the following different aspects: According to the field distributions, the PNJ behaves similarly to a ball lens for the sphere diameter of $15\ \mu m$, meaning that the side lobes around the hot spot are pronounced, especially under the plane wave and diverging beam. It can be explained by the lens aberration for large sphere sizes. Although, for the small sphere diameter of $2\ \mu m$, the side lobes are diminished around the hot spot. Figures 6.5 (b) and (d) compare the transverse intensity profiles at hot spot plane, for 2 and $15\ \mu m$ diameters, clarifying the intensity distribution in side lobes. Furthermore, the effective focal length f increases by 83% for the diameter of $15\ \mu m$ by going from converging to diverging source although, f increases by 40% only for the diameter of $2\ \mu m$ (dimensions normalized to the sphere size). This comparison confirms that the lens behavior of the sphere is dominant for the large sphere diameter of $15\ \mu m$. For this reason, we will more deeply investigate the PNJ behavior for the sphere diameter of 1 to $20\ \mu m$ (or 1.6λ to 33λ).

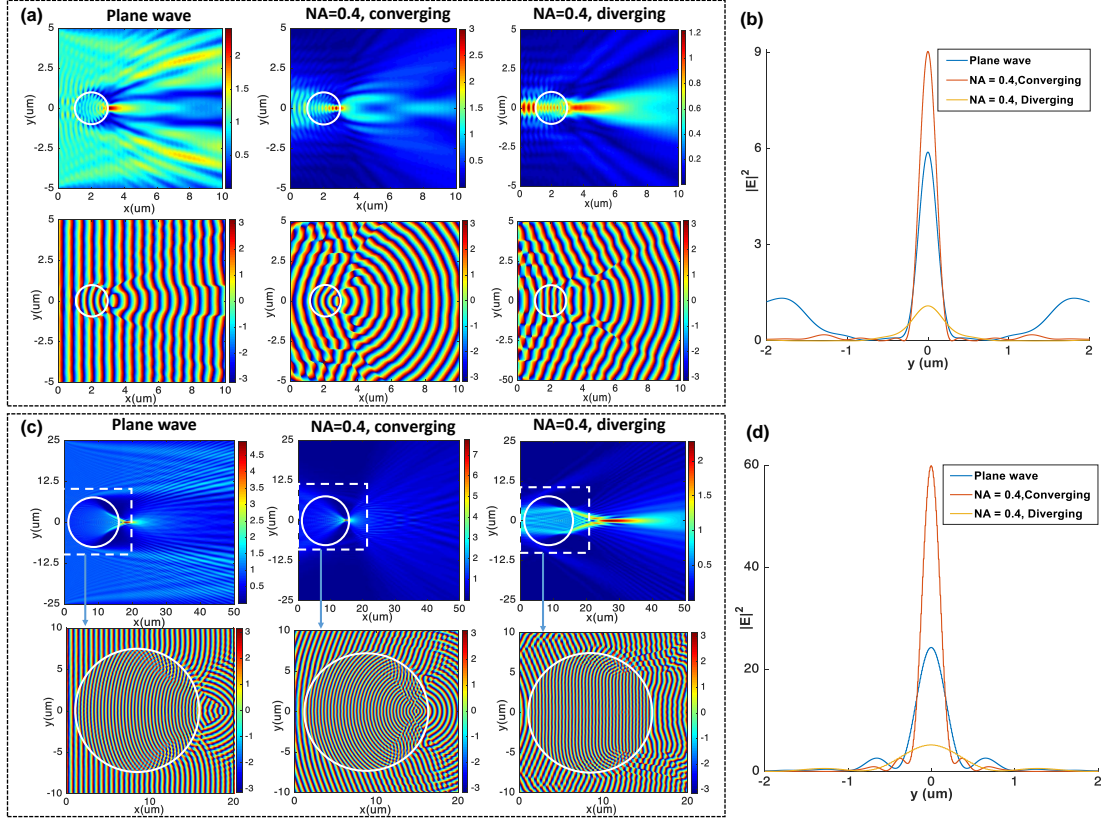


Figure 6.5: (a) and (c) Electric field amplitude and phase distribution for sphere diameters of 2 and $15 \mu\text{m}$, respectively, under plane wave, converging and diverging illumination with $\text{NA}=0.4$, (b) and (d) their corresponding transverse Intensity profile at hot spot position. Please note that the scale for amplitude distributions are different.

6.3.2 FWHM and effective focal length f versus the sphere diameter d for diverging beam

In this section, we study more systematically the PNJ for a sphere of diameter between 1 to $20 \mu\text{m}$ and with changing the source numerical aperture NA from 0.1 to 0.8 . We concentrate on the diverging source and compare it with the plane wave illumination as a reference. As seen in Fig. 6.6(a), the effective focal length f for all NA s and also for the plane wave illumination is greater than $f = d/2$, i.e that the hot spot is generated in air, outside the sphere in all the cases. Also for every source NA , the effective focal length f tends to increase for large diameter d . For plane-wave and source NA s of 0.1 and 0.2 , f linearly increases as a function of d . For $\text{NA} > 0.2$, the linear behavior of the curve vanishes and f significantly increases for large diameter d . For the high NA of 0.8 , no hot spot is generated in practice for the large diameters of $15 \mu\text{m}$ (or 25λ) and $20 \mu\text{m}$ (or 33.3λ) because of that the sphere behaves like a lens that collimates the beams.

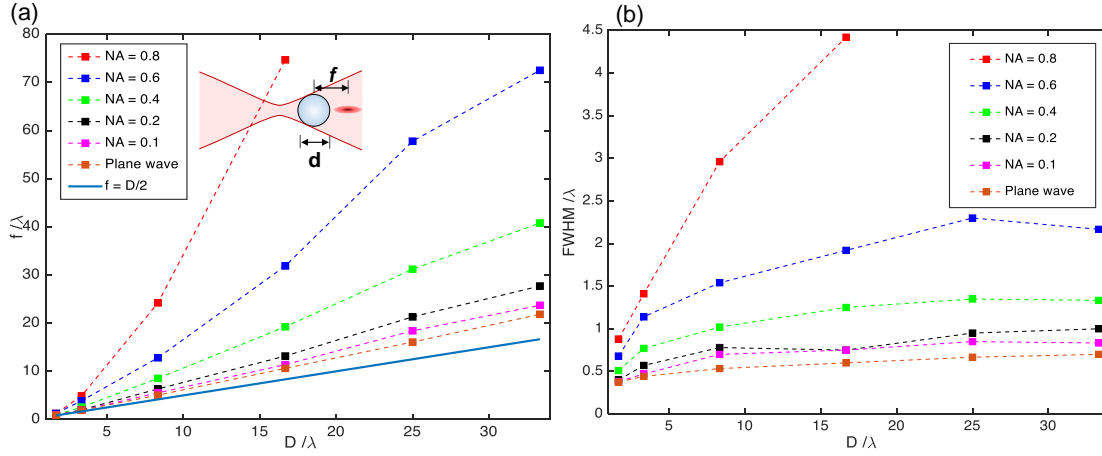


Figure 6.6: PNJ characteristics as a function of the sphere diameter d for diverging beam by changing the source NA in comparison with the plane wave illumination. (a) effective focal length f , and (b) FWHM.

As seen in fig. 6.6(b), the smallest FWHM is achieved under the plane wave illumination for all the sphere diameters d . Also for all the source NAs, the FWHM generally increases as the particle diameter d increases, providing a larger focus. For the source NAs below 0.4, the FWHM with respect to d is almost a stable function. By further increase of NA, the FWHM tends to increase steeply as a function of d , and for the high NAs of 0.6 and 0.8, the FWHM is much larger than the plane wave illumination. For a high NA of 0.8, no PNJ is formed for the large diameters of $15\mu m$ (or 25λ) and $20\mu m$ (or 33.3λ), as we explained earlier. Finally, Figure 6.6 emphasizes that the generation of PNJ as a function of the sphere diameter d is much more sensitive for a high NA diverging source than plane wave illumination. This point should be carefully considered when employing the high NA objective to generate the source for optical trapping applications [8], etc.

To explore the lens behavior of sphere for high NA diverging sources as a function of sphere diameter d , we show the field distributions in Fig. 6.7 for the source NA = 0.8 and various sphere diameters of $1, 2, 5, 10, 15$, and $20\mu m$. As seen in Fig. 6.7(a) and (b) for small sphere diameters of $1\mu m$ (or 1.6λ) and $2\mu m$ (or 3.3λ), a PNJ is formed outside the sphere. For diameters of $5\mu m$ (or 8.3λ) and $10\mu m$ (or 16.6λ), the hot spot is elongated along the propagation direction having side lobes around the central lobe (Fig. 6.7(c) and (d)). The side lobes around the hot spot for this range of diameters are the effect of aberration that demonstrates a transition from the PNJ scattering origin to the behavior of a ball lens having aberrations. According to Fig. 6.7 (e) and (f) for $15\mu m$ (or 25λ) and $20\mu m$ (or 33.3λ) diameter, the sphere behaves as a lens and collimates the beam out of the sphere although the diffracted beams are also visible in the collimated beam i.e that the sphere in practice is a diffracting lens. In this case, no PNJ is generated.

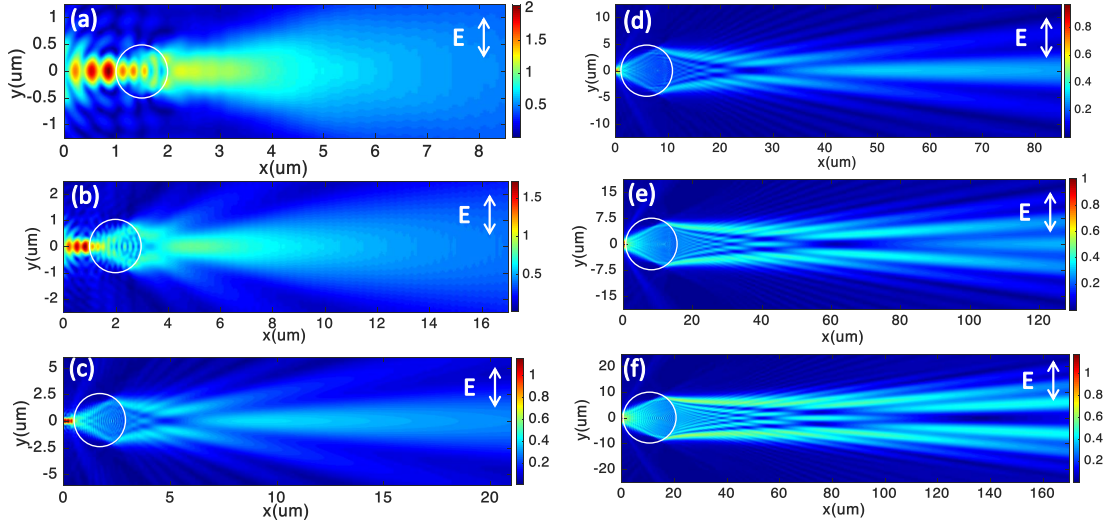


Figure 6.7: Field distribution for diverging source curvature of high NA of 0.8 for sphere diameters of (a) 1, (b) 2, (c) 5, (d) 10, (e) 15 and (f) 20 μm . Please note that the scale for amplitude distributions are different.

6.3.3 FWHM and effective focal length f versus the sphere diameter d for converging beam

Here, we study the evolution of PNJ as a function of sphere diameter d for converging beams with different NAs in comparison with the plane wave illumination. As seen in Fig. 6.8(a), the effective focal length f linearly increases by increasing the particle diameter d for all NAs of the converging beam, and the plane wave illumination. For larger NAs, the slope of the effective focal length curve decreases, the PNJ immersing inside the sphere for NA of 0.4, 0.6, and 0.8 (The curves are below $f = d/2$). In contrast, the PNJ is localized in the air, outside the sphere for Plane wave and the low NA of 0.1 and 0.2.

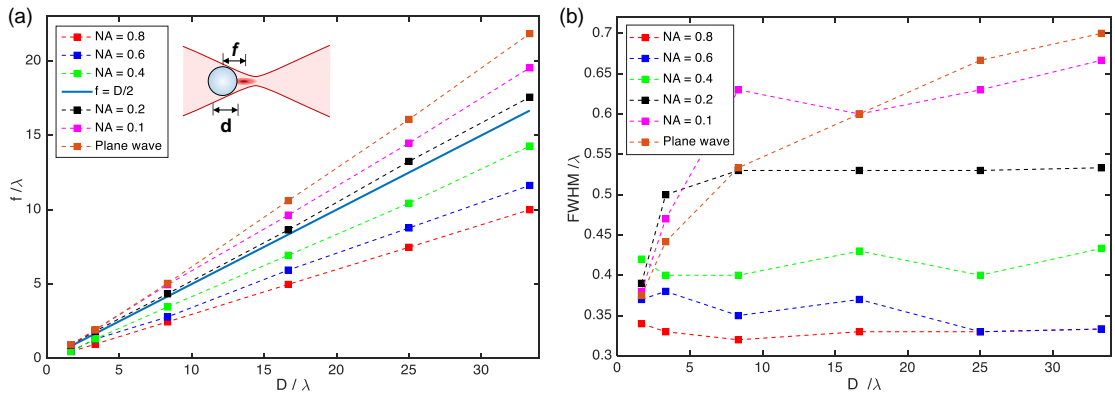


Figure 6.8: PNJ characteristics as a function of the sphere diameter d for converging beam by changing the source NA in comparison with the plane wave illumination. (a) effective focal length f , and (b) FWHM.

As seen in Fig. 6.8(b) for low NA of 0.1 and 0.2, the FWHM variation follows more closely the plane wave illumination, the cases that the PNJ is located outside the sphere in the air. Although for the high NA of 0.4, 0.6, and 0.8, the FWHM curve is slowly varying as a function of the sphere diameter d . The similar trend between these curves also comes from the fact that the PNJ is localized inside the sphere for all these cases. Also, the FWHM can go down to 0.33λ for converging sources of high NA 0.6 and 0.8 even for large sphere diameters d although, for plane wave illumination, the FWHM increases for large sphere diameters and reaches 0.7λ . The achieved ultra-narrow FWHM width for high NA sources is not only because of the medium refractive index n but also highly depends on the source NA. In summary, using a high NA microscope objective as the source in the experiment, we have to carefully consider that there is this possibility that the PNJ is generated inside the particle and no field enhancement is achieved outside the sphere to apply for optical trapping [8] and other applications, etc.

6.3.4 The analogy between converging source NA and sphere refractive index n

As we discussed, the PNJ for a glass sphere with a refractive index of 1.5 moves in the opposite direction of field propagation, toward the sphere surface by increasing the converging source NA and the PNJ is immersed inside the sphere for NA = 0.4, 0.6, and 0.8. On the other side, it is known that for Plane wave illumination, according to the geometrical optics, the focal length of the ball lens with the radius of R and the refractive index of n is given by [31].

$$f = \frac{R}{2} \left(\frac{n}{n-1} \right) \quad (6.1)$$

According to this equation, the focal point is outside the sphere for $n < 2$. For $n = 2$, the focal point is at the sphere surface. And for $n > 2$, the focal point is inside the sphere and moves toward the center of the sphere by a further increase of the refractive index n [31]. This geometrical optics approximation for the focal length of the ball lens under plane wave follows similar behavior as increasing the converging source NA for a glass sphere that was discussed above. To provide more insight we show in Fig. 6.9 the field distribution for a glass sphere of $15\mu m$ diameter under a converging beam in comparison with a sphere with a refractive index of 2.5 under plane wave illumination. As seen, the PNJ is localized inside the glass sphere under the converging beam and also for the high refractive index sphere under the plane wave illumination[1, 18]. It means that the effect of large source NA is equivalent to a high refractive index sphere under the plane wave. Although, a PNJ with a higher NA is generated for converging source in comparison with the high refractive index sphere under plane wave illumination, as seen in Fig.6.9.

Next, we compare a small and a big diameter of 2 and $15\mu m$. The curves in Fig. 6.10, show the effective focal length f and FWHM for $n = 1.5$, by changing the source NA from zero to 0.8, in comparison with the plane wave illumination by changing the refractive index n between 1.5 and 2.5. When comparing Fig. 6.10 (a) and (b), we find a similar trend between the effective focal length curves versus the NA and refractive index n . As seen in Fig. 6.10 (a), the PNJ

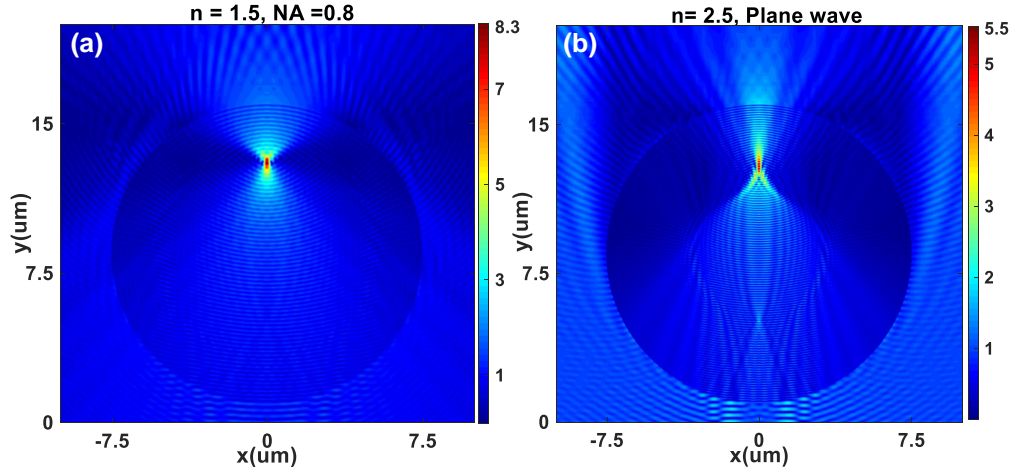


Figure 6.9: Electric field distribution for a sphere diameter of 15 μm under (a) converging source (NA=0.8) and sphere refractive index of 1.5 in comparison with (b) plane wave illumination and sphere refractive index of 2.5. Please note that the scale for amplitude distributions are different.

is localized inside the sphere for $NA > 0.25$ for both the sphere diameters of 2 and 15 μm . According to Fig. 6.10(b), the PNJ for a sphere diameter of 15 μm , is localized inside the sphere for $n > 1.8$ although, for the small diameter of 2 μm , the PNJ is immersed inside the sphere for $n > 1.6$; i.e. that f as a function of refractive index n is more sensitive than f versus the source NA for small and large sphere diameters. It can also be seen from Fig. 6.10(b) that using the ray-tracing equation, the beams are focused inside the sphere for $n > 2$ for both the sphere diameters of 2 and 15 μm , showing that the ray tracing does not include the effect of particle size although, f depends on both the refractive index n and size of the sphere, for this diffractive lens [16, 17].

As seen in Fig. 6.10 (c) and (d), the FWHM tends to decrease for larger source NA and refractive index n [21]. For the large diameter of 15 μm , both curves in Fig. 6.10(c) and (d) follow similar trends although, for the small diameter of 2 μm , the curves behave differently. On the other side, the minimum FWHM obtained value as a function of NA is 0.33λ although the FWHM can go down to 0.25λ for large refractive index of 2.5.

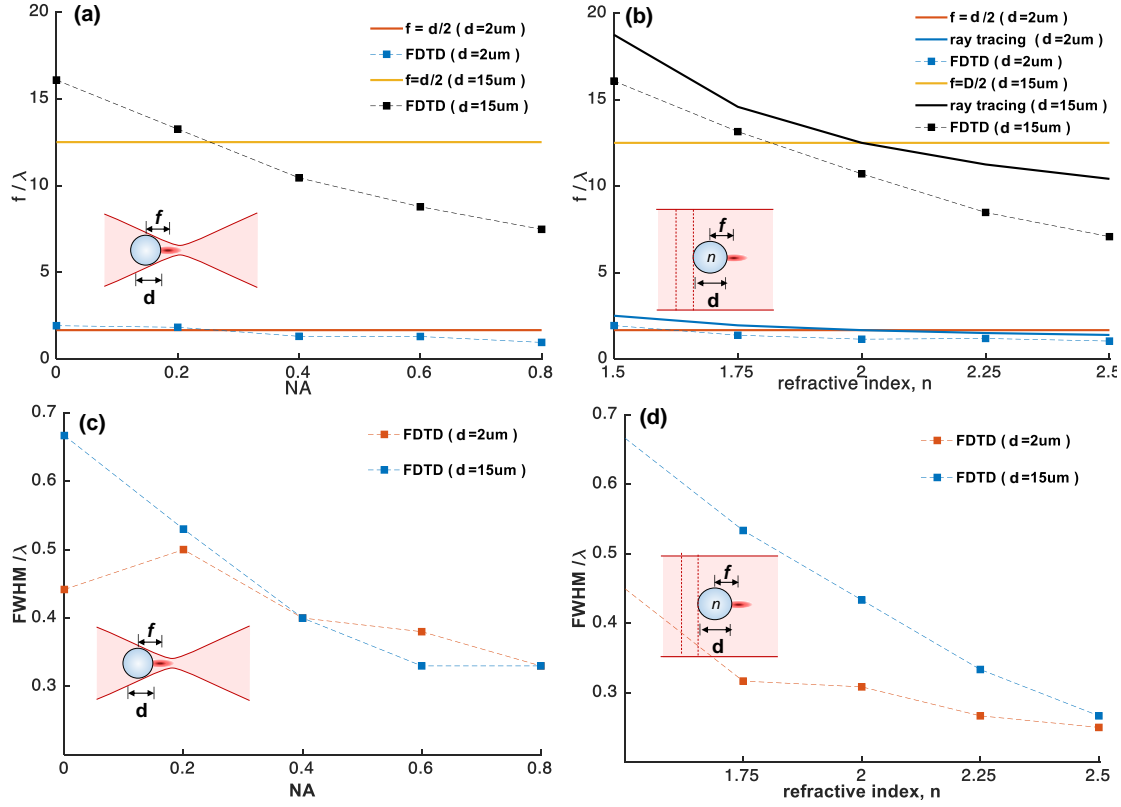


Figure 6.10: Comparison between the increase of source NA and sphere refractive index n for the sphere diameters of 2 and $15\mu\text{m}$. (a) Effective focal length f versus converging source NA for glass sphere, (b) Effective focal length f versus sphere refractive index n under a plane wave (c) FWHM versus converging source NA for glass sphere and (d) FWHM versus sphere refractive index n under plane wave.

6.3.5 Comparison between 2D and 3D simulations

In a real practical scenario, the micro-structure is a three-dimensional (3D) sphere that is illuminated by a microscope objective however our simulations are 2D. In Ref. [32], the behavior of PNJ is studied for 3D spheres in comparison with the 2D cylinder geometries for a diameter of 1 to $5\mu\text{m}$ under plane wave illumination. The optical characteristics of PNJ for 2D and 3D geometries are different however, they follow a similar trend as a function of structure diameter. In this section, we compare the optical characteristics of PNJ for cylinders and spheres of 1 and $5\mu\text{m}$ diameter under different source wavefront curvatures. For the sphere diameters larger than $5\mu\text{m}$, 3D simulation is computationally extensive and it is not practical.

In Fig. 6.11 (a), the evolution of PNJ is shown for a sphere diameter of $1\mu\text{m}$ under converging and diverging sources (NA = 0.4, 0.8) in comparison with plane wave illumination. For both the 2D and 3D geometries, by going from high-converging to high-diverging source, the formed PNJ moves along the direction of propagation ($+x$). However, for all the illumination

conditions, a longer PNJ is realized for a cylinder compared to 3D sphere geometry [32].

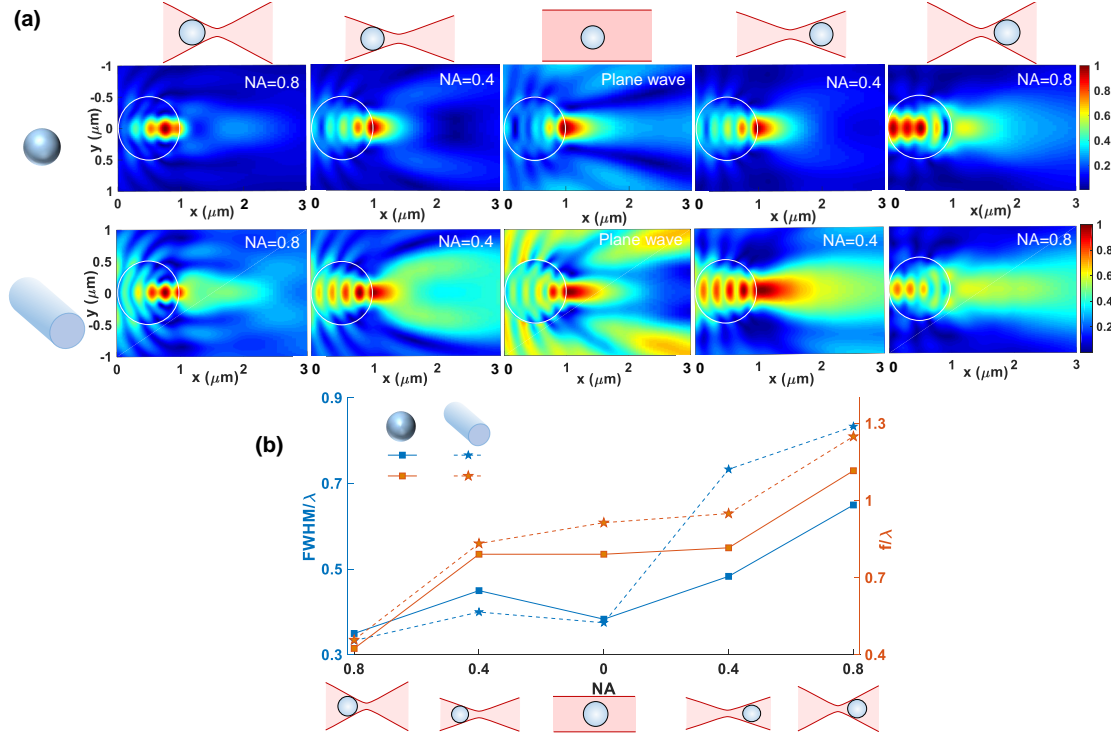


Figure 6.11: (a) Comparison between the electric field distribution of cylinder and sphere under converging, diverging sources ($NA = 0.4$ and 0.8), and plane wave illumination. The cylinder and sphere diameter is $1 \mu m$. (b) The extracted FWHM and effective focal length f of PNJs for the configurations in (a).

In Fig. 6.11 (b), the FWHM and effective focal length f of the PNJs are shown. As seen, the optical characteristics of PNJ are not equal for cylinder and sphere, however, both configurations show a similar trend under different wave-front curvatures. Going from high-converging to a high-diverging source, the following tendencies are observed in the curves for both cylinder and sphere: The FWHM is increased, except that a dip is realized in the FWHM curves in the case of plane wave illumination. Also, the effective focal length of f tends to increase.

In Fig. 6.12(a), the field distributions are demonstrated for a larger sphere diameter of $5 \mu m$. As it is observed, the PNJ moves along the direction of propagation by going from high converging to a high-diverging source wave-front. Moving the hot spot along the direction of propagation is more pronounced for a diameter of $5 \mu m$, compared to the smaller diameter of $1 \mu m$. Also, the PNJ is elongated along the propagation direction with a longer length for cylinder compared to a sphere geometry. In Fig. 6.12(b), the FWHM and effective focal length (f) of PNJ are compared for cylinder and sphere geometries. The FWHM tends to increase by the evolution of source curvature from converging to diverging although a minimum is visible in the FWHM curve for plane wave illumination. Besides, the effective focal length of f increases by changing the source curvature from converging to diverging.

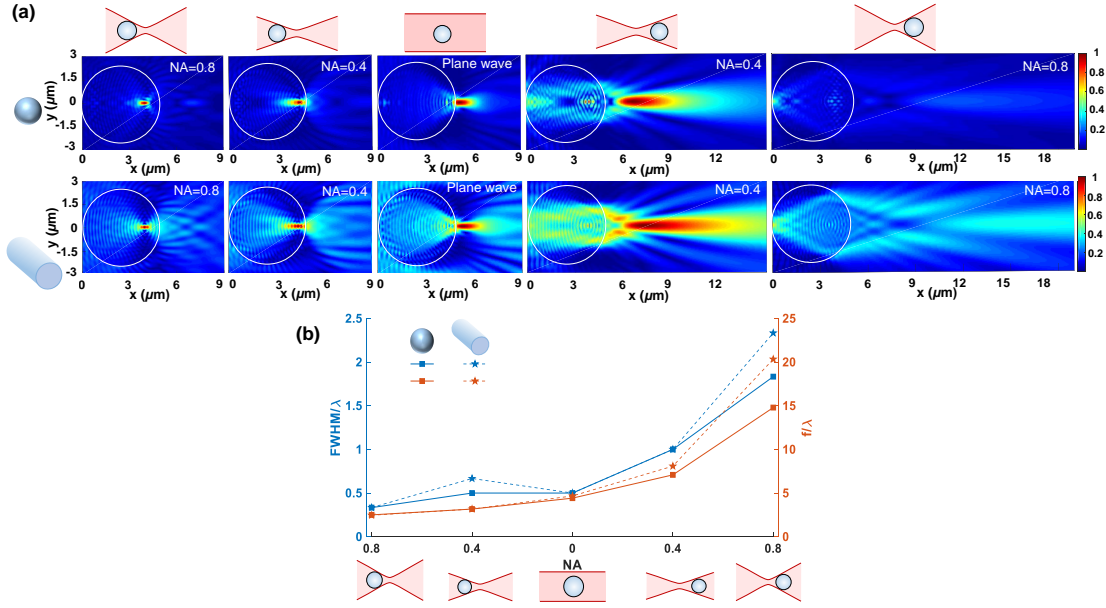


Figure 6.12: (a) Comparison between the electric field distribution of cylinder and sphere under converging, diverging sources ($NA = 0.4$ and 0.8), and plane wave illumination. The cylinder and sphere diameter is $5 \mu m$. (b) The extracted FWHM and effective focal length f of PNJs for the configurations in (a).

Here we observed similar PNJ behavior for 2D and 3D scenarios according to the diameter of microstructure for different source wave-front curvatures. It demonstrates that our theoretical findings in this paper for a 2D cylinder can be useful and informative for understanding the behavior of real 3D spheres in practical applications.

6.4 Summary

In this chapter, we systematically study the PNJ formed by a microsphere under diverging and converging sources of low and high wavefront curvatures in comparison with the plane wave illumination, by conducting the FDTD simulations. We study the characteristic parameters of PNJ including the effective focal length and FWHM. The PNJ shows a completely different behavior under converging and diverging illuminations with NA of 0.1 to 0.8 for the sphere diameters of 1.6λ to 33λ . For diverging source curvature, the PNJ is found to move along the propagation direction by increasing the source NA, forming a hot spot with a larger effective focal length and FWHM for all the sphere diameters. By further increase of NA to 0.8, PNJ is only generated for the sphere diameters of less than 16λ , and for larger diameters, the microsphere is a diffractive-refractive ball lens that collimates the beams. In contrast under the converging beam, the effective focal length and FWHM tend to decrease as a function of source NA, and for $NA > 0.2$, the PNJ is immersed inside the sphere with a FWHM that can be as small as 0.33λ . We also found similar PNJ behavior for the two configurations of (i) A glass

sphere under the converging beam, by increasing the source NA from 0.1 to 0.8, and (ii) By increasing the sphere refractive index from 1.5 to 2.5 under plane wave illumination.

Finally, our theoretical findings are especially helpful for those practical applications that implement a high NA objective to illuminate the beam for optical trapping, etc.

References

- [1] A. Heifetz, S.-C. Kong, A. V. Sahakian, A. Taflove, and V. Backman. “Photonic nanojets”. *Journal of computational and theoretical nanoscience*, 6(9):1979–1992, 2009. Publisher: American Scientific Publishers.
- [2] M.-S. Kim, T. Scharf, S. Mühlig, M. Fruhnert, C. Rockstuhl, R. Bitterli, W. Noell, R. Voelkel, and H. P. Herzig. “Refraction limit of miniaturized optical systems: a ball-lens example”. *Optics express*, 24(7):6996–7005, 2016.
- [3] Z. Wang, W. Guo, L. Li, B. Luk’yanchuk, A. Khan, Z. Liu, Z. Chen, and M. Hong. “Optical virtual imaging at 50 nm lateral resolution with a white-light nanoscope”. *Nature communications*, 2(1):1–6, 2011. Publisher: Nature Publishing Group.
- [4] H. Yang, R. Trouillon, G. Huszka, and M. A. Gijs. “Super-resolution imaging of a dielectric microsphere is governed by the waist of its photonic nanojet”. *Nano Letters*, 16(8):4862–4870, 2016. Publisher: ACS Publications.
- [5] G. Gu, J. Song, M. Chen, X. Peng, H. Liang, and J. Qu. “Single nanoparticle detection using a photonic nanojet”. *Nanoscale*, 10(29):14182–14189, 2018. Publisher: Royal Society of Chemistry.
- [6] H. Yang, M. Cornaglia, and M. A. Gijs. “Photonic nanojet array for fast detection of single nanoparticles in a flow”. *Nano letters*, 15(3):1730–1735, 2015. Publisher: ACS Publications.
- [7] H. Wang, X. Wu, and D. Shen. “Trapping and manipulating nanoparticles in photonic nanojets”. *Optics letters*, 41(7):1652–1655, 2016. Publisher: Optical Society of America.
- [8] Y. Li, H. Xin, X. Liu, Y. Zhang, H. Lei, and B. Li. “Trapping and detection of nanoparticles and cells using a parallel photonic nanojet array”. *ACS nano*, 10(6):5800–5808, 2016.
- [9] S.-C. Kong, A. Sahakian, A. Taflove, and V. Backman. “Photonic nanojet-enabled optical data storage”. *Optics express*, 16(18):13713–13719, 2008. Publisher: Optical Society of America.
- [10] B. Zhang, J. Hao, Z. Shen, H. Wu, K. Zhu, J. Xu, and J. Ding. “Ultralong photonic nanojet formed by dielectric microtoroid structure”. *Applied optics*, 57(28):8331–8337, 2018. Publisher: Optical Society of America.
- [11] Y. E. Geints, A. A. Zemlyanov, and E. K. Panina. “Microaxicon-generated photonic nanojets”. *JOSA B*, 32(8):1570–1574, 2015. Publisher: Optical Society of America.

- [12] Z. Hengyu, C. Zaichun, C. T. Chong, and H. Minghui. “Photonic jet with ultralong working distance by hemispheric shell”. *Optics Express*, 23(5):6626–6633, 2015.
- [13] L. Han, Y. Han, J. Wang, G. Gouesbet, and G. Gréhan. “Controllable and enhanced photonic jet generated by fiber combined with spheroid”. *Optics letters*, 39(6):1585–1588, 2014. Publisher: Optical Society of America.
- [14] G. Gu, J. Song, H. Liang, M. Zhao, Y. Chen, and J. Qu. “Overstepping the upper refractive index limit to form ultra-narrow photonic nanojets”. *Scientific reports*, 7(1):1–8, 2017. Publisher: Nature Publishing Group.
- [15] A. Paganini, S. Sargheini, R. Hiptmair, and C. Hafner. “Shape optimization of microlenses”. *Optics Express*, 23(10):13099–13107, 2015.
- [16] A. Darafsheh and D. Bollinger. “Systematic study of the characteristics of the photonic nanojets formed by dielectric microcylinders”. *Optics Communications*, 402:270–275, 2017. Publisher: Elsevier.
- [17] Z. Chen, A. Taflove, and V. Backman. “Photonic nanojet enhancement of backscattering of light by nanoparticles: a potential novel visible-light ultramicroscopy technique”. *Optics express*, 12(7):1214–1220, 2004. Publisher: Optical Society of America.
- [18] Y. Shen, L. V. Wang, and J.-T. Shen. “Ultralong photonic nanojet formed by a two-layer dielectric microsphere”. *Optics Letters*, 39(14):4120–4123, 2014. Publisher: Optical Society of America.
- [19] X. Mao, Y. Yang, H. Dai, D. Luo, B. Yao, and S. Yan. “Tunable photonic nanojet formed by generalized Luneburg lens”. *Optics express*, 23(20):26426–26433, 2015. Publisher: Optical Society of America.
- [20] H. Xing, W. Zhou, and Y. Wu. “Side-lobes-controlled photonic nanojet with a horizontal graded-index microcylinder”. *Optics letters*, 43(17):4292–4295, 2018. Publisher: Optical Society of America.
- [21] J. Yang, P. Twardowski, P. Gérard, Y. Duo, J. Fontaine, and S. Leclerc. “Ultra-narrow photonic nanojets through a glass cuboid embedded in a dielectric cylinder”. *Optics express*, 26(4):3723–3731, 2018.
- [22] G. Gu, L. Shao, J. Song, J. Qu, K. Zheng, X. Shen, Z. Peng, J. Hu, X. Chen, and M. Chen. “Photonic hooks from Janus microcylinders”. *Optics Express*, 27(26):37771–37780, 2019. Publisher: Optical Society of America.
- [23] L. Han, Y. Han, G. Gouesbet, J. Wang, and G. Gréhan. “Photonic jet generated by spheroidal particle with Gaussian-beam illumination”. *JOSA B*, 31(7):1476–1483, 2014. Publisher: Optical Society of America.
- [24] R. Chen, J. Lin, P. Jin, M. Cada, and Y. Ma. “Photonic nanojet beam shaping by illumination polarization engineering”. *Optics Communications*, 456:124593, 2020. Publisher: Elsevier.

-
- [25] T. Uenohara, Y. Mizutani, and Y. Takaya. “Comparison of intensity distribution of photonic nanojet according to Gaussian beam and radially polarization beam incidence”. *Precision Engineering*, 60:274–279, 2019. Publisher: Elsevier.
 - [26] M.-S. Kim, T. Scharf, S. Mühlig, C. Rockstuhl, and H. P. Herzig. “Engineering photonic nanojets”. *Optics express*, 19(11):10206–10220, 2011.
 - [27] A. Mandal and V. R. Dantham. “Photonic nanojets generated by single microspheres of various sizes illuminated by resonant and non-resonant focused Gaussian beams of different waists”. *JOSA B*, 37(4):977–986, 2020. Publisher: Optical Society of America.
 - [28] A. Dong and C. Su. “Analysis of a photonic nanojet assuming a focused incident beam instead of a plane wave”. *Journal of Optics*, 16(12):125001, 2014. Publisher: IOP Publishing.
 - [29] F. Solutions. “Lumerical solutions inc”. *Vancouver, Canada*, 2003.
 - [30] M. Mansuripur. “Distribution of light at and near the focus of high-numerical-aperture objectives”. *JOSA A*, 3(12):2086–2093, 1986. Publisher: Optical Society of America.
 - [31] F. Träger. *Springer handbook of lasers and optics*. Springer Science & Business Media, 2012.
 - [32] Y. E. Geints, A. Zemlyanov, O. Minin, and I. Minin. “Systematic study and comparison of photonic nanojets produced by dielectric microparticles in 2d-and 3d-spatial configurations”. *Journal of Optics*, 20(6):065606, 2018.

7 Structured light engineering using a photonic nanojet

7.1 Introduction

As we introduced in chapter 6, Photonic nanojet (PNJ) is a high-intensity strongly focused light beam that is generated on the shadow side surface of dielectric microparticles. Because of the flexible optical characteristics, PNJ has recently received significant attention in different fields especially in super-resolution optical imaging [1, 2], sub-wavelength direct-write nanopatterning [3], nanolithography [4, 5], nanoparticle optical trapping [6, 7], etc. For structured pattern generation, we employ micro-optical (micro-lens arrays, etc) elements under a Gaussian beam illumination, as we discussed in previous chapters. In this chapter, we introduce the structured pattern generation for a micro-lens array using the PNJ phenomenon instead of a focused Gaussian beam. Our research introduces the potential of PNJ for modifying the source and engineering its size and angular distribution in a microlens based array generator. First, we numerically report the structured pattern generation for an MLA that is illuminated by a PNJ compared to Gaussian beam illumination. We compare the PNJ for three different spheroid geometries that are illuminated by a focused Gaussian beam. Next, in the experiment part, we use our high-resolution interferometry setup that is adopted to record the field intensity and phase in different planes and compare them with simulations. Here, the lateral full width at half-maximum (FWHM) of PNJ is investigated as the main optical parameter.

7.2 Configuration

The 3D schematic of our configuration is shown in Fig. 7.1(a). An x -polarized single-mode Gaussian beam is focused on a spheroid surface, resulting in a PNJ with a high-intensity narrow peak in the shadow side. The spheroid is located at a certain distance D from a microlens array (MLA) and the field intensity distribution is observed in the far-field. The far-field is referred to the Fraunhofer region in physical optics [8]. The source wavelength is $\lambda = 642 \text{ nm}$ in all simulations and experiments. We choose $D = 1.5 \text{ mm}$ to fulfill the self-imaging condition for an MLA to obtain a high contrast pattern in the far-field [9]. More detailed discussions

on the self-imaging phenomenon for a point source illumination is explained in chapter 2. We examine the formation of PNJ for three spheroid geometries of the prolate, sphere, and oblate, as seen in the 3D schematic in Fig. 7.1(c). The sphere diameter is $10\ \mu\text{m}$, the prolate spheroid is elongated along the z -axis with the dimensions of $20\ \mu\text{m} \times 10\ \mu\text{m}$, and the oblate spheroid is flattened along the z -axis with the dimensions of $10\ \mu\text{m} \times 20\ \mu\text{m}$. The MLA has a hexagonal lattice with a period of $30\ \mu\text{m}$ and a lens radius of curvature of $47\ \mu\text{m}$, as seen in the SEM image in Fig. 7.1(b). The lens height is $2.5\ \mu\text{m}$ because of its high radius of curvature of $47\ \mu\text{m}$ for a lens diameter of around $30\ \mu\text{m}$ and for this reason, it can be considered as a thin lens. The used MLA in this experiment is the same as the one which was used in chapter 5.

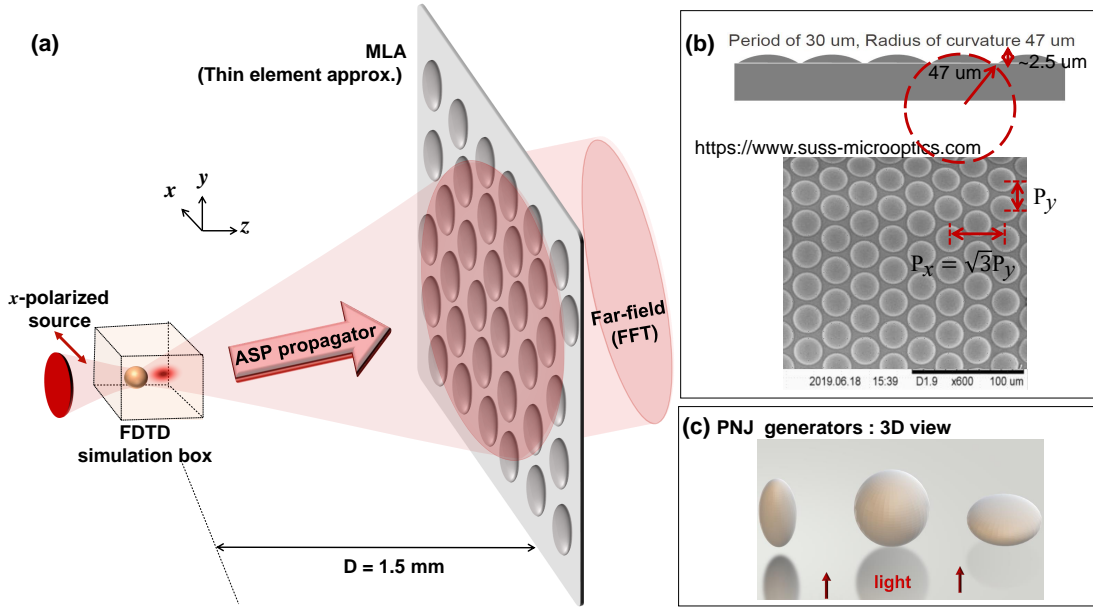


Figure 7.1: (a) The configuration under study, illuminating an x -polarized beam into a sphere at a certain distance from an MLA, (b) lens array drawing from side view and a scanning electron microscopy (SEM) image of sample from top view, (c) 3D view of the considered spheroid geometries.

7.3 Simulations

In the simulation part, as seen in Fig. 7.1(a), the source is modeled by an x -polarized single-mode Gaussian beam with a beam waist w_0 of $2\ \mu\text{m}$ that propagates along the z -axis, with the following complex field, as we earlier explained in chapter 2 :

$$u(x, y, z = 0) = \exp\left[-\frac{x^2}{w_0^2}\right] \cdot \exp(-jkz) \quad (7.1)$$

To calculate the spheroid near-field, we use the 3D rigorous FDTD solver (Lumerical FDTD[10]). The perfectly matched layer (PML) boundary condition is applied along the x , y , and z -axis in an average computational domain of $20\ \mu\text{m} \times 20\ \mu\text{m} \times 20\ \mu\text{m}$, and a uniform mesh size of

50 nm. The electromagnetic field is extracted in the plane in which the PNJ hot spot forms. The extracted field is propagated from the PNJ to the plane just immediately before MLA for a distance of $D = 1.5$ mm by applying the angular spectrum of plane waves method (ASP) [8]. The effect of physical optics by passing through the MLA is modeled by applying thin element approximation (TEA) that is valid in our case [9] and only introduces a phase delay according to the MLA surface profile. However, no amplitude modulation is added by applying this approximation. As we apply a thin MLA, the pattern field of view in the far-field does not go far beyond the paraxial approximation. For this reason, the far-field can be calculated by taking the Fourier transform of the extracted field immediately after the MLA, considering the Fraunhofer approximation [8]. The spheroid and the MLA refractive index are considered to be $n = 1.5$ and the whole configuration is in the air with a refractive index of one.

7.3.1 Gaussian Beam illumination

As reference and starting point, the field distributions at the different planes are shown for a Gaussian beam illumination (no spheroid, only Gaussian beam+MLA), in Fig. 7.2. As seen, no phase modulation is observed in P_2 which is the Gaussian beam focal plane in this example. The beam is then propagated for a distance of D , resulting in both the intensity and phase modulation in the plane of P_3 , immediately before the MLA. As we employ TEA, only the phase is modulated after passing through the MLA, however, the intensity distribution remains the same in planes P_3 and P_4 .

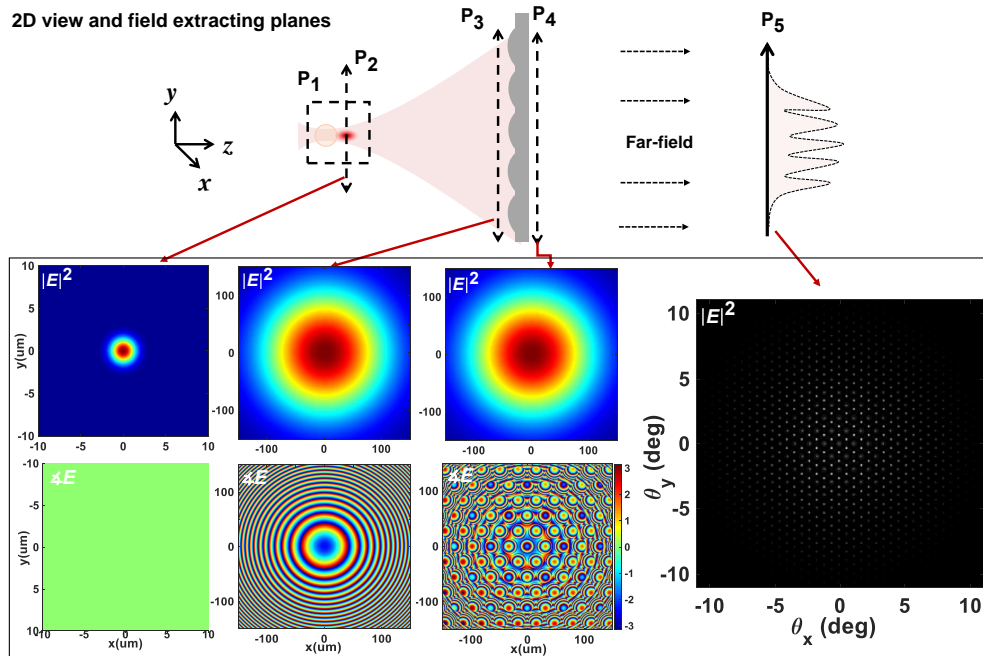
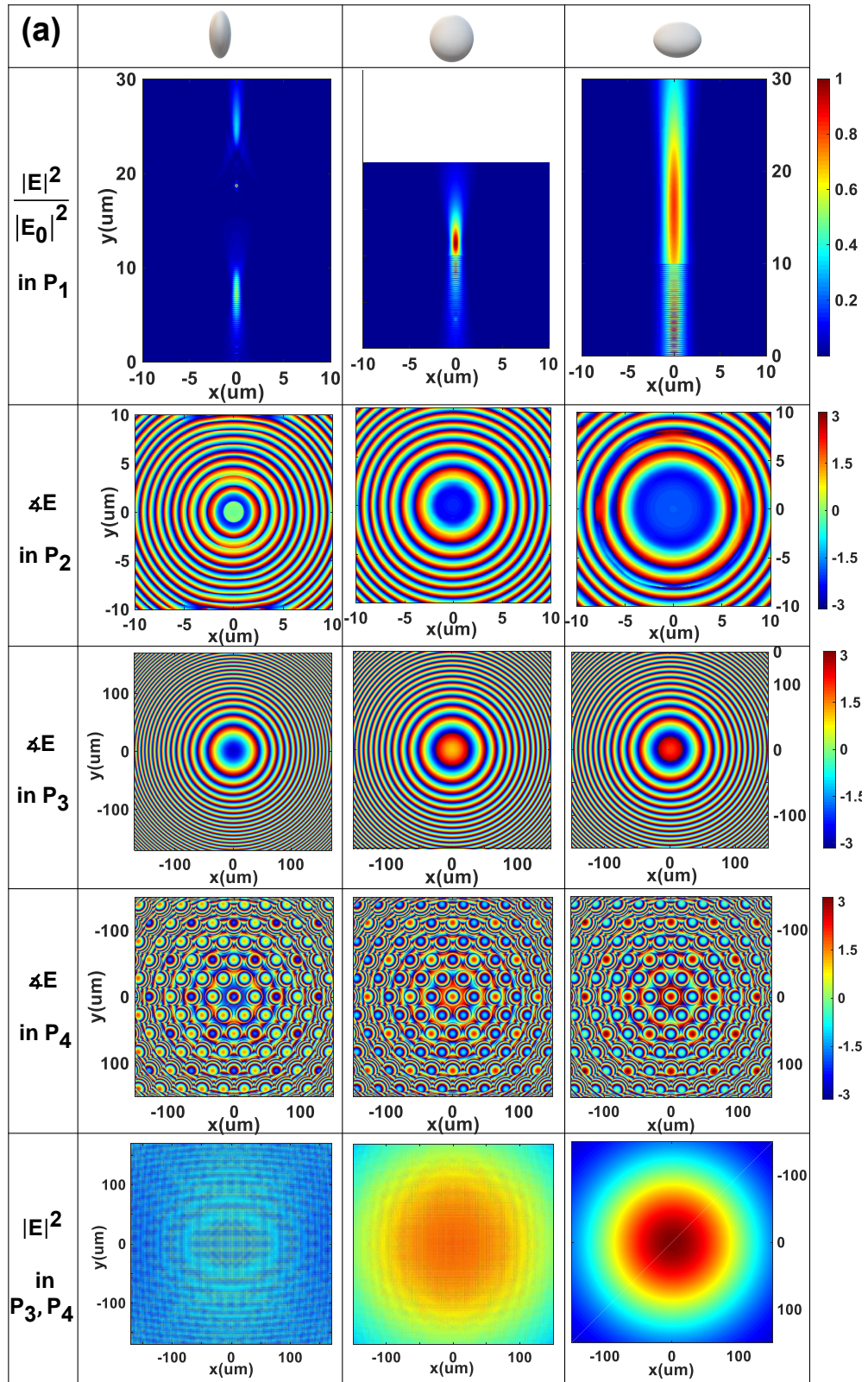


Figure 7.2: The MLA under the Gaussian beam illumination, without any spheroid in its near-field, and the extracted fields in different planes by doing simulations.

Finally, we observe a high contrast pattern of dots with a hexagonal distribution (because of the MLA hexagonal lattice) in the far-field with $+/- 8^\circ$ field of view. In a similar representation, we will theoretically and experimentally study the effect of adding a spheroid with different aspect ratios in the focal plane of the Gaussian beam. In such a situation, P_2 is referred to the plane in which the hot spot for a PNJ is formed.

7.3.2 Modulated Gaussian beam by PNJ

Figure 7.3 (a) and (b) illustrate the simulation results for the prolate, sphere, and oblate geometries. As seen from the spheroid nearfield in the plane of P_1 , a hot spot is produced for all three geometries. The transverse FWHM of PNJ is calculated to be $0.76 \mu m$ and $0.82 \mu m$, for prolate and sphere, respectively. For oblate shape, a PNJ with a larger FWHM of $1.96 \mu m$ in comparison with prolate and sphere is formed. One reason is that the oblate shape transverse diameter of $20 \mu m$ is five times larger than the incoming beam diameter of $4 \mu m$, resulting in less interference between the incoming beam and the spheroid. Besides, a PNJ with a larger transverse FWHM and effective focal length is formed by going from a prolate to oblate geometry [11]. From the phase distribution in the PNJ focal plane of P_2 , one observes that: First, the phase is modulated in the focal plane of PNJ for all the spheroid geometries while for a Gaussian beam, no phase modulation is observed at its focal plane, as seen in Fig. 7.2. Second, the smaller the transverse FWHM, the larger the phase modulations in the focus plane; i.e. that a PNJ with a higher divergence angle is produced for prolate and sphere in comparison with the oblate geometry. It also leads to different phase distributions for these configurations, in the following plane of P_3 immediately before the MLA. Furthermore, the phase distribution in the plane of P_4 immediately after the MLA is modulated according to the MLA geometry. The field intensity distribution in the plane of P_3 and P_4 immediately before and after the MLA is the same as we implement TEA for modeling the diffraction from MLA, the approximation in which no amplitude modulation is assumed. More importantly, the field intensity in the plane of P_3 and P_4 is distributed in a larger area for prolate and sphere compared to oblate shape; confirming the higher divergence angle of PNJ for prolate and sphere.



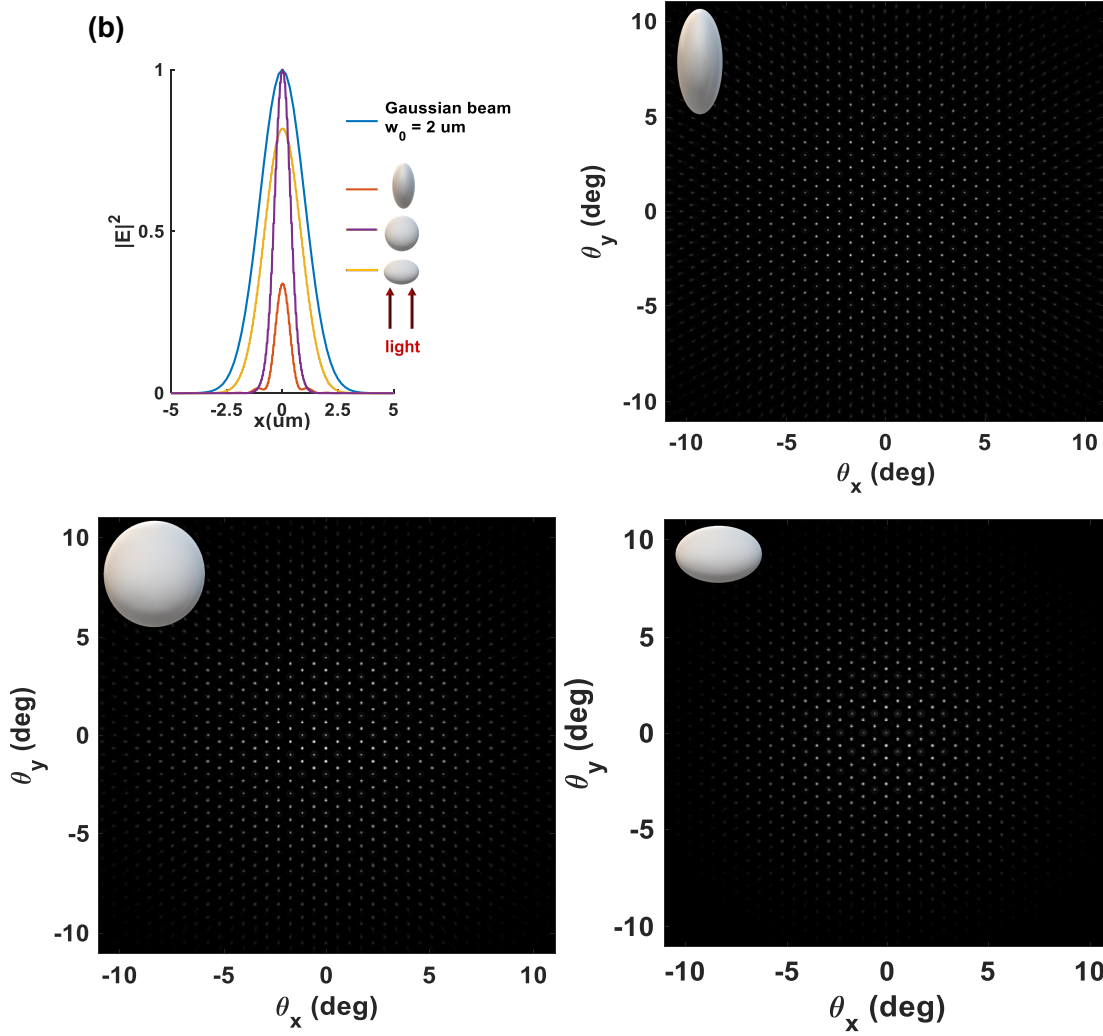


Figure 7.3: (a) Field distribution in the planes of P_1 to P_4 for oblate, sphere and prolate geometries, by doing simulations, (b) The PNJ Intensity cross section and their corresponding far-field distributions.

Figure 7.3(b) demonstrates the transverse intensity profiles at the PNJ plane and their corresponding far-field distributions. As seen, the far-field pattern is distributed in a larger area for sphere and prolate in comparison with oblates shape; meaning that the pattern FOV is higher. It is originated from the PNJ optical characteristics. The smaller the transverse FWHM, the larger the source divergence angle, and the larger the number of lenses that are covered by the incoming beam, resulting in a higher field of view in the far-field distribution [9].

7.4 Experiments

In the experimental evaluation, we aim to extract the full information of the field including intensity and phase. We use our high-resolution interference microscopy system to extract both field intensity and phase in different planes of P_1 to P_5 . The schematic of setup is shown in Fig. 7.4. We use configuration 2 for the case in which the Gaussian beam is modulated by a spheroid. For Gaussian beam illumination with no spheroid in its near-field, configuration 2 is replaced by configuration 1 that is shown in the inset figure of 7.4. The working principle and step by step field recording in plane P_1 to P_5 , is explicitly explained in chapter 4. Furthermore,

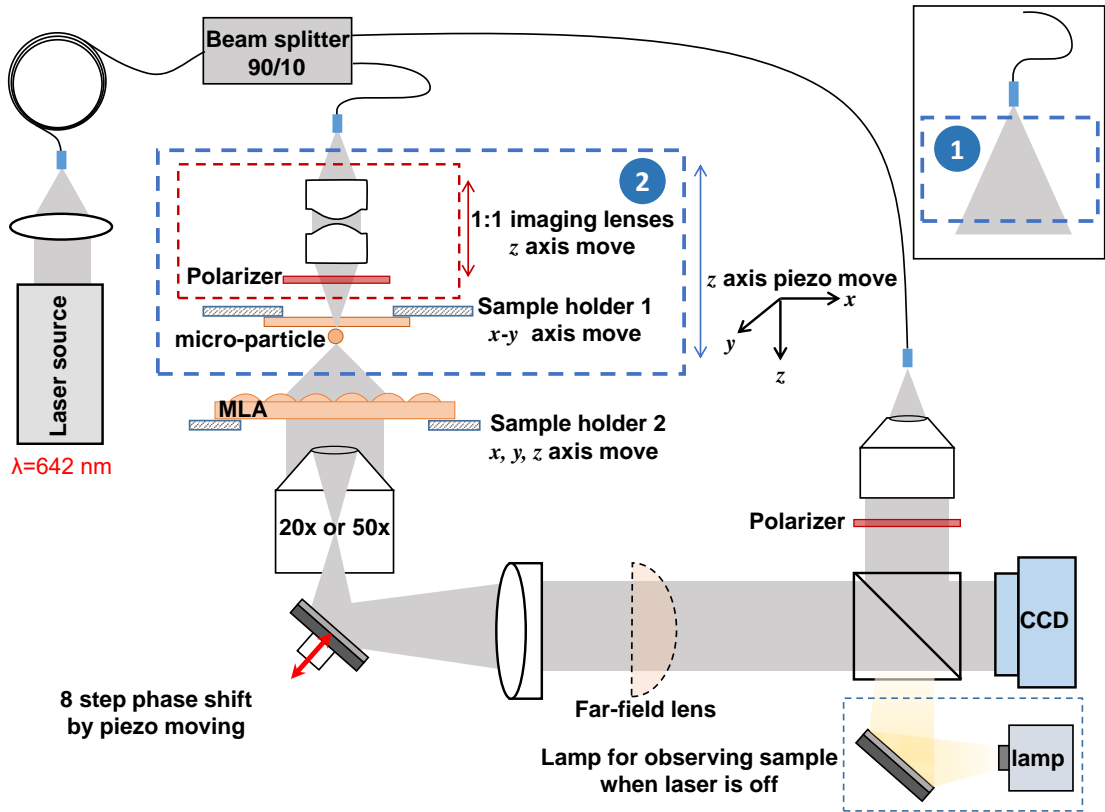


Figure 7.4: The schematic of high-resolution interference microscopy setup (HRIM) which is based on a Mach-Zehnder interferometer. Configuration 2 is replaced by configuration 1 considering Gaussian beam illumination, without any spheroid in its near-field.

the spheroid samples are fabricated through a direct laser writing technique by making use of the commercial Nanoscribe Photonic Professional GT which is a femtosecond laser lithography system [12]. A few drops of IP-Dip liquid resist is dispensed on a glass wafer. Then the objective focuses on different planes to polymerize the resist with an axial and lateral resolution of 100 nm . After polymerization, the sample is developed and the non-polymerized resist removes. The polymerized IP-DIP refractive index is 1.52.

7.4.1 Gaussian beam illumination

The measured field distributions at the different planes are shown for a Gaussian beam illumination (no spheroid, only Gaussian beam+MLA), in Fig. 7.5. As seen, the source intensity distribution is very similar to a Gaussian beam illumination with $w_0 = 2\mu m$ except that the field distribution is not perfectly symmetric. The beam is then propagated for a distance of D , resulting in both the intensity and phase modulation in the plane of P_3 , immediately before the MLA. As seen from intensity distribution in the plane immediately after the MLA, a limited number of lenses are covered by the beam. This results in a far-field distribution with a lower field of view and contrast (especially in the center of the pattern) compared to adding a spheroid in the system. This effect will be investigated for different spheroid geometries in the following section.

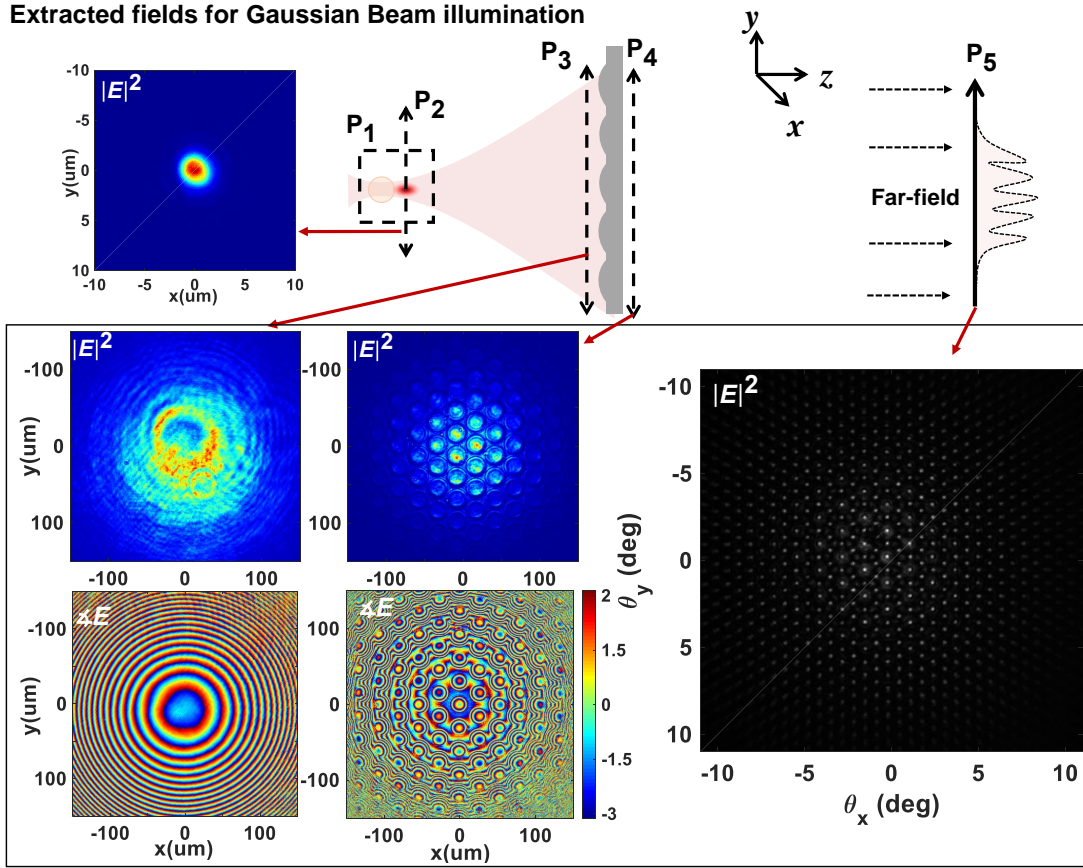
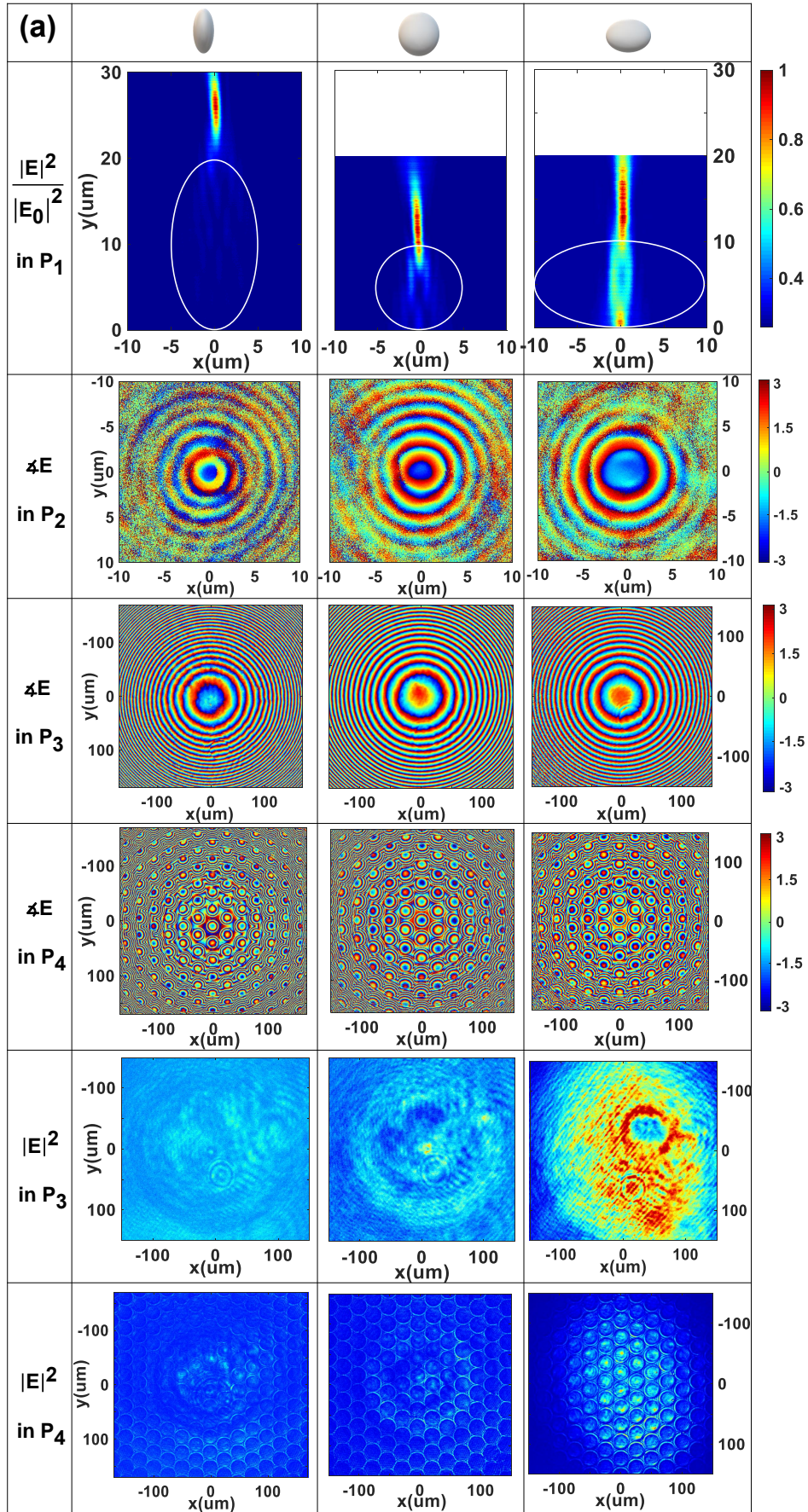


Figure 7.5: The MLA under the Gaussian beam illumination, without any spheroid in its near-field, and the extracted fields in different planes by doing experiments.

7.4.2 Modulated Gaussian beam by PNJ

Figure 7.6 illustrates the experimental results for comparison with performed simulations. From the recorded near-field in the plane of P_1 , it can be observed that a PNJ with a smaller transverse FWHM is formed for prolate and sphere in comparison with oblate shape. The transverse FWHM is measured to be $0.8 \mu m$, $0.82 \mu m$, and $1.06 \mu m$ for prolate, sphere, and oblate, respectively. As seen in P_2 , the phase distribution in the focal plane of PNJ confirms that for smaller FWHM, more modulations are observed in the phase distribution that is analogous to a source with a higher divergence angle. However, the phase measurement in this plane is extremely challenging because the fields are mostly concentrated in the focus of PNJ and, the intensity level in the edges is very low to interfere with the incoming beam from the reference arm. For this reason, the phase distribution in outer rings is noisy. As seen, the phase distribution in P_3 and P_4 , immediately before and after the MLA are recorded. In the plane of P_4 immediately after the MLA, the phase distribution is modulated due to the effect of diffraction from MLA. Also, the field intensity distribution is measured in P_3 and P_4 immediately before and after the MLA. As we also observed in the simulation results, the field intensity in P_3 immediately before the MLA is distributed in a larger area for prolate and sphere in comparison with oblate geometry. The intensity distribution in P_4 immediately after the MLA is weekly modulated because of the diffraction from the thin MLA. This modulation was not observed in simulation results because the TEA was employed for modeling the MLA. Figure 7.6(b) shows the transverse intensity profiles at PNJ plane and their corresponding far-field distributions. As seen, the far-field pattern is distributed in a larger area, having a higher FOV for sphere and prolate in comparison with oblates shape. For a smaller FWHM of the PNJ a higher divergence angle is introduced that results in a higher FOV in the far-field pattern for prolate and sphere geometries.

The simulation and experimental results are in good agreement although, two aspects should be considered while comparing them. First, underneath the fabricated spheroid where the structure joins the substrate is not perfectly curved because the spheroid should have flat support to attach the glass substrate [13, 14]. This effect can be more pronounced for prolate because of its high curvature in the area in which the structure is attached to the substrate. Second, the intensity is recorded by focusing the objective in different planes including the planes inside the spheroid. By focusing the objective, the interference effect inside the particle due to the material refractive index is not fully considered.



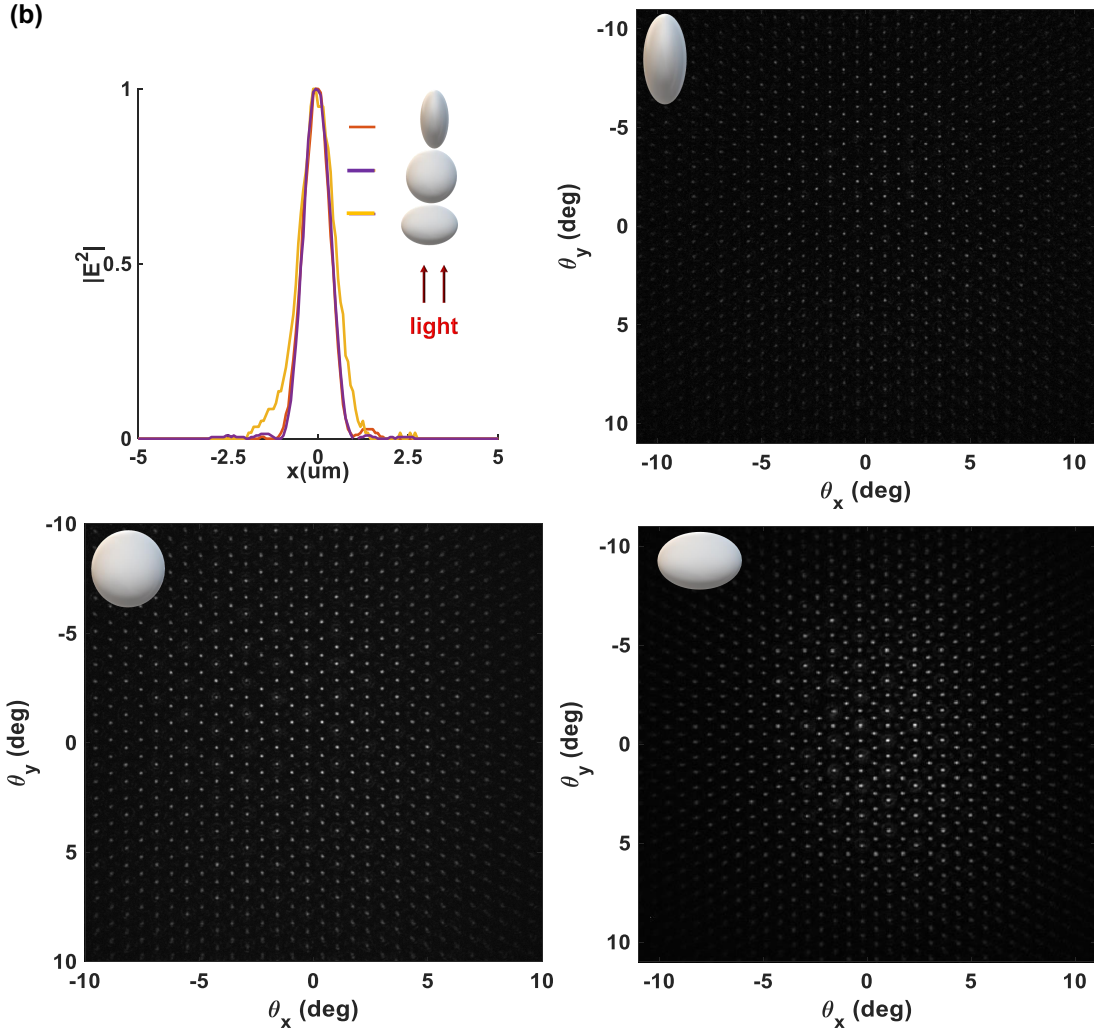


Figure 7.6: (a) Field distribution recorded in the planes of P_1 to P_4 for oblate, sphere and prolate geometries, using the high-resolution interferometry setup, (b) The PNJ Intensity cross section and their corresponding far-field distributions.

7.5 Comparison between simulations and experiments

For a thorough study, we do a comparison between the far-field distributions, quantitatively. We calculate the number of points in the far-field pattern considering only dots intensities higher than 13% of the maximum intensity in each pattern. Figure 7.7 compares the simulated and experimentally measured transverse FWHM for each configuration and the corresponding number of points (N. of points) in the far-field pattern. As seen for both experiments and simulations, a larger number of points in the far-field pattern is realized for sphere and prolate with a smaller transverse FWHM in comparison with oblate shape. The experimental and simulation results match very well. However, the deviation between the experimentally measured and simulated FWHM is higher than other configurations for oblate geometry. For

this geometry, both the measured and simulated FWHM are large values and for a large FWHM, the deviation in source divergence angle is small between these two cases. For this reason, the experimentally and numerically obtained number of points in the patterns are almost equal for this configuration.

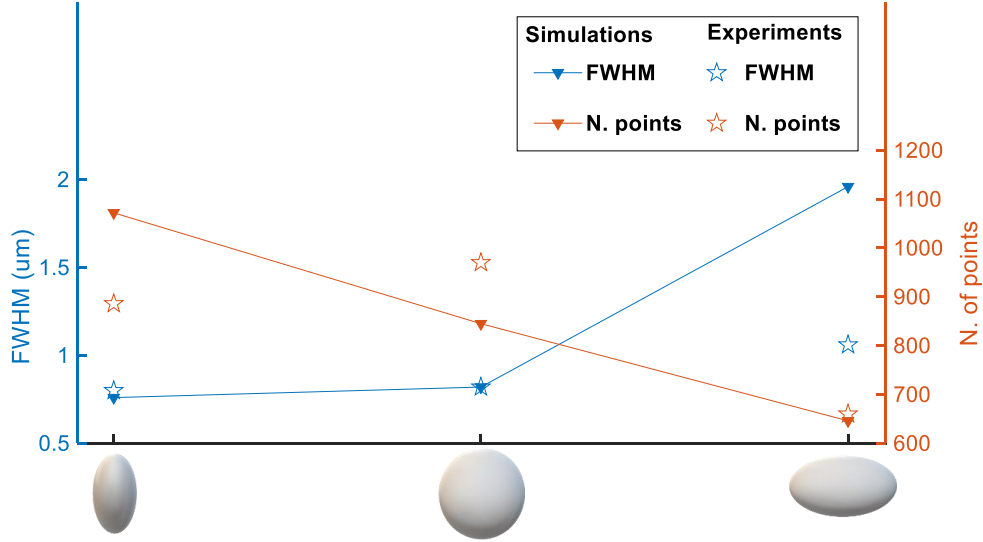


Figure 7.7: Numerically and experimentally calculated FWHM and the number of points (N. of points) in the far-field pattern.

7.6 Summary

In summary, we introduce the PNJ as a source manipulator in a structured pattern generation system. The structured light generator is a microlens array under a diverging source. By introducing a spheroid in the focal point of the source, the source near-field is modulated, producing a PNJ that affects the far-field pattern. We developed a high-resolution interferometry setup to record both the phase and intensity in different planes for a deeper comparison with simulations. The simulation and experimental results demonstrate that the number of points in the far-field pattern can be engineered by the optical characteristics of PNJ including the FWHM and divergence. We examine the oblate, sphere, and prolate geometries and demonstrate that for a smaller FWHM, a source with a higher divergence angle is realized that leads to a far-field pattern with a larger field of view.

References

- [1] H. Yang, R. Trouillon, G. Huszka, and M. A. Gijs. “Super-resolution imaging of a dielectric microsphere is governed by the waist of its photonic nanojet”. *Nano Letters*, 16(8):4862–4870, 2016. Publisher: ACS Publications.

-
- [2] Z. Wang, W. Guo, L. Li, B. Luk'yanchuk, A. Khan, Z. Liu, Z. Chen, and M. Hong. "Optical virtual imaging at 50 nm lateral resolution with a white-light nanoscope". *Nature communications*, 2(1):1–6, 2011.
 - [3] E. Mcleod and C. B. Arnold. "Subwavelength direct-write nanopatterning using optically trapped microspheres". *Nature nanotechnology*, 3(7):413–417, 2008.
 - [4] J. Kim, K. Cho, I. Kim, W. M. Kim, T. S. Lee, and K.-S. Lee. "Fabrication of plasmonic nanodiscs by photonic nanojet lithography". *Applied Physics Express*, 5(2):025201, 2012.
 - [5] A. Jacassi, F. Tantussi, M. Dipalo, C. Biagini, N. Maccaferri, A. Bozzola, and F. De Angelis. "Scanning probe photonic nanojet lithography". *ACS applied materials & interfaces*, 9(37):32386–32393, 2017.
 - [6] H. Wang, X. Wu, and D. Shen. "Trapping and manipulating nanoparticles in photonic nanojets". *Optics letters*, 41(7):1652–1655, 2016. Publisher: Optical Society of America.
 - [7] Y. Li, H. Xin, X. Liu, Y. Zhang, H. Lei, and B. Li. "Trapping and detection of nanoparticles and cells using a parallel photonic nanojet array". *ACS nano*, 10(6):5800–5808, 2016.
 - [8] J. W. Goodman. *Introduction to Fourier optics*. Roberts and Company Publishers, 2005.
 - [9] M. Yousefi, T. Scharf, and M. Rossi. "Dot pattern generation using thick sinusoidal phase grating under gaussian beam illumination". In *Digital Optical Technologies 2019*, volume 11062, page 1106211. International Society for Optics and Photonics, 2019.
 - [10] F. Solutions. "Lumerical solutions inc". *Vancouver, Canada*, 2003.
 - [11] L. Han, Y. Han, J. Wang, G. Gouesbet, and G. Gréhan. "Controllable and enhanced photonic jet generated by fiber combined with spheroid". *Optics Letters*, 39(6):1585–1588, 2014.
 - [12] B. H. Cumpston, S. P. Ananthavel, S. Barlow, D. L. Dyer, J. E. Ehrlich, L. L. Erskine, A. A. Heikal, S. M. Kuebler, I.-Y. S. Lee, D. McCord-Maughon, et al. "Two-photon polymerization initiators for three-dimensional optical data storage and microfabrication". *Nature*, 398(6722):51–54, 1999.
 - [13] A. Bogucki, . Zinkiewicz, M. Grzeszczyk, W. Pacuski, K. Nogajewski, T. Kazimierczuk, A. Rodek, J. Suffczynski, K. Watanabe, T. Taniguchi, et al. "Ultra-long-working-distance spectroscopy of single nanostructures with aspherical solid immersion microlenses". *Light: Science & Applications*, 9(1):1–11, 2020.
 - [14] M. Rank and A. Heinrich. *3D printing of optics*. 2018.

8 Structured light engineering for photonic nanojets as multi-sources

8.1 Introduction

In previous chapters, we studied pattern generation for a single source. Using multi-sources, the pattern in the far-field may be redistributed, depending on the sources' optical characteristics such as coherence. If the sources non-coherently illuminate, the field intensity in the observation plane is simply the sum of the sources intensities as their fields do not interfere with each other. For coherently illuminating sources, the fields do interfere with each other and the problem becomes more complicated. In this chapter, we study using coherently illuminating multi-sources where the sources are PNJs. The purpose is to apply different arrangements of PNJs in the Gaussian source near-field and observe the resulting distribution of dots in the far-field. Our idea is to image the multi-sources near-field distribution in the far-field observation plane, depending on the geometry that is used in the near-field.

8.2 Simulations

The schematic of our configuration is shown in Fig. 8.1. The x -polarized single-mode Gaussian beam with the beam waist $w_0 = 2\mu m$, illuminates a microstructure, resulting in an array of PNJs with high-intensity narrow peaks in the shadow side. The microstructure is at a certain distance d from the Gaussian beam focal plane, depending on its size and geometry. In this way, the microstructure is fully covered by the incoming beam. The microstructure is located at a certain distance D from a microlens array (MLA) and the field intensity distribution is observed in the far-field. The source wavelength is $\lambda = 642nm$ and we use a square lattice MLA with a period of $50\mu m$ along x and y axis. We choose D to be $3.9mm$ to fulfill the self-imaging condition for this MLA to obtain a high contrast pattern in the far-field.

As it is seen in Fig. 8.1, the used simulation tools are the same as chapter 7. To calculate the micro-structure near-field, the 3D rigorous FDTD solver (Lumerical FDTD[1]) is used. The electromagnetic field is extracted in the near-field plane and propagated for a distance of $D = 3.9mm$ by applying the angular spectrum of plane waves method (ASP)[2]. The effect of beam

propagation through the MLA is modeled by applying thin element approximation (TEA). The far-field is then calculated by taking the Fourier transform of the extracted field immediately after the MLA.

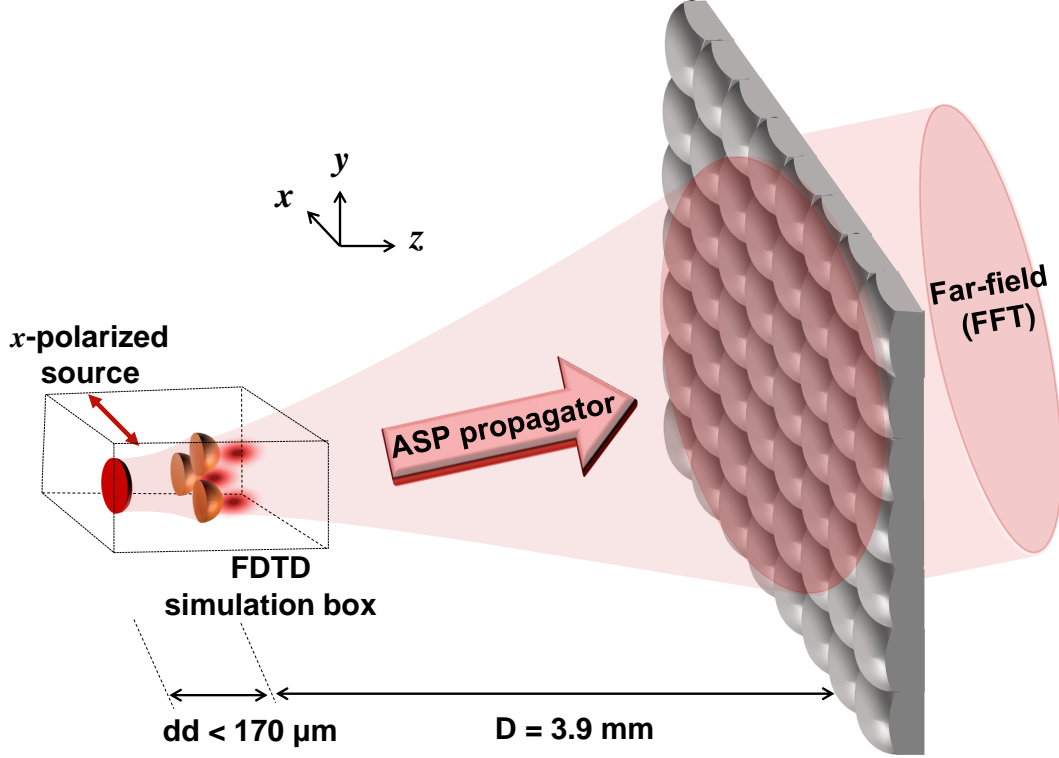


Figure 8.1: The configuration under study for a multi-source scenario. Micro-structures are inserted in the source near-field.

We perform the simulations for two example configurations, as it is shown in Fig. 8.2. In the first configuration, three half-spheres having apertures in a triangular arrangement is assumed. As seen in Fig. 8.2(a), the near field in the focal plane shows three PNJs that are generated in a triangular arrangement. The near-field triangular arrangement is imaged in each period of far-field pattern, as it is seen in the far-field distribution. In Fig. 8.2(b), the simulations are done for four half-spheres that are arranged in square lattices and four PNJs are produced in the near-field focal plane of microstructure. The square arrangement of PNJs, are reproduced in each period of far-field pattern, as seen in the far-field distribution. The simulation results show that the PNJs near-field is imaged in the far-field observation plane and in this way, different distributions of dots are generated in the far-field. Although, the far-field distribution resolution is poor as the high-resolution 3D simulation is computationally extensive for these configurations.

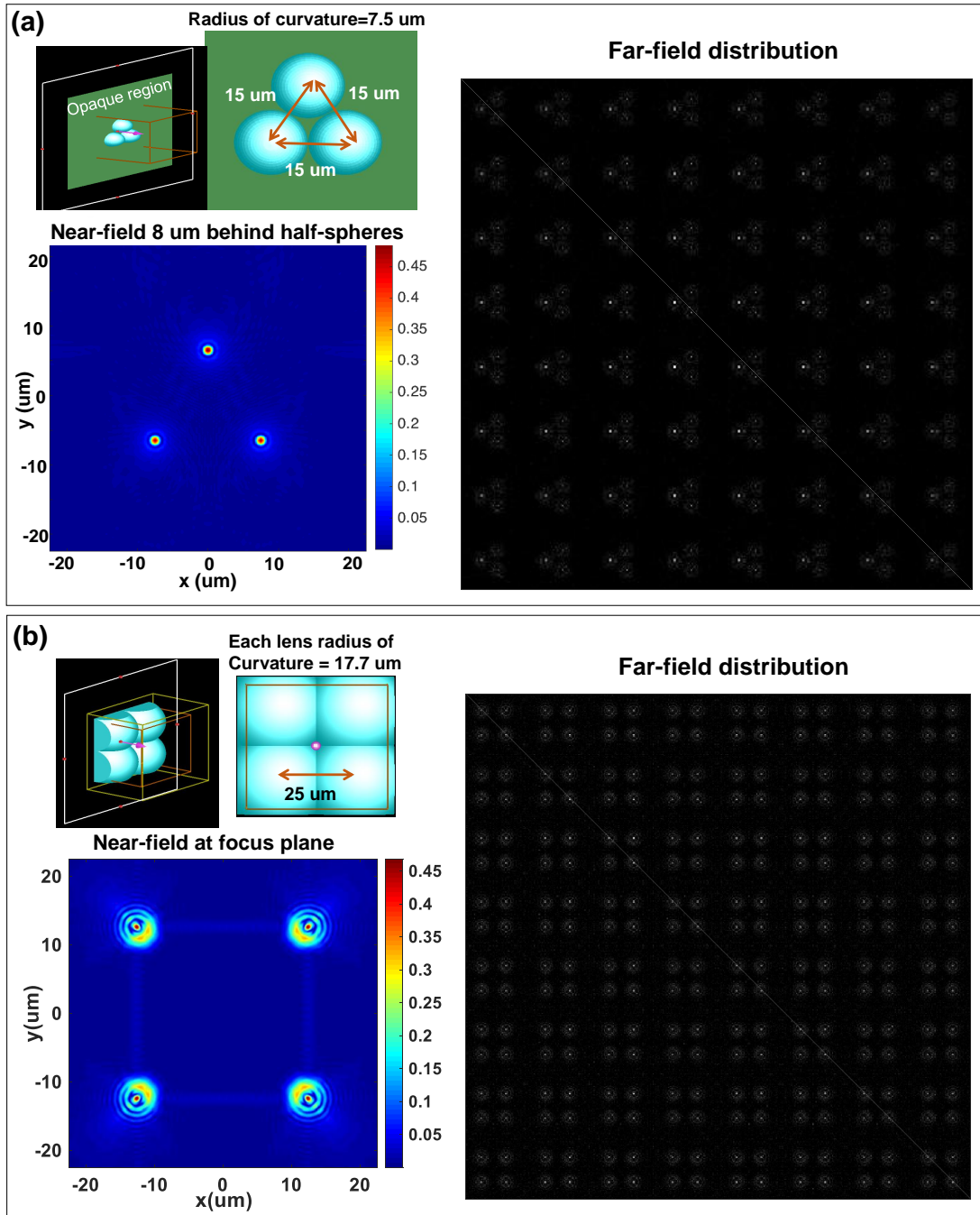


Figure 8.2: (a) The triangular arrangement of half-spheres with apertures, the near-field in its focal plane, and the far-field distribution, (b) The square arrangement of half-spheres with square lattice shape, the near-field in the focal plane, and the resulting far-field distribution.

8.3 Experiments

In the experiment section, we examine five microstructure arrangements. The samples are fabricated using the 3D printing technique, employing the Nanoscribe Photonic Professional GT. The MLA is retained by a rotating sample holder. Three far-field distributions are recorded for each microstructure by rotating the MLA plane with respect to the microstructure plane for the rotation angles of $\theta = 0^\circ$, 30° and 45° . A three dimensional schematic of configurations and the recorded near-field and far-fields are shown in Fig. 8.3. As it is seen for the square, triangular and hexagonal arrangements of the half-spheres in figures 8.3(a) to (d), the near-field at PNJ plane is imaged in every period of the far-field distribution. By rotating the MLA with respect to the half-spheres plane, different arrangements of dots can be achieved in the far-field. For the configuration in Fig. 8.3(a), for 45° rotation angle, the far-field distribution is not simply the image of rotated near-field at PNJ plane but it is a distribution of points in a square grid with less number of dots compared to 0° rotation angle. For the configurations in Fig. 8.3(b) to (d), the rotated near-field is imaged in each period of far-field for all the rotation angles. For the configuration in Fig. 8.3(e), the structure is divided into square and rectangular units, each of the two lenses in square units having a different focal distance. As a result, this configuration is composed of sources with different optical characteristics. The near-field in f_1 and f_2 focal planes of the two lenses having the square lattices are recorded. As seen, for the small square unit, a high-intensity PNJ is produced in the near-field focal plane f_2 . This results in a grid of high-intensity points in the far-field pattern. On the other side, for the larger square unit, the intensity in its focal plane is lower and generates a grid of low-intensity points in the far-field observation plane.

The samples are fabricated on a glass substrate without any apertures that can block the incoming beam around the structure. It is tricky to focus the source on the sample plane such that it covers the whole structure but does not transmit through the glass substrate around the sample. For this reason, the contrast of the pattern in the far-field may reduce, especially this effect is well visible for the triangular configuration in the far-field pattern in Fig. 8.3(b). Besides, because of the non-uniform intensity distribution of Gaussian source compared to plane wave illumination, the intensity over PNJs is not the same, for example for the hexagonal arrangement in Fig. 8.3(c), the PNJ in the center has a higher intensity compared to the neighboring PNJs. This effect directly results in low and high intensity peaks in the far-field.

8.4 Summary

In this chapter, we studied an MLA under coherently illuminating PNJs to engineer the field distribution in the far-field. Different distributions of dots in the far-field is realized by designing the PNJs arrangement in near-field, applying different configurations of micro-structures in the source near-field. By rotating the MLA plane with respect to the PNJs plane, we can redistribute the dots and generate different patterns in the far-field observation plane.

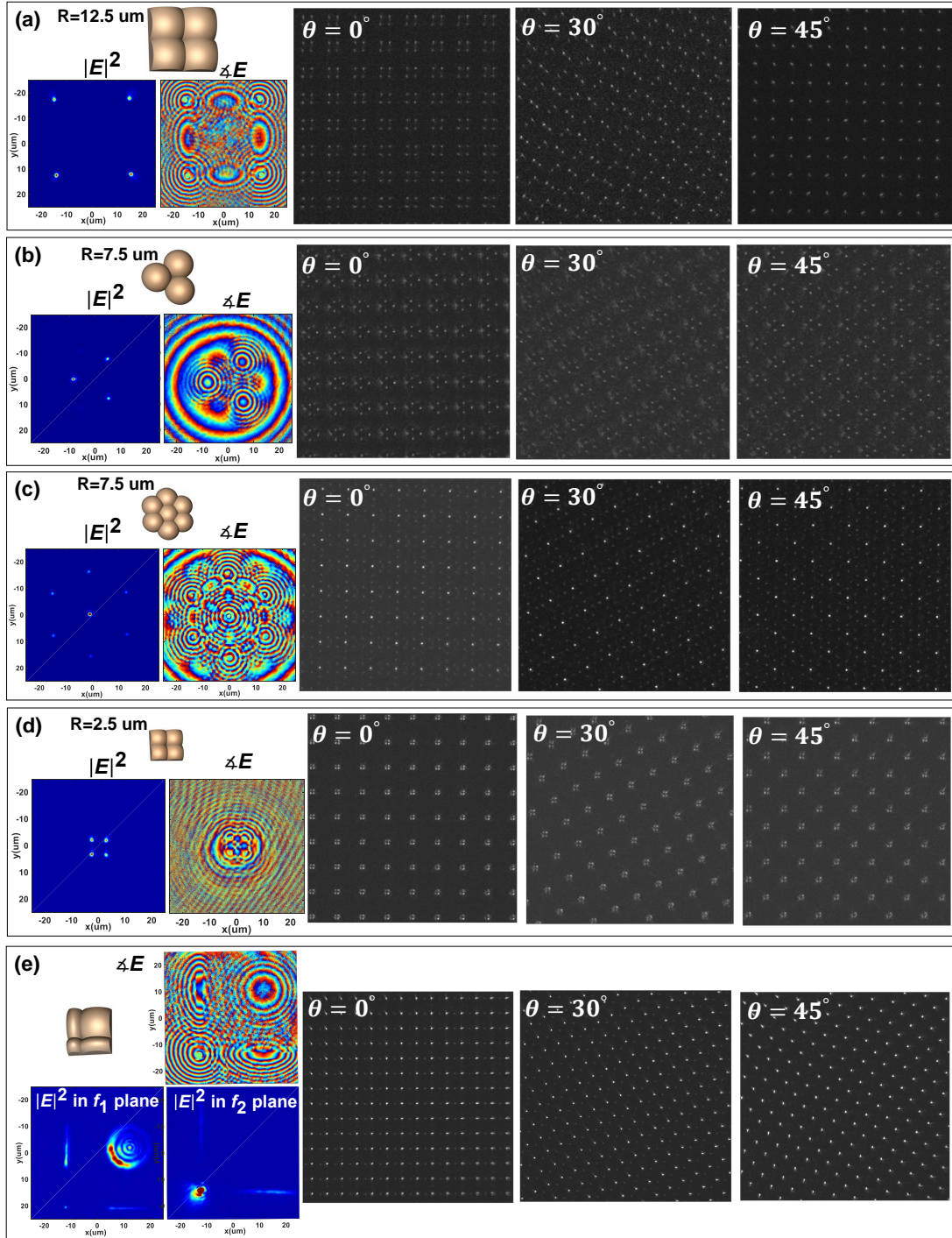


Figure 8.3: Different micro-structure geometries for modulating the source near-field. Experimentally calculated near-field distribution at the micro-structures focal plane and the corresponding far-field patterns for rotation angles of $\theta = 0^\circ$, 30° and 45° between the MLA plane and the micro-structure plane are demonstrated.

References

- [1] F. Solutions. “Lumerical solutions inc”. *Vancouver, Canada*, 2003.
- [2] J. W. Goodman. *Introduction to Fourier optics*. Roberts and Company Publishers, 2005.

9 Summary and outlook

In this thesis, we studied the structured light generation, using periodic microoptical elements in the refraction-diffraction regime, under a focused diverging source instead of a plane wave. A high-contrast far-field distribution is generated for specific values of the distance between the source and optical element, according to the Lau effect. Considering this phenomenon, we obtained a high-contrast structured light distribution. We chose two strategies; modification of periodic microoptical element surface profile and source modulation by applying an optical element in its near-field:

In the first strategy, we applied a sinusoidal phase grating instead of a regular lens array under Gaussian beam illumination to enhance the number of points in the far-field observation plane. The sinusoidal curvature is a combination of convex and concave curvatures, resulting in more points in the observation plane compared to the lens array. By changing the sinusoidal phase grating thickness from thin to thick, different distribution of points with different uniformities is realized in the far-field. The sinusoidal phase gratings were fabricated using two-photon absorption polymerization technique and the experimentally recorded far-field distributions were compared with the simulations. Finally, in a more general configuration, we considered a concave and convex lens in each period of the optical element instead of a sinusoidal profile; we optimized the lens curvature to further increase the field of view compared to sinusoidal shape. By surface optimization, we concluded that the pattern FOV and the number of points can even further increase to large values. The state of art point generators, have a large field of view of $71^\circ \times 51^\circ$ (considering the Full width at half maximum definition) and 6k number of points that can approach 8k. However, with optimized curvature in our strategy, we can generate 14.5 k points with large FOV of $77^\circ \times 77^\circ$. This part of the thesis demonstrates that by properly defining the refractive-diffractive microoptical element surface profile, we can achieve even more points in far-field compared to the arbitrary used optical elements such as lens arrays.

In the next part, we studied structured light generation by modifying the source near-field. Applying a dielectric microstructure in the source near-field, an alternative source with a new optical characteristic is generated. Adding a dielectric microparticle in the source near-

field, a hot spot i.e a photonic nanojet (PNJ) is generated in the shadow side surface of the structure that is a new alternative source in the system to redistribute the dots in the far-field. We numerically demonstrated that the PNJ optical characteristics change with respect to microsphere diameter for diverging and converging sources of low and high wavefront curvatures. Using this strategy to modify the source near-field, we were able to improve the structured light generation in the far-field. We demonstrated that by applying the dielectric microparticle in the source focal plane, a PNJ is generated that corresponds to a high NA source in the point generator system. This high NA source enlarges the far-field distribution FOV. In this strategy, the pattern distribution and its period do not change and only the FOV is increased. In this part, we used a thin lens array generating a low FOV pattern to qualitatively observe the effect of inserting a microparticle in the source near-field on far-field distribution.

To experimentally evaluate this idea, we used a high-resolution interference microscopy (HRIM) setup. Our interferometry setup is developed based on a Mach-Zehnder interferometer in which we can record both phase and amplitude in different planes. We recorded the fields under both Gaussian beam and plane wave illumination. We experimentally studied the far-field generation for a microlens array under a Gaussian beam by applying a microparticle in its near-field. As we expected from our numerical results, by applying the microparticle in the source near-field, a PNJ is formed that corresponds to a high NA source. In this way, the pattern FOV increases in the far-field. We extracted the phase and amplitude in different planes for a deeper understanding and comparison with simulations. In this strategy, the distribution of points remains the same, however the FOV increases.

Next, to increase both the FOV and density of point distribution in the observation plane, we applied multiple coherently illuminating PNJs instead of a single microparticle in the source near-field. As an example, by applying four lenses with square lattice in the source near-field, four points in each period of far-field distribution are generated instead of one. In this way, we were able to reach more than 24k points which is a comparable number with the number of generated points in the iPhone (30k). With this strategy, we can further increase the number of points by creatively designing more lenses in the source near-field; for example with a hexagonal arrangement of lenses, the number of points can exceed 40k.

According to this summary, our introduced strategies are promising in the field of structured light generation and there is room to further advance this research. For industrial applications, a vertical-cavity surface-emitting laser (VCSEL) is implemented instead of the Gaussian beam illumination. The VCSEL is a kind of semiconductor laser diode in which the beam emits perpendicularly from its top surface. One interesting project is to study the generation of PNJ under a VCSEL source. For this purpose, the fabrication of a lens or multi-lenses on a VCSEL source can be studied and designed to generate a desirable source with new optical characteristics.

The study of meta-lens which is a diffractive flat lens is a hot topic in academic environments. In my view, there is this potential to apply metalens especially the dielectric ones in the

industry. We can study using dielectric meta-lens instead of microparticles to modulate the source near-field. To do so, the fabrication of meta-lens on a VCSEL can be investigated; the topic that is been recently attracted by researches and some experimental results has been published in this field. Applying meta-lens, there is the possibility to have a more compact module for industrial applications however, proper fabrication tools are required to be used for mass production in the industry.

In this thesis, we used the high-resolution interference microscopy system and applied the PSI algorithm to record the phase. Studying and comparing different types of algorithms to extract the phase is a broad field of study. With a more detailed comparison between different algorithms, one can investigate the further improvement of phase extraction in the system.

In the last part of the thesis, we studied coherently illuminating multi-sources instead of a single source. As we discussed, the near-field of the multi-source is directly imaged in each period of pattern distribution in the far-field. We have studied this phenomenon for a small dimension of multi-sources that is less than the lens array period. One can study the self-imaging phenomenon for larger dimensions and arrangement of the structures in the source near-field and find the limitations of self-imaging versus dimensions of the structure.

Maryam Yousefi

CONTACT INFORMATION	<p>Nanophotonics and Metrology Laboratory (NAM)</p> <p>EPFL-STI-IMT-NAM Station 11 CH-1015 Lausanne</p> <p>Phone : +41 787324937 Email : maryam.yousefi@epfl.ch web: people.epfl.ch/maryam.yousefi</p>
EDUCATION	<p>Ph.D in Optics and Photonics</p> <ul style="list-style-type: none">Ecole Polytechnique Federal de Lausanne, Lausanne, Switzerland March 2017-Dec. 2017 And July 2019-presentAMS AG., Ruschlikon, Zurich area, Switzerland Jan. 2018- Jun. 2019 <p>Thesis: Structured light generation by refractive-diffractive micro optical array illuminators Advisor: Dr. Toralf Scharf</p> <p>Master in Electrical Engineering (Fields and waves)</p> <p>Shiraz University, Shiraz, Iran, Sept. 2012 – Feb. 2015 Thesis: Improvement of Light Absorption in Photovoltaic Solar Cells using Plasmonic Structures Advisor: Prof. Abbas Alighanbari</p> <p>Bachelor in Electrical Engineering (Electronics)</p> <p>Shiraz University of Technology, Shiraz, Iran, Sept. 2007 – July. 2012 Thesis: Optimum Gene Selection via Meta-heuristic Methods to Improve Clustering systems Advisor: Prof. Aliakbar Rahideh</p>
SCIENTIFIC CONTRIBUTIONS	<p>I have obtained a solid background in optics with the emphasis on 'optical design for structured light generation' to find innovative solutions for problems especially according to the industry needs and constraints. Thanks to my experience of staying in the industry during my Ph.D and with my capabilities to design, simulate, and test my ideas, I present new optical solutions for assessing the issues especially for industrial problems.</p>
SKILLS	<ul style="list-style-type: none">Fourier optics and diffractive-refractive optics knowledge such as micro-lenses, lenses, etc.Fabrication of microoptics using direct laser polymerization technique.High-resolution interference microscopyOptical simulation software: VirtualLab Fusion (Coupled-Wave Analysis, Beam Propagation Method, ray tracing, etc), FDTD & mode Lumerical, FRED, CSTMicrowaveProgramming: MatlabSoftware: MS Office, Latex, Blender
LANGUAGE	<p>Persian (native), English (fluent), German (beginner), Arabic (basic)</p>

List of Publications

- Journal Papers** M. Yousefi, T. Scharf, and M. Rossi, "Light pattern generation with hybrid refractive microoptics under Gaussian beam illumination," *OSA Continuum* 3, 781-797 (2020).
<https://doi.org/10.1364/OSAC.386517>
- M. Yousefi, D. Nečesal, T. Scharf, and M. Rossi, "Near-field phase profile and far-field contrast modulation for micro-lens arrays at the refraction limit. " *SN Appl. Sci.* **2**, 1961 (2020).
<https://doi.org/10.1007/s42452-020-03759-y>
- M. Yousefi, T. Scharf, and M. Rossi, "Photonic nano-jet generation under converging and diverging beams, " *J. Opt. Soc. Am. B* 38, 317-326 (2021) [Selected as the spotlight in optics].
<https://doi.org/10.1364/JOSAB.405837>
- M. Yousefi, T. Scharf, and M. Rossi, "Contrast evaluation of Diffraction Pattern from sinusoidal phase gratings under Gaussian beam illumination," accepted for publication at *SN Appl. Sci.*
- P. Chiu, M. Yousefi, K.Vonmetz, F.Canini and H. P. Urbach, "Extended depth-of-field industrial camera with optimized cubic phase mask and digital restoration," Under revision (JEOS:RP)
- Patent** M. Yousefi, T. Scharf, and M. Rossi, "High Contrast dot generation and Flood illumination in one module based on LIMA ", Filed Apr. 29, 2019
- Proceedings** M. Yousefi, T. Scharf, and M. Rossi, "Dot pattern generation using thick sinusoidal phase grating under Gaussian beam illumination." *Digital Optical Technologies 2019*. Vol. 11062. International Society for Optics and Photonics, 2019.
- M. Yousefi, D. Nečesal, T. Scharf and M. Rossi, "Simulation of microoptics under inhomogeneous illumination: Sinusoidal Phase Grating under Gaussian Beam Illumination," 2019 24th Microoptics Conference (MOC), Toyama, Japan, 2019, pp. 224-225, doi: 10.23919/MOC46630.2019.8982802.
- Conferences & Workshops** Poster presentation in European Optical Society Biennial Meeting (EOSAM), 8 - 12 October, Delft, Netherlands, 2018
- M.Yousefi, T.Scharf , M.Rossi "Analysis of high diverging Gaussian beams propagation by phase gratings using different simulation approaches"
- Oral presentation for Digital Optical Technologies Conference in Munich, June 2019
- M. Yousefi, T. Scharf, M. Rossi, "Dot pattern generation using thick sinusoidal phase grating under Gaussian beam illumination," *Proc. SPIE* 11062, Digital Optical Technologies 2019, 1106211 (21 June 2019)
- Poster presentation for Workshop on information optics in Stockholm, July 2019
- M.Yousefi, T.Scharf , M.Rossi 'Contrast of Diffraction Pattern from Sinusoidal phase gratings under Gaussian beam illumination'
- Oral presentation in Topical meeting on Diffractive optics in Jena, 16-19 Sep 2019
- M.Yousefi, D.Nečesal, T.Scharf , M.Rossi "Simulation of microoptics under inhomogeneous illumination"
- Poster presentation in 24th microoptics conference (MOC), 17-20 Novemeber, Toyama, Japan, 2019
- M.Yousefi, T.Scharf , M.Rossi "Simulation of microoptics under inhomogeneous illumination: Sinusoidal Phase Grating under Gaussian Beam Illumination"